


2007

Signal Processing Of An Ecg Signal In The Presence Of A Strong Static Magnetic Field

Aditya Gupta
University of Central Florida

 Part of the [Electrical and Electronics Commons](#)
Find similar works at: <https://stars.library.ucf.edu/etd>
University of Central Florida Libraries <http://library.ucf.edu>

This Doctoral Dissertation (Open Access) is brought to you for free and open access by STARS. It has been accepted for inclusion in Electronic Theses and Dissertations, 2004-2019 by an authorized administrator of STARS. For more information, please contact STARS@ucf.edu.

STARS Citation

Gupta, Aditya, "Signal Processing Of An Ecg Signal In The Presence Of A Strong Static Magnetic Field" (2007). *Electronic Theses and Dissertations, 2004-2019*. 3185.
<https://stars.library.ucf.edu/etd/3185>

SIGNAL PROCESSING OF AN ECG SIGNAL
IN THE PRESENCE OF A STRONG STATIC MAGNETIC FIELD

by

ADITYA GUPTA

M.S. University of Central Florida, 2006

B. S. M S Ramaiah Institute of Technology, 2002

A dissertation submitted in partial fulfillment of the requirements
for the degree of Doctor of Philosophy
in the Department of Electrical and Computer Engineering
in the College of Engineering and Computer Science
at the University of Central Florida
Orlando, Florida

Fall Term
2007

Major Professor: Arthur Weeks

© 2007 Aditya Gupta

ABSTRACT

This dissertation addresses the problem of elevation of the T wave of an electrocardiogram (ECG) signal in the magnetic resonance imaging (MRI). In the MRI, due to the strong static magnetic field the interaction of the blood flow with this strong magnetic field induces a voltage in the body. This voltage appears as a superimposition at the locus of the T wave of the ECG signal. This loses important information required by the doctors to interpret the ST segment of the ECG and detect diseases such as myocardial infarction.

This dissertation aims at finding a solution to the problem of elevation of the T wave of an ECG signal in the MRI. The first step is to simulate the entire situation and obtain the magnetic field dependent T wave elevation. This is achieved by building a model of the aorta and simulating the blood flow in it. This model is then subjected to a static magnetic field and the surface potential on the thorax is measured to observe the T wave elevation. The various parameters on which the T wave elevation is dependent are then analyzed.

Different approaches are used to reduce this T wave elevation problem. The direct approach aims at computing the magnitude of T wave elevation using magneto-hydrodynamic equations. The indirect approach uses digital signal processing tools like the least mean square adaptive filter to remove the T wave elevation and obtain artifact free ECG signal in the MRI.

Excellent results are obtained from the simulation model. The model perfectly simulates the ECG signal in the MRI at all the 12 leads of the ECG. These results are compared with ECG signals measured in the MRI. A simulation package is developed in MATLAB based on the simulation model. This package is a graphical user interface allowing the user to change the strength of magnetic field, the radius of the aorta and the orientation of the aorta with respect to the heart and observe the ECG signals with the elevation at the 12 leads of the ECG.

Also the artifacts introduced due to the magnetic field can be removed by the least mean square adaptive filter. The filter adapts the ECG signal in the MRI to the ECG signal of the patient outside the MRI. Before the adaptation, the heart rate of the ECG outside the MRI is matched to the ECG in the MRI by interpolation or decimation. The adaptive filter works excellently to remove the T wave artifacts. When the cardiac output of the patient changes, the simulation model is used along with the adaptive filter to obtain the artifact free ECG signal.

I dedicate this book to Lord Sri Krishna through my beloved grand-spiritual master His Divine Grace A.C. Bhaktivedanta Swami Prabhupada, the Founder-Acarya of the International Society for Krishna Consciousness.

Srila Prabhupada is always absorbed in the perfect samadhi of Krishna consciousness.

His mind and heart, his thoughts, words, and deeds

Forever concentrated on one point — Serving the lotus feet of Radha-Govinda.

He taught the world to enter Samadhi and taste the eternal bliss of the soul

Surrendered to God in service by constantly chanting Hare Krishna.

Srila Prabhupada gave the most authoritative and exact translation of the divine book – “Bhagavad Gita As It Is.” It is not a mere product of his scholarship but a deeply realized penetration into the very essence of life, the problems that haunt all men, and solutions with which to exorcise them. Its powerful message of hope and enlightenment lifts the reader above the petty and temporal. The wisdom of the Gita leads to dimensions beyond ordinary education and enables one to analyze and understand life in a revolutionary way.

One of the seven hundred transcendental verses of the Bhagavad Gita:

yat karoṣi yad aśnāsi
yaj juhoṣi dadāsi yat
yat tapasyasi kaunteya
tat kuruṣva mad-arpaṇam

TRANSLATION

Whatever you do, whatever you eat, whatever you offer or give away, and whatever austerities you perform—do that, O son of Kuntī, as an offering to Me.

PURPORT

Thus, it is the duty of everyone to mold his life in such a way that he will not forget Kṛṣṇa in any circumstance. Everyone has to work for maintenance of his body and soul together, and Kṛṣṇa recommends herein that one should work for Him. Everyone has to eat something to live; therefore he should accept the remnants of foodstuffs offered to Kṛṣṇa. Any civilized man has to perform some religious ritualistic ceremonies; therefore Kṛṣṇa recommends, "Do it for Me," and this is called arcana. Everyone has a tendency to give something in charity; Kṛṣṇa says, "Give it to Me," and this means that all surplus money accumulated should be utilized in furthering the Kṛṣṇa consciousness movement. Nowadays people are very much inclined to the meditational process, which is not practical in this age, but if anyone practices meditating on Kṛṣṇa twenty-four hours a day by chanting the Hare Kṛṣṇa mantra round his beads, he is surely the greatest meditator and the greatest yogī.

ACKNOWLEDGMENTS

I thank my advisor, Arthur R Weeks, for his guidance and support throughout my research. He gave me the opportunity to work on very interesting research projects and challenged me to expand my problem solving abilities.

I thank my committee members Samuel M Richie, Harold I Klee, Christian S Bauer and David Nicholson for their time and valuable comments.

I thank Oosterom, A. van from the Department of Cardiology, University of Lausanne, Netherlands for his help and valuable suggestions for improving my research work.

I thank Invivo Corp., now Royal Philips Electronics for their financial support throughout my work.

I heartily thank my parents, Ravindra K Gupta and Radhika Gupta, who deserve a vast amount of credit for supporting me throughout my education and life and most of all for believing in my intellectual capacity.

I thank all my friends and relatives, who have encouraged and supported my endeavor and my work.

Most of all I thank Lord Sri Krishna, the Supreme Personality of Godhead who gives the intelligence and guides every activity of the living entity as the most beloved friend. I thank my instructing spiritual master His Holiness Trivikrama Swami Maharaj who mercifully encouraged me and kept my spiritual life alive during my stay in Orlando. I thank my eternal spiritual master His Holiness Bhakti Charu Swami Maharaj and my grand spiritual master His Divine Grace Abhay Charan Bhaktivedanta Swami Srila Prabhupada, who opens the eyes of the ignorant with a torch of knowledge and gives the intelligence of the higher dimension.

TABLE OF CONTENTS

LIST OF FIGURES	xiii
LIST OF TABLES.....	xvi
LIST OF SYMBOLS	xvii
LIST OF ABBREVIATIONS.....	xix
CHAPTER 1 INTRODUCTION	1
1.1 Problem Statement.....	1
1.2 The Electrocardiogram (ECG) signal	4
1.2.1 Basic structure of the heart and its physiology	4
1.2.2 Cardiac Electrophysiology.....	6
1.2.3 Segments of the ECG wave	9
1.2.4 Orientation of the 12 Lead ECG	10
1.3 Magnetic Resonance Imaging (MRI).....	12
1.3.1 Basics of MRI	12
1.3.2 The MRI system.....	13
1.3.3 Gradient Echo and Spin Echo	15
1.3.4 Frequency Encoding - Imaging.....	15
1.3.5 Advantages over other imaging systems.....	16
1.4 Flow of Electric Charges in Magnetic Field.....	16
1.4.1 Lorentz Force and Hall Effect.....	16
1.5 ECG Signal Distortions.....	18
1.6 Approach to remove the T wave elevation	19

1.7	Magneto fluid dynamics	21
1.7.1	Introduction and history of Magneto fluid dynamics	21
1.7.2	Governing equations of electrodynamics.....	23
1.7.3	Maxwell's equations for MHD	25
1.7.4	Different categories of fluid flow	26
1.7.5	Governing equations of Fluid Dynamics - Navier-Stokes equations.....	28
1.7.6	Magneto Fluid Dynamics Parameters	29
1.7.7	Incorporating Lorentz force into the Navier-Stokes - MHD equations	30
1.8	Pulse Oximeters	31
1.9	Contributions.....	33
1.10	Overview of Dissertation	34
CHAPTER 2	LITERATURE REVIEW	36
2.1	Blood and Blood Vessels	37
2.1.1	Properties of blood vessels.....	37
2.1.2	Properties of blood	38
2.1.3	Electrical conductance properties of blood in motion	39
2.1.4	Blood flow in the aorta	40
2.1.5	Modeling blood flow in arteries.....	42
2.2	Cardiac Output and Cardiac rate.....	46
2.2.1	Velocity Encoded MRI	47
2.2.2	Thermo dilution	50
2.2.3	Doppler Ultrasound.....	50
2.3	Relation between blood volume in the finger and cardiac output	52

2.3.1	Relation between the aortic blood flow (cardiac output) and blood pressure in the aorta.....	55
2.3.2	Relation between the blood pressure in the aorta and the blood pressure in the finger	61
2.3.3	Relation between the blood pressure in the finger and the blood volume pulse measured from pulse oximeter	63
2.4	Effect of magnetic field on blood flow	67
CHAPTER 3 REVIEW OF EXPERIMENTS ON ANIMALS AND PRESENT MODELS		72
3.1	Elevation of T wave in magnetic fields – experiments on animals	72
3.2	Simulation models of the heart	76
3.2.1	Electromechanical Model of the Heart	77
3.2.2	Simulation Model of Cardiac Electrical activity	83
3.2.3	ECG Simulation Package - ECGSIM	84
CHAPTER 4 METHOD TO COMPUTE AND SIMULATE THE INDUCED T WAVE POTENTIAL.....		91
4.1	ECGSIM Model modified to study the elevated T waves of an ECG inside a static magnetic field based on Lorentz Equation	92
4.2	Model to compute the induced T wave potential.....	98
4.2.1	The Magneto Hydro Dynamic Equations	99
4.2.2	Model of the aorta.....	103
4.2.3	Computing the potential induced for each of the slices of the aorta.....	108
4.2.4	Transfer Matrix	112

4.2.5	Final Computations.....	117
4.3	Parameters required to compute the induced potential.....	118
4.4	GUI Simulation Package.....	125
CHAPTER 5 LINEAR ADAPTIVE FILTERS TO ELIMINATE T WAVE ARTIFACTS.....		137
5.1	Implementation of the LMS filter on simulation results.....	138
5.2	Adaptive LMS filter with other noise removal filters.....	143
5.3	LMS Filter on the T waves of ECG signal	152
5.4	LMS Adaptive Filter on Real Data	160
5.4.1	QRS peak detection algorithm.....	161
5.4.2	Signal Processing on real data	165
CHAPTER 6 DISCUSSIONS AND FUTURE WORK.....		175
6.1	Comparison of GUI Simulation Package with real data.....	175
6.2	Relation between T wave elevation and the magnetic field	184
6.3	Relation between T wave elevation and cardiac output.....	188
6.4	Results from the adaptive system	190
6.5	Future Work.....	193
6.6	Conclusion	194
LIST OF REFERENCES.....		196

LIST OF FIGURES

Figure 1 Elevation of the T wave of ECG when subjected to different magnetic fields.	2
Figure 2 Schematic representation of the effect of magnetic field on the ECG.	4
Figure 3 Structure of the heart and flow of blood in the atria and ventricles.	5
Figure 4 The conduction system of the heart – SA node, AV node and Purkinje fibers.	6
Figure 5 Action potential	7
Figure 6 Shape of the action potential at various points on the heart.	8
Figure 7 One complete ECG cycle - the P wave, QRS complex, ST segment, T wave and the U wave.	9
Figure 8 Lead placement on the body.....	11
Figure 9 Einthoven's triangle.....	12
Figure 10 The MRI system.	13
Figure 11 Block Diagram of the entire research.....	20
Figure 12 Pressure and velocity pulse waveforms in the aorta and arterial branches of a dog.....	41
Figure 13 Comparison of derived arterial flow waveform (top) and the measured Doppler waveform (bottom).	53
Figure 14 Three element model to compute flow.....	60
Figure 15 Change in the velocity profile of viscous conducting fluid when subjected to a magnetic field.....	69
Figure 16 T-wave elevation in rabbits	73

Figure 17 Percentage increase in T wave amplitude in Macaca monkeys as a function of magnetic field strength.....	74
Figure 18 Elevation of T wave for different magnetic fields (0 T to 1.52 T) in Macaca monkeys.	75
Figure 19 Electromechanical model construction, simulation of cardiac activity and clinical data analysis.	79
Figure 20 One dimensional measure of action potential simulation.....	80
Figure 21 Interactive user control – controls for simulation and visualization.	84
Figure 22 Display of the ECGSIM window.	85
Figure 23 Mechanism responsible for induced potential.....	94
Figure 24 Blood flow profile in the aorta obtained from MRI.	95
Figure 25 ECG tracing at lead II showing the elevated T wave for a field of 1.5 T.....	96
Figure 26 ECG tracing at lead II showing the elevated T wave for a field of 3.0 T.....	96
Figure 27 The structure of the aorta showing the three different sections.....	104
Figure 28 The longitudinal axis of the aorta.	106
Figure 29 Tube of constant radius developed around the axis of figure 6.....	107
Figure 30 Model of the aorta showing the nodes and triangles.	108
Figure 31 Angle of each slice with respect to the magnetic field.....	109
Figure 32 The potential distribution on the aorta surface determined from Maxwell 2D.	111
Figure 33 Volume V showing the inner and outer surfaces and the observation point o.	114
Figure 34 Wilson Central Terminal (WCT) – average of limb potentials.....	118

Figure 35 Pulse transit time (PTT) calculation.	120
Figure 36 Electrical representation of a segment of artery of unit length	122
Figure 37 The pressure waveforms at the aorta (minimum amplitude), the finger (maximum amplitude) and some intermediate arteries.....	123
Figure 38 Blood flow in the aorta (maximum amplitude), brachialis and the finger (minimum amplitude).	124
Figure 39 Main screen of the simulation package showing heart, thorax and aorta model.	130
Figure 40 Second scene showing the original ECG and the ECG in the MRI at the 12 leads.	131
Figure 41 Third Scene showing the model of the aorta and the potential induced at the node selected (heavy black rectangle on the model of aorta).	132
Figure 42 Screen with the option to change the orientation of the aorta with respect to the heart.....	133
Figure 43 Final screen showing the aortic blood flow, the ECG in a magnetic field, corrected and filtered ECG and the induced potential.	134
Figure 44 Potential induced on the surface of the aorta. Color transition from red to blue indicates maximum positive to minimum negative.	135

LIST OF TABLES

Table 1 The significance of each segment of the ECG [3].	10
Table 2 Typical data for human aorta	38
Table 3 Simulation of 12 lead ECG in presence of 1.5 T magnetic field.	97
Table 4 ECG tracings at the 12 leads under normal conditions (A) compared with the tracings when subjected to 1.5 T static magnetic field (B).	178
Table 5 Comparison of the ECG tracings measured and the tracings obtained from the simulation at leads I, II, III, AVR, AVL and AVF.	180
Table 6 Comparison of the ECG tracings measured and the tracings obtained from the simulation at leads V1, V2, V3, V4, V5 and V6.	181
Table 7 Magnitude of the normal T wave amplitude, the T wave amplitude in a magnetic field of 1.5 T and the magnitude of induced potential at 12 leads.	182
Table 8 T wave elevation at lead II for varying magnetic fields (0 to 4 T). Table also shows percentage increase in T wave amplitude.	186
Table 9 The slope of the line joining the ST segment measured at different points of the measured ECG signals	192
Table 10 The performance of the adaptive system – the ECG signal outside the MRI, the ECG signal in the MRI and the adaptive system output.	193

LIST OF SYMBOLS

QUANTITY	SYMBOL
Charge density	ρ, ρ_e
Compliance	C
Current Density	J
Electric Charge	Q
Electrical conductivity	Σ
Electrostatic Field	E, E_s
Force	F
Hartmann Number	Ha
Interaction Parameter	N
Magnetic field	B
Magnetic field Intensity	H
Magnetic Reynold's number	Rm
Permeability	M
Permittivity	E
Pressure	P, p
Pulse Wave Velocity	C
Radius	r, a
Reynold's number	Re
Stress	T

Velocity	V
Viscosity	μ, η
Voltage	V, ψ
Young's modulus of elasticity	E

LIST OF ABBREVIATIONS

Atrio-ventricular	AV
Cardiac Output	CO
Computed Tomography	CT
Electrocardiogram	ECG, EKG
Equivalent Double Layer	EDL
Fast Fourier Transform	FFT
Finite Impulse Response	FIR
Graphical User Interface	GUI
Least Mean Square	LMS
Magnetic Resonance	MR
Magnetic Resonance Imaging	MRI
Magneto-fluid-dynamics	MFD
Magneto-hydro-dynamics	MHD
Mean Arterial Pressure	MAP
Nuclear Magnetic Resonance	NMR
Photo-plethysmogram	PPG
Pulse Transit Time	PTT
Pulse Wave Velocity	PWV
Radio Frequency	RF
Sino-atrial	SA

Uniform Double Layer

UDL

Wilson's Central Terminal

WCT

CHAPTER 1

INTRODUCTION

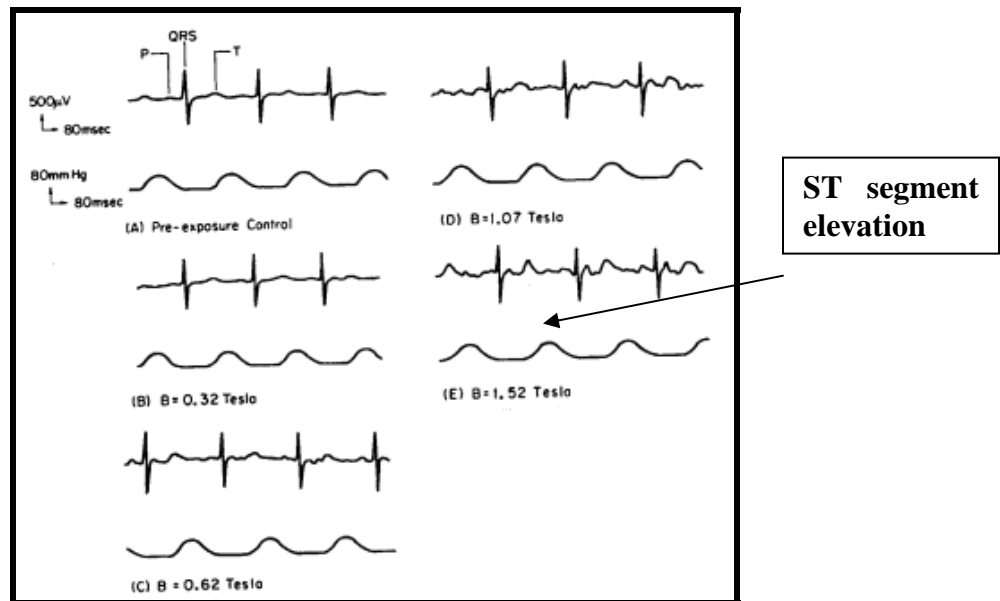
1.1 Problem Statement

Magnetic Resonance Imaging (MRI) has over the years become an essential component of diagnostic medicine. With the use of high magnetic fields (1.5 T and above), the biological effects of static magnetic fields have become an important area of research. Also the high fields restrict the use of ferromagnetic devices in the MR rooms [1].

Electrocardiography (ECG) is the most commonly used diagnostic tool in cardiology. It contributes significantly to the diagnosis and management of patients with cardiac disorders. Importantly, it is essential to the diagnosis of cardiac arrhythmias and the acute myocardial ischemic syndromes [2]. These two conditions account for the majority of cardiac fatalities. Hence ECG is appropriately used as a screening test in many circumstances.

When a patient is inside the MRI bore, the body of the patient is subjected to magnetic fields. An instantaneous magnetic field strength dependent increase in the T wave of the ECG signal is observed. Figure 1 shows this elevation when the heart of a monkey was subjected to different magnetic fields [3]. Also the plots reveal the increase in T wave elevation with an increase in the magnetic field.

The superimposition of the induced signal distorts the ST segment of the ECG (refer figure 1), thus making it impossible for doctors to diagnose critical diseases such as myocardial infarction [2]. The measurements taken on the ST segment form a predominant factor in the interpretation phase of the ECG. ST segment is an indicator of the imbalance in the myocardial oxygen supply/demand ratio and becomes irregular in patients suffering from myocardial ischemia or myocardial infarction [2]. Another problem, though less significant, caused due to the elevation is the erroneous results produced by various QRS detectors. These detectors working on the concept of threshold selection see the elevated T wave as a QRS pulse and hence fail to identify the true QRS peaks. Hence with the increasing use of MRI for critically ill patients, the problem of elevation of the T wave of an ECG signal has become very significant.



(Reproduced with kind permission of Springer Science and Business Media)

Figure 1 Elevation of the T wave of ECG when subjected to different magnetic fields.

The temporal sequence of this signal and its reversibility following the termination of the magnetic field exposure are consistent with the suggestion that it arises from a magnetically induced aortic blood flow potential superimposed on the native T wave [3]. There is also a suggestion of further superposition of a second induced flow potential that can be detected only at high fields and this is associated with the blood flow in the pulmonary artery [3]. But since the blood flow in the aorta is much larger than the pulmonary artery, the magneto-hydro-dynamic effect in the aorta is much more significant [3]. The magneto-hydrodynamic interaction of a stationary magnetic field with blood flow produces a reduction in flow velocity and a compensatory elevation in blood pressure to retain a constant volume flow rate.

Hence, this dissertation aims at finding a solution to the above mentioned problem of elevation of the T wave of an ECG signal in the MRI. The first step is to simulate the entire situation and obtain the magnetic field dependent T wave elevation. This is achieved by building a model of the aorta and simulating the blood flow in it. This model is then subjected to a static magnetic field and the surface potential on the thorax is measured to observe the T wave elevation. The various parameters on which the T wave elevation is dependent are then analyzed. Different approaches are used to reduce this T wave elevation problem. The direct approach aims at computing the magnitude of T wave elevation using magneto-hydro-dynamic equations. The indirect approach uses digital signal processing tools like the least mean square adaptive filter to remove the T wave elevation and obtain artifact free ECG signal in the MRI.

The next sections in this chapter discuss the basics of electrocardiography (ECG), magnetic resonance imaging (MRI) and the basic equations governing the flow of electric charges in a magnetic field.

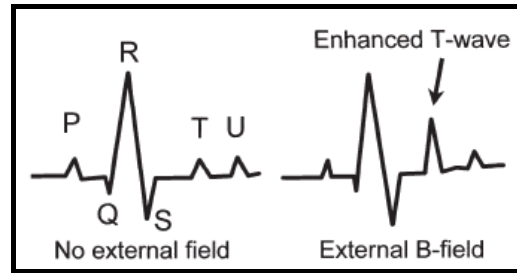


Figure 2 Schematic representation of the effect of magnetic field on the ECG.

1.2 The Electrocardiogram (ECG) signal

1.2.1 Basic structure of the heart and its physiology

The heart is the organ that supplies blood and oxygen to all parts of the human body. About the size of a clenched fist weighs about 10.5 ounces and is shaped like a cone [4]. The heart is located in the chest cavity just posterior to the breastbone, between the lungs and superior to the diaphragm. The heart is surrounded by a fluid filled sac called the pericardium.

The heart consists of four chambers – the upper two atria and the lower two ventricles. In the lungs, venous blood received from the right side of the heart is oxygenated and then flows into the left atrium of the heart. From the left atrium, blood enters the much thicker left ventricle. The valve lying between the left atrium and the left ventricle, namely the

mitral valve opens when the pressure in the left ventricle is very low [4]. This low pressure is its relaxation phase called diastole. During ventricular contraction or systole, the valve closes and the increased pressure in the left ventricle prevents blood from reentering the atrium. The aortic valve located at the base of the aorta opens and blood is expelled into the aorta from where it travels throughout the circulation to reach all parts of the body.

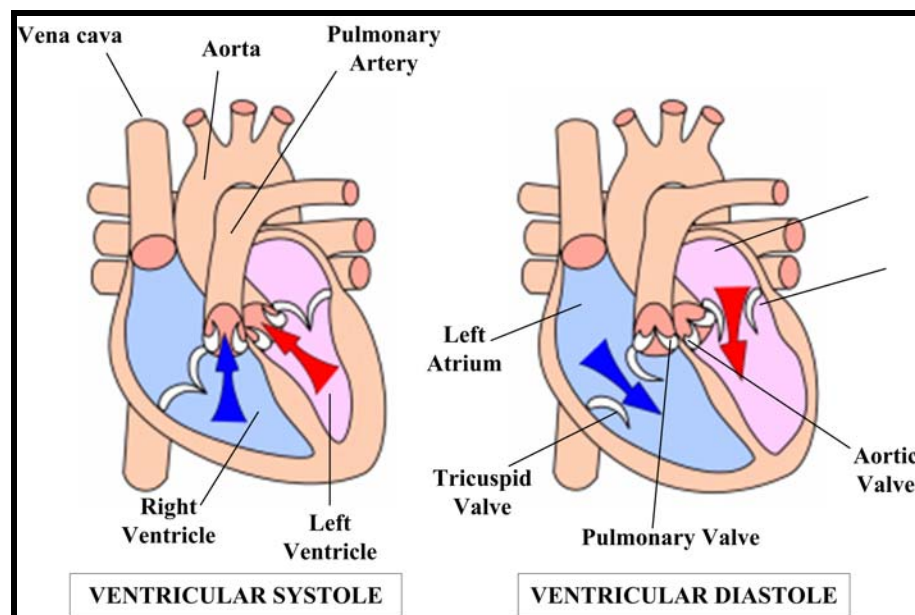
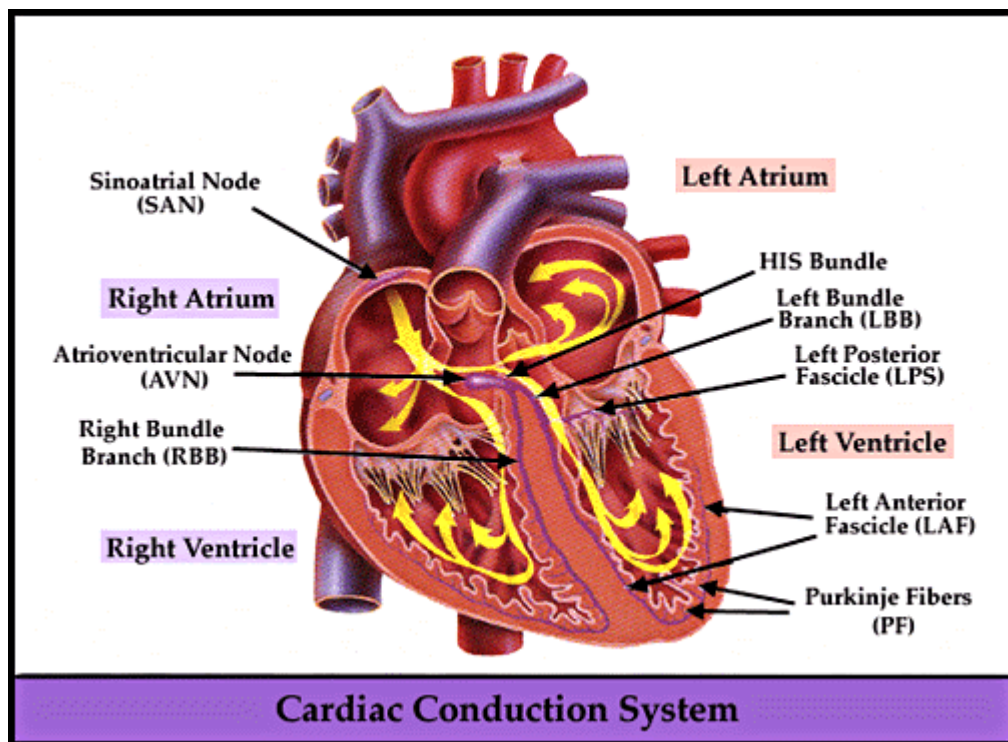


Figure 3 Structure of the heart and flow of blood in the atria and ventricles.

The two main veins entering the right atrium are the superior and inferior vena cava, which drain deoxygenated blood from all parts of the body. Blood flowing into the right atrium then enters the right ventricle through the tricuspid valve. The contracting right ventricle forces the blood into the lungs through the pulmonary artery, where it is oxygenated to return to the left atrium to complete the circulation [4].

1.2.2 Cardiac Electrophysiology

The heart beats at a relatively constant rate and rhythm due to special properties of cardiac pacemaker cells [4,5]. These pacemakers depolarize at regular intervals without any external stimuli from neighboring cells. The certain cells that possess these properties include: Sinoatrial Node (SA), the Atrio-Ventricular Node (AV), the His Bundle, and Purkinje fibers.



(Reproduced under the conditions specified by the Creative Commons Deed <http://creativecommons.org/licenses/by-nd-nc/1.0/>)

Figure 4 The conduction system of the heart – SA node, AV node and Purkinje fibers.

Pacemaker cells depolarize in rhythmic fashion. After depolarization, the cells begin to repolarize. Then inward sodium currents slowly begin flowing and the cells begin to depolarize again [5, 6]. Eventually the cells reach threshold, and an action potential fires, causing the atria or the ventricles to contract. Because of the regular inward currents, pacemaker cells maintain a resting potential of -50 to -60mV. This increased membrane potential deactivates fast Sodium channels. Pacemakers therefore rely on Calcium as the primary cat-ion which triggers action potentials [6].

When the SA node depolarizes, the action potential spreads throughout the atria, rapidly causing atrial depolarization and contraction. The action potential rapidly enters the AV node where it is delayed for 120 to 200 msec [5]. The AV node conducts slowly because it depends on slow inward calcium currents to depolarize cells. The AV node also must conduct the action potential through thin fibers which slows conduction further. This delay is deliberate and allows the ventricles time to fill following atrial contraction [6].

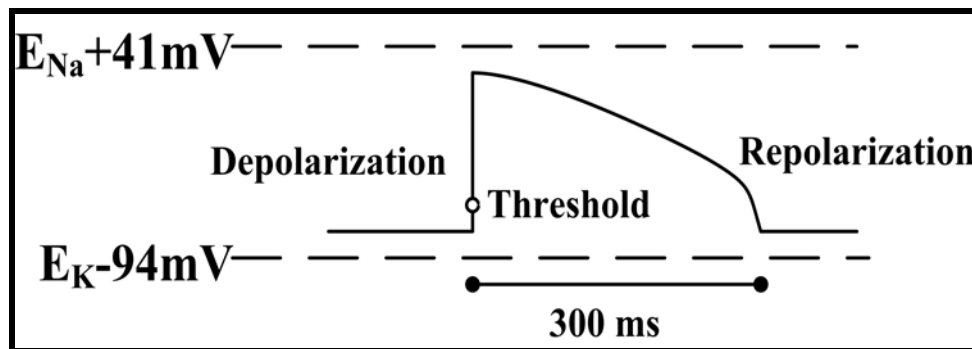


Figure 5 Action potential

The action potential spreads to the Bundle of His and then rapidly down the three bundle branches – right, left anterior and left posterior bundle [7]. These rapidly depolarize both ventricles. The left ventricle depolarizes slightly before the right. The cells repolarize following depolarization. Atrial depolarization is not seen in an ECG because the higher magnitude ventricular depolarization occurs simultaneously. Ventricular repolarization is seen as the T wave.

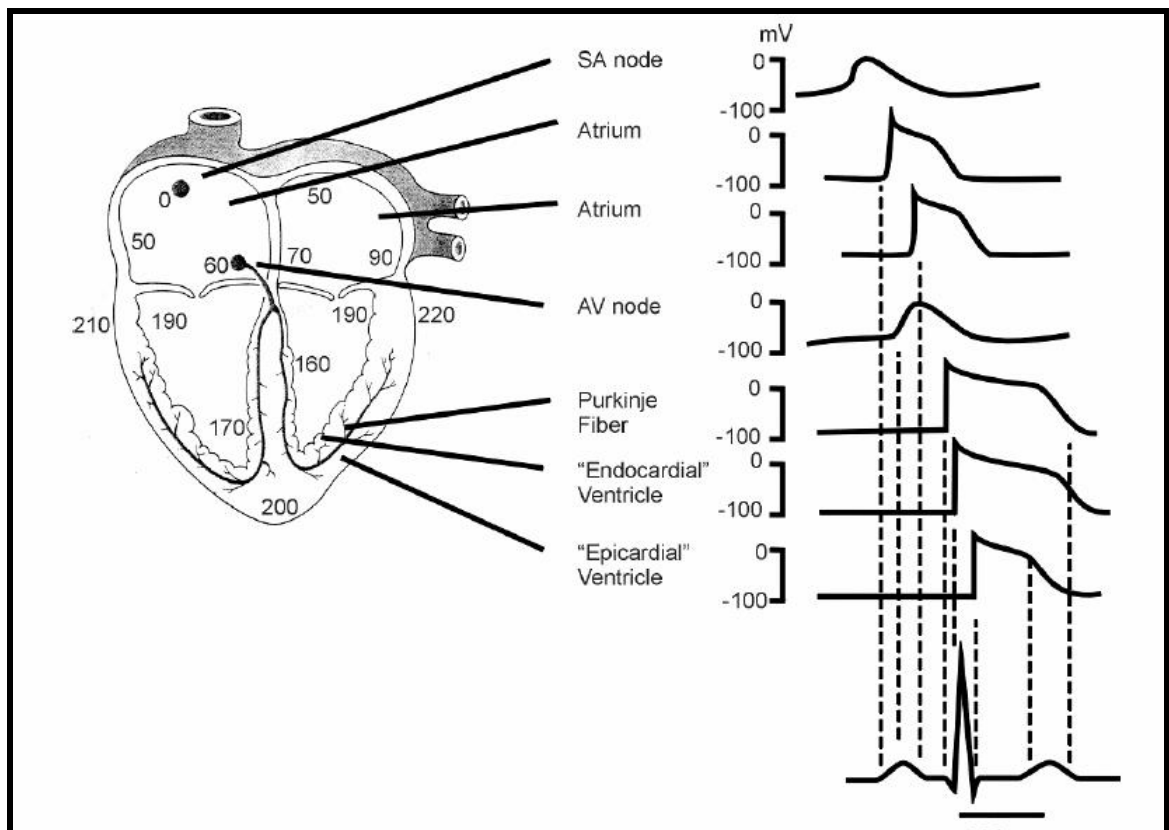


Figure 6 Shape of the action potential at various points on the heart.

1.2.3 Segments of the ECG wave

The process of recording the potential changes at the skin surface resulting from depolarization and repolarization of the heart muscle is called electrocardiography and the record is called an electrocardiogram (ECG or EKG) [8].

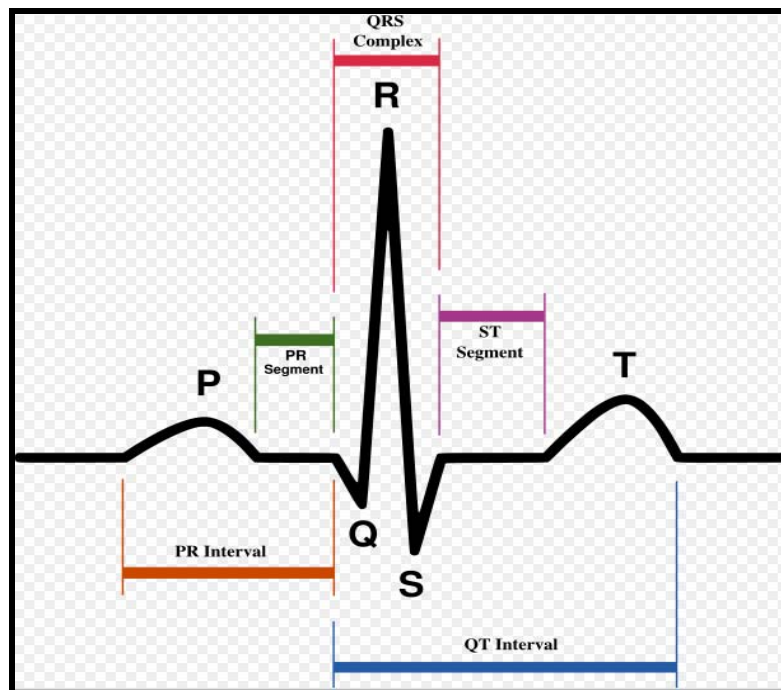


Figure 7 One complete ECG cycle - the P wave, QRS complex, ST segment and the T wave.

Table 1 The significance of each segment of the ECG [3].

ECG segment	Sequence of Activation during the segment
First half of P wave	Sinus impulse activates the right atrium and reaches AV Node
P Wave	Left Atrium and AV Node activated
PR Segment	His Purkinje system is being activated
Q Wave	Interventricular septum activated (l to r)
QRS complex	Two ventricles activated from endocardium to epicardium.
ST segment and T wave	Repolarization of the ventricles.

1.2.4 Orientation of the 12 Lead ECG

The potential change on the surface of the skin is measured using 10 electrodes [7, 8]. The 12-lead ECG provides spatial information about the heart's electrical activity in 3 approximately orthogonal directions: Right – Left; Superior – Inferior; Anterior – Posterior [8]. Each of the 12 leads represents a particular orientation in space. Figure 8 shows the lead placement on the body. In the figure, RA refers to the right arm, LA refers to the left arm and LF refers to the left foot.

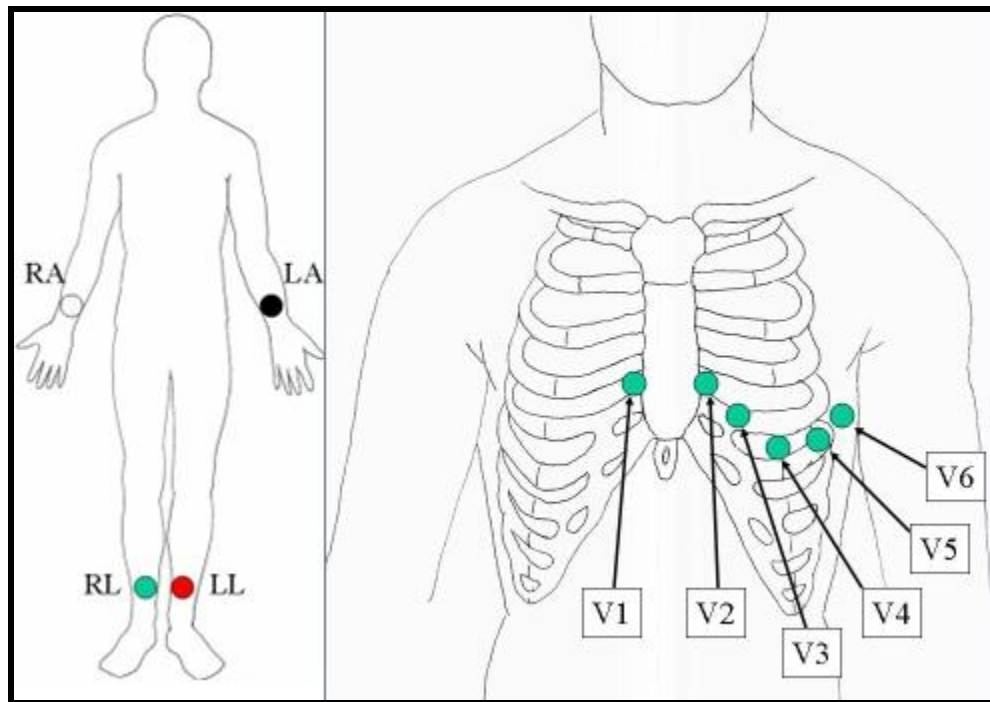


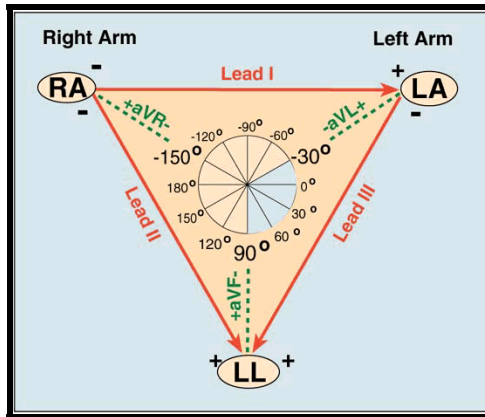
Figure 8 Lead placement on the body.

For the 12 leads, the direction in which the potential is measured and the plane of measurement is:

1. Bipolar limb leads (frontal plane):
 - a. Lead I: RA (-) to LA (+) (Right Left, or lateral)
 - b. Lead II: RA (-) to LF (+) (Superior Inferior)
 - c. Lead III: LA (-) to LF (+) (Superior Inferior)
2. Augmented unipolar limb leads (frontal plane):
 - a. Lead aVR: RA (+) to [LA & LF] (-) (Rightward)
 - b. Lead aVL: LA (+) to [RA & LF] (-) (Leftward)
 - c. Lead aVF: LF (+) to [RA & LA] (-) (Inferior)
3. Unipolar (+) chest leads (horizontal plane):

- d. Leads V1, V2, V3: (Posterior Anterior)
- e. Leads V4, V5, V6: (Right Left, or lateral)

Figure 9 shows the standard Einthoven's Triangle [9], which gives information about the vector for each ECG lead type. Each of the 6 frontal plane leads has a negative and positive orientation (as indicated by the '+' and '-' signs). Lead I (and to a lesser extent Leads aVR and aVL) are right - left in orientation. Also, Lead aVF (and to a lesser extent Leads II and III) are superior - inferior in orientation [8].



(Reproduced under the conditions specified by the Creative Commons Deed <http://creativecommons.org/licenses/by-nd-nc/1.0/>)

Figure 9 Einthoven's triangle.

1.3 Magnetic Resonance Imaging (MRI)

1.3.1 Basics of MRI

Magnetic resonance imaging (MRI) is an imaging technique used primarily in medical settings to produce high quality images of the inside of the human body [9, 10]. MRI is

based on the principles of nuclear magnetic resonance (NMR), a spectroscopic technique used by scientists to obtain microscopic chemical and physical information about molecules. MRI started out as a tomographic imaging technique, that is it produced an image of the NMR signal in a thin slice through the human body. MRI has advanced beyond a tomographic imaging technique to a 3D volume imaging technique [10].

1.3.2 The MRI system

MR Scanner consists of three main hardware components [10]:

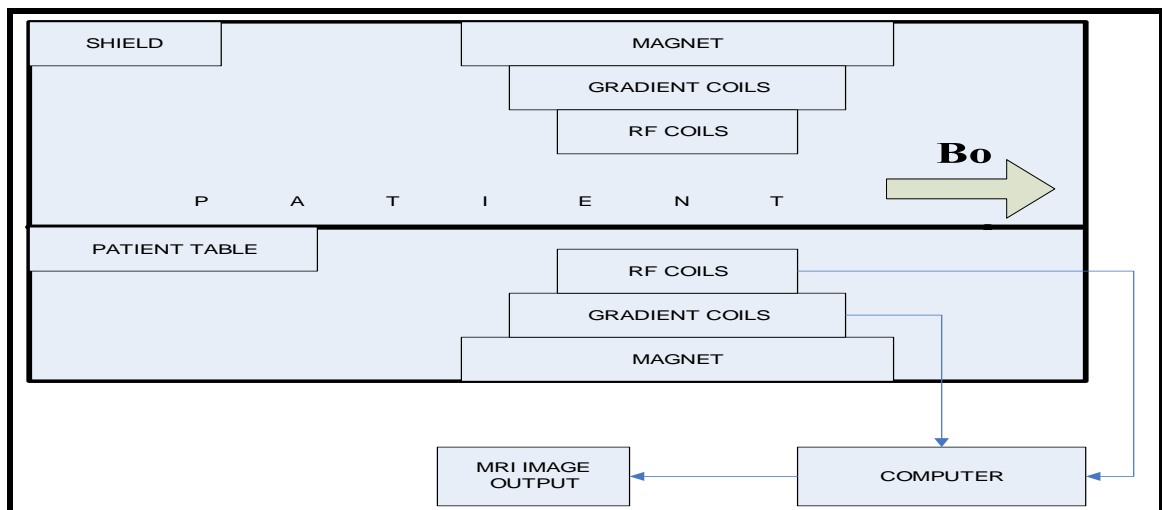


Figure 10 The MRI system.

The main magnet produces a strong uniform magnetic field (B_0 field). When placed in a magnetic field, the hydrogen atom has a strong tendency to line up with the direction of the magnetic field [11]. The magnetic field runs straight down the center of the tube in which we place a patient. The hydrogen protons in the patient's body will line up in the

direction of either the uniform magnetic field B_0 or in the opposite direction. The vast majority of these protons will cancel each other out - that is, for each one lined up toward the feet, one toward the head will cancel it out. Only a couple of protons out of every million are not canceled out. The sheer number of hydrogen atoms in the body gives what is needed to create desired images.

The RF System consists of a transmitter coil for rotating magnetic field and a receiver that converts magnetic into electrical field [10]. The MRI machine applies an RF pulse at a frequency specific only to the hydrogen atom. The system directs the pulse toward the area of the body that is needed to be examined. The pulse causes the protons in that areas to absorb the energy, making them spin, or precess, in a different direction. This is the "resonance" part of MRI. The RF pulse forces the protons (only the one or two extra unmatched protons per million) to spin at a particular frequency, in a particular direction. The specific frequency of resonance is called the Larmour frequency (42.59 MHz/Tesla) and is calculated based on the particular tissue being imaged and the strength of the main magnetic field.

The gradient system produces time varying magnetic fields. Three gradient magnets are arranged in such a manner inside the main magnet that when they are turned on and off very rapidly in a specific manner, they alter the main magnetic field on a very local level. This provides a means of modulating the Larmour frequency as a function of the spatial position in the MRI bore. A "slice" of any part of the body in any direction can be obtained giving a huge advantage over any other imaging modality. That also means that

the patient doesn't need to move in the machine to get an image from a different direction -- the machine can manipulate everything with the gradient magnets and the gradient switching patterns.

1.3.3 Gradient Echo and Spin Echo

When the RF pulse is turned off, the hydrogen protons begin to slowly (relatively) return to their natural alignment within the magnetic field and release their excess stored energy [9]. When they do this, they give off a signal that a receiver coil picks up and sends to a computer system through an analog interface. The system receives mathematical data that is converted, through the use of a Fourier transform, into a picture that can be viewed on a film [9].

1.3.4 Frequency Encoding - Imaging

By manipulating the magnetic field through gradient coils, protons at different points in space have different resonant Larmour frequencies. This is called frequency encoding. Many commercial gradient systems are capable of producing gradients of 20 mT/m to 100 mT/m [11]. Since precessing magnetization from the entire object induces signal changes in the receiver coil, the received signal now contains a spectrum of received signals. Frequency analysis (FFT) can then be used to discriminate between different spatial locations based on the spatial distribution of magnetic field strength.

1.3.5 Advantages over other imaging systems

The MRI gives a very high precision of detail over many other systems. MRIs do not use ionizing radiation (is a comfort to many patients). MRI contrast materials have a very low incidence of side effects [9]. They have the ability to image in any plane unlike CT (computer tomography) which is limited to one plane, the axial plane. An MRI system can create axial images as well as images in the sagittal plane and coronal or any degree in between, without the patient ever moving [9, 10]. The three gradient magnets discussed earlier allow the MRI system to choose exactly where in the body to acquire an image and how the slices are oriented.

1.4 Flow of Electric Charges in Magnetic Field

1.4.1 Lorentz Force and Hall Effect

The T wave elevation of the ECG signal in the MRI is caused due to the interaction of the electric charges in the blood with the uniform static magnetic field of the MRI. This section discusses the interaction of the electric charges with a static magnetic field.

A point charge q moving with a velocity v in a magnetic field B will experience a force called the Lorentz force [12], given by the following equation:

$$F = q \cdot v \times B \quad (1)$$

When applied to a fluid (with density ρ) that is charged with a charge density q' per unit volume the body force per unit mass becomes:

$$F = (v \times B) \cdot q' / \rho$$

(2)

Consider the flow of current in a conductor in the presence of a magnetic field. Due to the Lorentz force there is a tendency for the individual charges to move perpendicular to the direction of flow and perpendicular to the magnetic field. The maximum effect occurs when the magnetic field is perpendicular to the flow of charges. The charges accumulate on the conductor surfaces. This charge distribution gives rise to an electric field and hence a potential difference exists across the conductor. This voltage is called the Hall voltage [12] and is given by:

$$\psi = d \cdot V \cdot B$$

(3)

where d is the width of the channel, V is the velocity of blood flow and B is the external magnetic field applied.

The Lorentz equation is derived considering a channel with rectangular cross-section and conducting walls. In the MRI, a voltage is induced due to the effect of the magnetic field on the blood flow in the aorta. The aorta wall has a circular cross-section and also the walls of the artery are non-conducting. The Hall voltage equation does not consider many important parameters like the Hartmann number, the aortic blood pressure, and the density, conductivity and viscosity of blood. To consider these important parameters, section 1.7 discusses the more exact - magneto hydro dynamic equations.

1.5 ECG Signal Distortions

In the MRI, an increase in the T wave amplitude of the ECG signal is observed. This is related to the voltage induced due to the flow of blood in the aorta in the presence of the static magnetic field of the MRI. Blood contains charge carriers and the flow of charge carriers in the presence of a magnetic field induces a voltage, as discussed in the previous section. During every heart cycle, the heart pumps blood to the different parts of the body through the aorta. The blood flow in the aortic arch is perpendicular to the static magnetic field [13] and thus is the major factor responsible for the induced voltage that appears as an elevation of the T waves [3]. The induced voltage is directly proportional to the volume of blood in the aorta during each heart cycle [14]. The volume of blood flow in the aorta changes during every heart cycle depending on the activity of the patient. For example, a patient during exercise will have a higher volume of blood flow in the aorta as compared to a resting or sleeping condition. A higher volume of blood in the aorta implies a higher number of charge carriers and hence a higher induced voltage.

To compute the magnitude of induced voltage, it is essential to determine the volume of blood in the aorta during every heart cycle. A term related to the amount of blood ejected from the ventricles is the ‘cardiac output.’ Cardiac output [15] is a measure of the pumping ability of the heart and is the amount of blood pumped from the heart in ml measured every minute.

The aortic blood flow or cardiac output can be determined by measuring the pulse wave velocity (PWV) of the blood in the aorta [16, 17]. The motivation behind this research is

that the velocity profile of blood flow in the aorta is related to the pulse wave velocity. The velocity profile obtained can be directly used in the Lorentz's equation to calculate the voltage induced by the magnetic fields in the ECG signal. Hence if a method of measuring the PWV of the patient in the MRI environment can be devised, then it can be used to provide a continuous measure of the cardiac output [16, 17]. Also when integrated over a single heart beat it can provide the stroke volume and when integrated over a minute it can provide the cardiac minute volume. This can be used to estimate the magnitude of an elevated T wave in the MRI.

1.6 Approach to remove the T wave elevation

The aim of this research is to remove the T wave elevation from the ECG signal so that artifact free ECG signal can be obtained in the MRI. Two different approaches are used to solve this problem. The first approach is the indirect method that uses linear adaptive filters to remove the T wave elevation. The second approach used magneto hydro dynamic equations to directly measure the magnitude of T wave elevation. Both these methods are briefly discussed below and are presented in great detail in the later chapters.

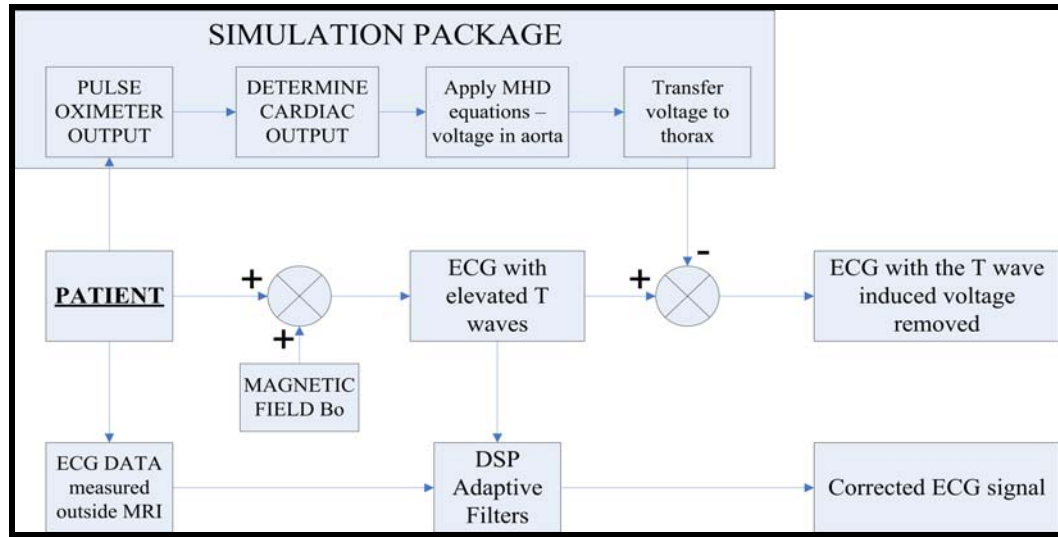


Figure 11 Block Diagram of the entire research

The first approach is based on digital signal processing filters. This approach requires the ECG of the patient before he/she enters the MRI room in addition to the ECG in the MRI. The approach uses LMS adaptive filtering techniques to adapt the ECG in the MRI to the ECG signal obtained prior to entering the MRI. The specifications of the LMS filter and the results are discussed in the fourth chapter of this dissertation.

The second approach is based on simulating the ECG signals in the MRI with elevated T waves. In this simulation, the induced voltage due to blood flow in the aorta is computed. A model of the aorta is developed and the blood flow in it is simulated. To simulate the blood flow, the cardiac output needs to be determined. It is difficult to directly measure the cardiac output of the patient in the MRI due to many reasons - the patient in the MRI is not easily accessible, it takes time to acquire a phase, encoded MRI image and a non-invasive method of determining the cardiac output needs to be devised. Also for computing the induced voltage the cardiac output needs to be determined continuously.

The signal obtained from a pulse oximeter – photo-plethysmogram (PPG) signal is easily available even in the MRI and is a good starting point for determining the cardiac output in the aorta. This is obtained by using various algorithms that relate the PPG to the cardiac output. Once the cardiac output is obtained, magneto-hydro-dynamic equations are used to determine the induced voltage in the aorta. This induced voltage is then transferred to the thorax using transfer functions that considers the different conductivities of various tissues and organs between the heart and the thorax. This entire method will be discussed in more detail in the later chapters.

The next sections discuss the basics of magneto-hydro-dynamic equations starting from Maxwell's equations and Navier Stokes equations. Also the basics of pulse oximeters and a brief idea of how the signal obtained from pulse oximeters can be used to obtain cardiac output are discussed.

1.7 Magneto fluid dynamics

1.7.1 Introduction and history of Magneto fluid dynamics

The flow of a conducting fluid through round pipes subjected to a magnetic field is analyzed in magneto-fluid-dynamics (MFD) [18]. MFD is the study of flow of electrically conducting fluids in electric and magnetic fields. It describes the effect of magnetic field on the flow and the effect of the flow on the magnetic field by combining electromagnetic and fluid dynamic theories. MFD deals with an electrically conducting fluid, whereas its subtopics, magneto-hydro-dynamics (MHD) and magneto-gas-

dynamics (MGD), specifically deal with electrically conducting liquids and ionized gases respectively.

The effect of magnetic field on the flow of fluid has been a topic of research for many decades. In 1937, Hartmann obtained the exact solution to the flow between two parallel, non-conducting walls with the magnetic field perpendicular to the flow [19, 20]. Only the transverse component of all physical quantities except pressure was considered. In 1953, Shercliff solved the corresponding more general problem of the flow in a rectangular duct [19, 21]. He considered both co-ordinates normal to the direction of fluid motion. The results of his exact solution show that for large Hartmann number, the velocity distribution consists of a uniform core in the center with boundary layers near the walls. After three years, he used this result to derive the exact solution for the flow in a circular pipe for large Hartmann number assuming walls of zero conductivity and subsequently for small conductivity [19, 22]. In 1962, Richard R Gold considered the problem of flow of an incompressible, viscous, electrically conducting fluid through a circular pipe in the presence of an applied uniform magnetic field. The solution is exact and is thus valid for all values of Hartmann number [19]. Excellent agreement exists between the theoretical results and the experimental values. Hence this solution is used to compute the voltage induced in the aorta due to the static magnetic field of the MRI. The details are provided in the following chapters.

Before discussing the details of the MHD equations, the basic equations of electrodynamics and fluid dynamics are discussed in the next sections.

1.7.2 Governing equations of electrodynamics

A particle charge q moving with a velocity v is subject to three electromagnetic forces, described by the equation [12]:

$$F = qE_s + qE_i + qv \times B \quad (4)$$

where E_s is the electrostatic field, E_i is the electric field induced by changing magnetic field and B is the magnetic field.

The three electromagnetic forces are:

1. Electrostatic Force (Coulomb force): This arises due to mutual repulsion or attraction of electric charges.
2. The force experienced by the charge in the presence of a time varying magnetic field.
3. Lorentz force, which arises from the motion of the charge in a magnetic field.

The Coulomb's law (E_s is irrotational) and Gauss's law (divergence of E_s is a fixed value) defines the following equations:

$$\nabla \cdot E_s = \frac{\rho_e}{\epsilon_o} \quad (5)$$

$$\nabla \times E_s = 0 \quad (6)$$

where ρ_e is the total charge density and ε_0 is the permittivity of free space. The induced electric field has zero divergence and its curl is finite, defined by Faraday's law:

$$\nabla \times E = -\frac{\partial B}{\partial t} \quad (7)$$

The Ohm's law remains the same when applied to a conducting fluid, only the electric field is measured in a frame moving with the local velocity of the conductor.

$$J = \sigma(E + u \times B) \quad (8)$$

where J is the current density, u is the local velocity of the conductor and σ is the electrical conductivity.

The volumetric version of the Lorentz equation, when applied to a unit volume of a conductor [12] is:

$$F = \rho_e E + J \times B \quad (9)$$

where F is the force per unit volume acting on the conductor and ρ_e is the charge density within the conductor.

The Ampere-Maxwell equation gives information about the magnetic field generated by a given distribution of current [12]:

$$\nabla \times B = \mu[J + \varepsilon_o \frac{\partial E}{\partial t}] \quad (10)$$

where μ is the permeability of free space. The last term in the above equation was introduced by Maxwell as a correction to Ampere's law and is called displacement current.

1.7.3 Maxwell's equations for MHD

For materials that are neither magnetic nor dielectric, the Maxwell's equations are defined by the following four equations [18]:

1. Gauss's Law:

$$\nabla \cdot E = \frac{\rho_e}{\epsilon_o} \quad (11)$$

2. Solenoidal nature of B:

$$\nabla \cdot B = 0 \quad (12)$$

3. Faraday's law in differential form:

$$\nabla \times E = -\frac{\partial B}{\partial t} \quad (13)$$

4. Ampere-Maxwell equation:

$$\nabla \times B = \mu \left[J + \epsilon_o \frac{\partial E}{\partial t} \right] \quad (14)$$

In addition to these four equations, we have the charge conservation equation (equation 15) and the Lorentz force equation (equation 16) [18, 19]:

$$\nabla \cdot J = -\frac{\partial \rho_e}{\partial t}$$

$$F = q(E + u \times B)$$

$$(15)$$

In MHD, the charge density ρ_e and the term $\frac{\partial \rho_e}{\partial t}$ are negligible. Also the displacement

currents are negligible by comparison with the current density J and so the Ampere-Maxwell equation reduces to the differential form of Ampere's law. Hence the above Maxwell equations can be reduced to the following equations, used in MHD [18, 19]:

$$\nabla \times B = \mu J$$

$$\nabla \cdot J = 0$$

$$(17)$$

$$\nabla \times E = -\frac{\partial B}{\partial t}$$

$$(18)$$

$$\nabla \cdot B = 0$$

$$(19)$$

$$J = \sigma(E + u \times B)$$

$$(20)$$

$$F = J \times B$$

$$(21)$$

The above equations are the required basic equations of electromagnetism for MHD.

1.7.4 Different categories of fluid flow

Fluid mechanics and fluid flows are often divided into three broad sub-categories [23]:

1. A fluid may be treated as inviscid and the finite velocity must be taken into account. Viscosity and shear stresses are important close to solid surfaces and less important at a large distance from them.
2. There is a sub-division between laminar (organized) and turbulent (chaotic) flow. Low speed or very viscous flows are stable to small perturbations. High speed or almost inviscid flows are unstable to the slightest perturbations and rapidly develop a chaotic component. So when the fluid flows in parallel layers with no disruption between the layers, the flow is said to be laminar and when the flow is characterized by semi-random, stochastic changes then the flow is said to be turbulent.
3. The third sub-division is between irrotational (potential) and rotational flow. Turbulent flows and boundary layers are always rotational.

Before describing the Navier-Stokes equations, a few common terms used in fluid dynamics are defined [23]. A fluid problem is compressible if the pressure variation in the flow is large enough to affect the density of the fluid. For incompressible flows, the partial differential equation is:

$$\nabla \cdot u = 0 \quad (23)$$

where u is the fluid velocity. If the shear stress of a fluid is linearly proportional to the velocity gradient in a direction perpendicular to the plane of shear then the fluid is defined as a Newtonian fluid. The constant of proportionality is defined as viscosity. The equation describing the Newtonian fluid is:

$$\tau = \mu \frac{dv}{dx}$$

(24)

where τ is the shear stress exerted by the fluid, μ is the fluid viscosity and dv/dx is the velocity gradient perpendicular to the direction of shear. Regardless of the forces acting on the fluid, a Newtonian fluid always has a flow velocity.

1.7.5 Governing equations of Fluid Dynamics - Navier-Stokes equations

Navier-Stokes equations are a set of equations that describe the motion of fluid [18, 23, 24]. These equations state that changes in momentum of fluid particles are the product of changes in pressure and dissipative viscous forces acting inside the fluid. The equations describe the changes in linear momentum of a small element of fluid as it progresses through a flow field. Let p be the pressure, τ_{ij} the viscous stresses acting on the fluid and ν the kinematic viscosity. The net pressure force acting on the surface of a fluid element plus the net force arising from the viscous stress is equal to the mass of the element multiplied by its acceleration Du/Dt (Newton's second law).

$$(\rho \delta V) \frac{Du}{Dt} = -(\nabla p) \delta V + \left[\frac{\partial \tau_{ij}}{\partial x_j} \right] \delta V \quad (25)$$

Considering the fluid to be incompressible and Newtonian, the above equation yields the conventional form of Navier-Stokes equation:

$$\frac{Du}{Dt} = -\nabla(p/\rho) + \nu \cdot \nabla^2 u \quad (26)$$

The boundary condition on u is that $u=0$ on any stationary, solid surface. This is the 'no-slip' condition.

1.7.6 Magneto Fluid Dynamics Parameters

There are four dimensionless terms that are used frequently in MHD. These four terms are described below:

1. Reynolds number [15, 23, 36]: Re is the ratio of inertial forces $(u \cdot \nabla)u$ to viscous forces $\nu \cdot \nabla^2 u$. This parameter is used for determining whether a flow will be laminar (low Re) or turbulent (high Re). In equation 27, l is a characteristic length scale of motion and u is the typical velocity.

$$Re = ul / \nu \quad (27)$$

2. Interaction parameter N [25, 36]: This parameter is relevant in situations where J is primarily driven by Ohm's law. In such a case, N represents the ratio of Lorentz force to inertia. N is defined by the following equation, where τ is the magnetic damping time.

$$N = \sigma \cdot B^2 \cdot l / \rho \cdot u = l / u \cdot \tau \quad (28)$$

3. Hartmann Number Ha [25, 36]: Ha is the ratio of magnetic force to the viscous force. $(Ha)^2$ represents the ratio of the Lorentz force to viscous forces. Ha is defined by the equation:

$$Ha = (N \cdot Re)^{1/2} = Bl(\sigma / \rho \nu)^{1/2} \quad (29)$$

4. Magnetic Reynolds number [15, 23]: R_m is the ratio of fluid flux to the magnetic diffusivity. It is a measure of the effect of the flow on the magnetic

field. If it is very small compared with unity, the magnetic field is not distorted by the flow. If it is very large, the magnetic field moves with the flow and is called frozen-in. It is defined by the equation:

$$R_m = ul / \lambda = \mu \cdot \sigma \cdot u \cdot l \quad (30)$$

1.7.7 Incorporating Lorentz force into the Navier-Stokes - MHD equations

The MHD equations for an incompressible fluid, assuming no displacement currents are presented below [23, 18]. The boundary conditions are the usual requirement that the velocity and the induced magnetic field are zero at the wall. Hence, only pressure will be a function of the direction of flow.

$$\rho(v \cdot \nabla)v - \mu_e(H \cdot \nabla)H = -\nabla(p + \frac{\mu_e H^2}{2}) + \mu \cdot \nabla^2 v \quad (31)$$

$$\mu_e \cdot \sigma \cdot \nabla \times (v \times H) + \nabla^2 H = 0 \quad (32)$$

$$\nabla \cdot v = 0 \quad (33)$$

$$\nabla \cdot H = 0 \quad (34)$$

These equations will be used later to compute the voltage induced in the aorta due to flow of blood in it, in the presence of the static magnetic field.

1.8 Pulse Oximeters

The induced voltage in the MRI is due to the flow of blood (electrical charges) in the aorta in the presence of the static magnetic field of the MRI. This induced voltage is proportional to the volume of blood flow in the aorta. To determine the induced voltage it is essential to know the blood volume pulse in the aorta. One method to determine this is to use the waveform, photo-plethysmogram, obtained from the pulse oximeter in addition to the blood oxygen saturation digital readout [26, 27]. MRI compatible pulse oximeters are readily available in the market (INVIVO Research 4500 pulse oximeters [28]). This section describes the basics of a pulse oximeter.

Pulse oximeters have become an essential monitoring tool in the practice of emergency medicine. The degree of accuracy and the ease of operation have led to the widespread use of these devices for monitoring patients in intensive care unit (ICU). These devices measure the arterial oxygen saturation of hemoglobin. They are based on spectral analysis and use the following two physical principles:

1. A pulsatile signal is generated by arterial blood which is relatively independent of non-pulsatile arterial, venous and capillary blood and also the other tissues.
2. Oxy-hemoglobin and reduced hemoglobin have different absorption spectra.

The pulse oximeters use two light emitting diodes (LEDs) that emit light at 660 nm (red) and 940 nm (infrared) wavelengths. Oxy-hemoglobin and hemoglobin have different absorption spectra at these particular wavelengths. Oxy-hemoglobin absorbs less light

than hemoglobin (roughly ten times) in the red region and the reverse occurs in the infrared region. The concentration of an absorbing substance in solution can be determined from the intensity of light transmitted through that solution. The pulse oximeter probe emits light through a vascular bed, either the digits or ear lobe. A photodiode detector at the other end measures the intensity of transmitted light at each wavelength. The ratio of the red signal to the infrared signal measured is related to the ratio of reduced hemoglobin to oxygen hemoglobin, which is then converted to oxygen saturation [26, 27].

Absorbance of light by other tissue and blood components provides a hindrance to measure the oxygen saturation. To solve this problem, the pulse oximeter measures the light at the rate of several hundred times per second and hence distinguishes the variable, pulsatile component of arterial blood from the static component of the signal. The static component is cancelled. The pulsatile component is used to measure the oxygen saturation. When the arterial blood oxygen saturation is 90% or above, oximeters have a mean difference of less than 2% and standard deviation of less than 3% [27]. If the oxygen saturation level falls to 80% or below, the accuracy of pulse oximeters deteriorates [26]. Overall the performance of a finger probe for oximetry is higher than that of other probes like an ear probe.

In addition to the digital readout of oxygen saturation, pulse oximeters display a plethysmographic waveform. The change in the morphology of this waveform is difficult to interpret. Although they resemble the pressure waveforms recorded from arteries, they

represent changes in the blood volume in the tissue bed. In a research paper published in the British Journal of Anaesthesia [29], the intravascular volume was changed by removal of 10% of estimated blood volume and was then followed by an equal volume replacement by Haemaccel. Changes in the plethysmographic waveform correlated perfectly with the changes in the blood volume [30]. A detailed description is provided in the later chapters.

1.9 Contributions

The aim of this research is to find a solution to obtain an artifact free ECG signal in the MRI. More specifically, this research aims to remove the T wave elevation introduced in the ECG signal due to the interaction of blood flow in the aorta with the static magnetic field of the MRI. The simulation model developed confirms that the blood flow in the aorta is the most significant factor responsible for the induced voltage. To date, this was shown clinically and has not been completely modeled.

The model computes the magnitude of induced voltage by considering various parameters such as the radius of the aorta, magnetic field strength, blood pressure and the orientation of the aorta with respect to the heart. The model is implemented as a simulation package that uses a graphical user interface (GUI), allowing the user to alter the parameters for each patient and finally see the artifact free ECG signal. Also another important contribution is a method developed to determine the cardiac output of the patient from the pulse oximeter waveform – photoplethysmogram (PPG).

The solution to this problem obtained by using the least mean square adaptive filter is extremely good. In addition to just using the adaptive filters, appropriate changes in cardiac output are also included in the correction model. This can be directly implemented in the ECG monitors. This will enable doctors to interpret the important ST segment of the ECG signal even when the patient is in the MRI. All the results are presented in detail in the later chapters.

1.10 Overview of Dissertation

In this chapter, the problem statement, the approach to solve the problem and the goal of the research are discussed. Also this chapter covers the basics of electrocardiography, magnetic resonance imaging, the interaction of electric charges with a static magnetic field, the magneto hydro dynamic equations and a brief description of the working of pulse oximeter and its importance in the research.

The next chapter, chapter two, reviews the literature related to this research. The chapter presents a brief description of the research work in this field and how this previous work will be used to solve the T wave elevation problem. The chapter deals with the electrical conductance properties of blood, the modeling of blood flow in the aorta and the available methods to determine the blood flow in the aorta or cardiac output. Different papers are reviewed that relate the blood flow in the aorta with the pulse oximeter output waveform. Another important topic in this chapter is the effect of magnetic field on blood

flow and the various experiments performed on animals to observe this T wave elevation problem. The last section discusses different simulation models of the heart that are used as a reference to develop the simulation package in this dissertation.

Chapter three is divided into two main sections – the first section explains the details of how the simulation package is developed. The model of the aorta developed and the various parameters considered are discussed in detail. The various methods leading to the computation of the induced voltage are presented step by step. The second section explains the linear adaptive filter and other digital signal processing techniques implemented to remove the T wave elevation artifact.

Chapter four consists of the results of the entire research. The linear adaptive filters' outputs and the output screen shots of the simulation package are presented. The performance of the adaptive filter and parameters available to the user in the GUI simulation package are discussed. The final chapter discusses the conclusions and the future work of this research. This chapter is followed by the appendix and the references.

CHAPTER 2

LITERATURE REVIEW

This chapter discusses the previous research work that is related to solving the T wave elevation problem. The importance of these papers and how these papers will be used in our research work is presented.

As discussed in the previous chapter the induced voltage is caused due to blood flow in the aorta in the presence of a magnetic field. Blood is a charge carrying fluid and the first section of this chapter discusses the basic properties of blood and the electrical conductivity of blood. As the research deals with the blood flow in the aorta, the next section discusses the nature of blood flow in the aorta and the various theories developed to model the blood flow in arteries.

An important parameter proportional to the magnitude of induced voltage is the cardiac output or the volume of blood in the aorta. Hence, the third section in this chapter discusses the available methods to determine the cardiac output. Different papers are reviewed that relate the blood flow in the aorta with various physiological parameters in the body. These papers are used to derive a relation between the cardiac output and the pulse oximeter waveform.

The next section discusses how the magnetic field affects the velocity, pressure and blood flow pattern in the arteries. Various experiments on animals have been performed to

analyze this and this topic is the next section in this chapter. The last section in this chapter discusses different heart simulation models. These simulation models are studied to be an aid in developing a simulation model for this research.

2.1 Blood and Blood Vessels

The average adult has about five liters of blood flowing through blood vessels, delivering essential elements, and removing harmful wastes [30]. Blood transports oxygen from the lungs to body tissue and carbon dioxide from body tissue to the lungs. Blood contains red blood cells (RBC) and white blood cells (WBC). These cells are responsible for nourishing and cleansing the body. Approximately 55 percent of blood is plasma [24, 30]. The liquid plasma carries the solid cells and the platelets, which help blood clot.

2.1.1 Properties of blood vessels

The quantities of interest for the blood vessels are average density, dimensions and elastic properties of the wall material. The density of blood vessels is considered the same as soft tissue and it varies between 1.0 and 1.2 [30]. Blood vessels are composed of four types of tissues – endothelial lining, elastin, collagen fibres and smooth muscle [24, 31]. Elastic deformations take place at substantially constant volume so that Poisson's ratio is close to 0.5. The primary function of the muscles is to provide active tension by contraction under physiological control and thereby changing the diameter of the blood vessel. Each of the tissues has a different elastic modulus and the effective elastic

modulus increases with blood pressure. Increase of stiffness of the arterial wall is accompanied by increase in the pulse-wave velocity. The typical data for human aorta [24] is given in table 2.

Table 2 Typical data for human aorta

Vessel	Diameter (mm)	Wall Thickness (mm)	Length (cm)
Ascending Aorta	32	1.6	4
Thoracic Aorta	20	1.2	16
Abdominal Aorta	19	0.9	16

2.1.2 Properties of blood

Blood consists of a suspension of a variety of cells in an aqueous solution. The whole blood density is between 1.05 and 1.06 g/cm³ [30]. The majority of the cells are red blood cells (about 5 million per mm³), which are responsible for the fluid dynamic behavior of blood. The viscosity of blood is several times that of water [30, 31]. In general, for arteries and veins, blood does not behave like a Newtonian fluid because of the suspended particles and also its viscosity depends on the conditions under which measurements are carried out [31].

In any flow analysis, it is essential to use a viscosity appropriate to that particular flow situation. The effects of shear stress and axial accumulation of cells on wave transmission and flow are small under the conditions found in the large arteries. Hence, in most large

arteries, blood can be considered to behave in a Newtonian fashion, and the viscosity can be taken to be as a constant, 4 centipoises [31].

2.1.3 Electrical conductance properties of blood in motion

Sigman et al. (1937) found a maximum change of 10% in conductivity of blood with a linear velocity increase from 0 to 40 cm/sec [33, 32]. Moskalenko et al. (1959) found the change in conductivity of blood due to motion to be in the range of 2-5% of the initial magnitude. In their experiments the sharpest electrical conductivity change occurred in the range of flow between 0 and 15 cm/sec. An increase in velocity of blood flow above 20 cm/sec did not cause a noticeable change in resistance [32].

Moskalenko et al. (1959) [34, 32] explained the increase in electrical conductivity of moving blood by assuming that the erythrocytes carry an electric charge on their surface and that their directed motion caused a convection current between the electrodes as a result of the change in surface area of the cells relative to the electrodes.

F.M. Liebman et al. (1961) [35, 32] showed that in rigid tubes the electrical conductance of blood varies with the blood velocity within certain limits. The change in conductance was independent of any increase in the blood volume but was related to the diameter of the tube and the velocity of the flow. The conductance changes in blood with velocity occur in such a way that the impedance pulse is synchronous with the velocity pulse. The change in the conductivity of blood due to velocity is brought about by the axial

accumulation of cells and the orientation of cells in relation to the vorticity (amount of circulation or rotation of the fluid) lines. The conductance change due to axial accumulation is shown to be of a much smaller magnitude than predicted theoretically. The larger the diameter of the tube the greater was the percentage change in conductance at any specific velocity [32].

2.1.4 Blood flow in the aorta

Normal arterial flow is laminar with secondary flows generated at curves and branches [31]. Arteries adapt and change with the varying flow and pressure conditions of blood flow. Heart pumps blood through a sophisticated network of branching tubes starting with the aorta. As the heart muscle contracts periodically, blood is pumped from the left ventricle into the aorta through the aortic valve [31]. The aorta, being elastic, expands when it receives blood at a rate faster than the rate at which it sends blood into the peripheral organs. Expanding an elastic vessel causes an increase of the circumferential strain and stress in the vessel wall. As a result, the blood pressure increases. The valve is closed; blood continues to flow from the aorta into the periphery. By this mechanism the blood flow in the aorta does not have a large swing of pressure as it has in the left ventricle.

The heart ejects and fills with blood in alternating cycles called systole and diastole, creating pulsatile conditions in all arteries. Blood is pumped out of the heart during systole and the heart rests during diastole. Pressure and flow have characteristic pulsatile

shapes that vary in different parts of the arterial system as shown in Figure 12 [31]. In the aorta, the velocity and pressure waveforms are shown in the ascending, descending and the abdominal aorta. The aorta provides a reservoir of high pressure during systole and diastole. Hence, the pressure waveform in the ascending aorta has the maximum value and decreases as blood flows to the different parts of the body. During diastole, when no blood is pumped out of the heart, the flow is zero or even reversed in some arteries but due to the pulsatile nature of blood flow the pressure does not go to zero.

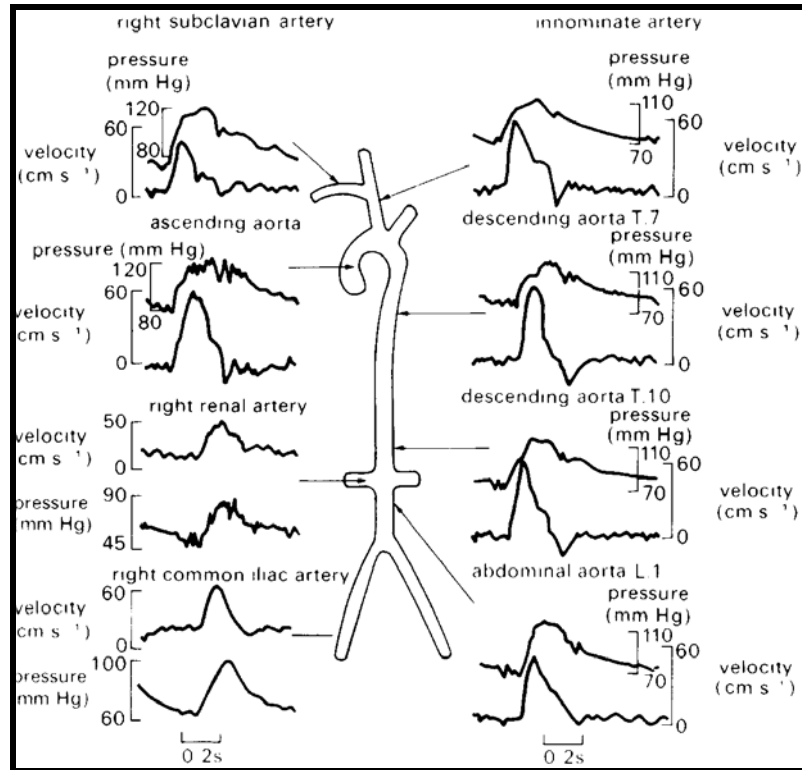


Figure 12 Pressure and velocity pulse waveforms in the aorta and arterial branches of a dog

2.1.5 Modeling blood flow in arteries

Any analysis of blood flow requires that the physical properties of blood and the blood vessels be known or assumed [15, 36]. Often adequate data is not available. In this section, some of the most common theories modeling blood flow in arteries are discussed. These models and theories will be used in our research to couple changes in blood flow, velocity, and cardiac output with changes in the T wave elevation in a magnetic field. Some most commonly used theories are presented below.

2.1.5.1 Windkessel Theory

The Windkessel model is used extensively because of its simplicity in interpreting pressure and flow behavior in arteries. Modern theories are developed as an improvement to the original Windkessel theory. In the Windkessel analysis, the amount of blood flow, Q_s , stored during each contraction, is the difference between inflow, Q_i , to the large arteries and the outflow, Q_o , to the small peripheral vessels [15].

$$Q_s = Q_i - Q_o \tag{35}$$

The aorta is represented by an elastic chamber and the peripheral blood vessels by a rigid tube of constant resistance. According to Equation 35, part of the flow is sent to peripheral vessels and part of it is used to distend the elastic chamber. Two important parameters defined are the peripheral resistance (R_s) and the compliance (C) [15]. At steady flow, assuming the venous side pressure drop to be small, the peripheral resistance is defined as the ratio of mean arterial pressure (\bar{P}) to mean arterial flow (\bar{Q}).

$$R_s = \frac{\bar{P}}{\bar{Q}} \quad (36)$$

The arterial compliance C represents the storage property of the artery. It is expressed as the amount in change in blood volume (dV) due to change in distending pressure (dP) in the artery.

$$C = \frac{dV}{dP} \quad (37)$$

The diastolic aortic pressure decay from end systolic pressure (P_{es}) to end-diastolic pressure (P_d) follows an exponential decay with a time constant τ . The time constant of pressure decay τ is defined by the product of resistance and compliance [36].

$$\tau = R_s \cdot C \quad (38)$$

Using the Windkessel model, the pressure in the aorta p is related to the blood flow from the left ventricle (Q) by the equation [36]:

$$p(t) = \exp\left(\frac{-t}{R_s \cdot C}\right) \cdot \int_0^t \frac{1}{C} \cdot Q(\tau) \cdot \exp\left(\frac{\tau}{R_s \cdot C}\right) \cdot d\tau + p_o \cdot \exp\left(\frac{-t}{R_s \cdot C}\right) \quad (39)$$

where p_o is the systolic pressure in the ventricle at the instant the valve opens.

2.1.5.2 Oscillatory blood flow in arteries

Three equations were formulated that characterize the propagation of blood flow in arteries [15, 36]. The velocity of blood flow is considered laminar in the vessel. The first of these equations describe fluid motion by relating the blood velocity in the longitudinal

direction with the pressure and density of blood. This equation implies that blood flow acceleration is proportional to the pressure gradient:

$$\frac{\partial v_z}{\partial t} = \frac{1}{\rho} \cdot \frac{\partial p}{\partial z} \quad (40)$$

where v_z is the blood velocity in the longitudinal z direction. p is the pressure. ρ is the density of blood. This equation is used to obtain blood flow from pressure gradient measurements.

The second is the equation of continuity, to describe the incompressibility of the fluid. This equation states that the blood flow velocity gradient is related to the rate of change in the cross-sectional area of the blood vessel.

$$\frac{\partial v_z}{\partial z} = \frac{1}{A} \cdot \frac{\partial A}{\partial t} = \frac{2}{r} \cdot \frac{\partial r}{\partial t} \quad (41)$$

where A is the cross sectional area of blood vessel and r is the inner lumen radius.

The third is the equation to describe the elastic properties of the wall. This equation states that the pressure-radius relationship remains constant (k) for the cardiac cycle.

$$\frac{\partial r}{\partial p} = k \quad (42)$$

From the above three equations, the pulse wave velocity (PWV) is thus derived as [22]:

$$PWV = \sqrt{\frac{E \cdot h}{2 \cdot r \cdot \rho}}$$

(43)

where E is the Young's modulus of elasticity for the vessel and 'h' is the wall thickness.

This equation can be used for the calculation of arterial pulse wave velocity when the geometry and elasticity of the artery are known.

In the arterial system, the velocity profile is relatively flat or blunt at the ascending aorta or at the entrance of the arterial system [15, 36]. The flat velocity profile implies that the blood flow velocity across the artery is uniform. The flat profile becomes progressively parabolic when approaching smaller arteries. In a parabolic velocity profile, the centerline velocity is the highest and the velocity declines in a parabolic fashion towards the vessel wall. In this profile the velocity at the arterial wall is lowest.

2.1.5.3 Womersley's theory

Of the many linear theories for blood flow, the Womersley's theory is used extensively. A frequency dependent parameter used in this theory called the Womersley's parameter is defined by [15]:

$$\alpha_w = r \cdot \sqrt{\frac{\omega \cdot \rho}{\eta}} \quad (44)$$

where

$$\omega = 2 \cdot \pi \cdot f_h \quad (45)$$

where f_h is the heart rate, r is the arterial lumen radius, ρ is the density of blood and η is the viscosity of blood. This parameter represents the ratio of the movement of blood mass

to the flow resistance caused by blood viscosity. Womersley's parameter increases in magnitude with size of blood vessel and body weight.

This theory starts with a linearized Navier-Stoke's equation and utilizes an equation of motion of a freely moving elastic tube with homogenous and isotropic wall material. The theory assumes that the pulse propagation wavelength is much greater than the arterial lumen radius. Assuming arterial wall and blood densities to be equal, an equation for the pulse wave velocity (PWV) is derived.

$$PWV = \sqrt{\frac{r \cdot \rho}{h \cdot E} \cdot k_c} \quad (46)$$

where k_c is a function of the Bessel function, E is the Young's modulus of elasticity for the vessel and 'h' is the wall thickness.

2.2 Cardiac Output and Cardiac rate

The induced voltage in the aorta depends largely on the cardiac output or the volume of blood flow in the aorta. The cardiac output or the amount of blood ejected from the ventricles is a measure of the pumping ability of the heart [30]. It is determined by:

$$CO(ml / min) = CR(beats / min) * SV(ml / beat) \quad (47)$$

where CO is the cardiac output, CR is the cardiac rate and SV is the stroke volume. Cardiac output is related to the total blood volume in a given time period. An increased cardiac output can be caused by an increase in the cardiac rate or stroke volume. Cardiac

rate is based on the natural rhythm of the SA node. The stroke volume is regulated by three parameters – end-diastolic volume (EDV), contractility and total peripheral resistance.

It is essential to determine the cardiac output to compute the T wave elevation of the ECG signal in the MRI. As the cardiac output increases, the volume of blood in the aorta increases and hence more potential will be induced across the aorta. This results in a higher T wave elevation. Hence the cardiac output is directly proportional to the T wave elevation. To measure this cardiac output, the most widely used techniques are the velocity encoded, phase difference MRI (non-invasive), thermo dilution (invasive) and Doppler Ultrasound (non-invasive). These methods are discussed below.

2.2.1 Velocity Encoded MRI

An MRI system can be used to measure the cardiac output of a patient. The principle of velocity encoded, phase difference MRI is that hydrogen nuclei moving through a magnetic field gradient accumulates a phase shift proportional to the velocity [11, 36, 37]. The flow is calculated by multiplying blood velocity by the cross-sectional area of the vascular structure, ascending aorta in this case. It takes about 1 to 2 minutes to calculate the blood flow using this technique [11]. For a normal patient the blood flow can be calculated before taking the MRI images of the body part of interest.

The RF system of the MRI causes the hydrogen protons to spin in a particular direction. The hydrogen protons moving in a magnetic field acquire a shift in their phase of rotation in comparison to stationary spins. The amount of this phase shift is proportional to the velocity of the moving spin. For stationary tissue, a bipolar magnetic gradient is used and this produces the required phase shift. By repeating the measurement with an inverted bipolar gradient, phase shifts induced by other sequence parameters are eliminated. The phase difference that remains after subtraction of these two data sets is used for a calculation of the velocity profile.

Before any measurement is started, the sequence is tuned to the maximum peak velocity expected in the blood vessel of interest (aorta). The tuning is necessary since the phase shift values should be within a range of 180° . The peak velocity now corresponds to a phase shift of 180° . The velocity v can be determined by the phase difference acquired in the two interleaved measurements:

$$\Delta\Phi = \gamma \cdot \Delta m \cdot v \quad (48)$$

where γ is the gyromagnetic ratio of hydrogen (42.59 MHz/Tesla) and Δm denotes the difference of the first moment of the gradient-time curve.

Velocity encoding (V_{enc}) is given in centimeters per second [36, 38]. It determines the highest and lowest detectable velocity encoded by a phase-contrast MRI image. The velocity encoding parameter is inversely related to the area of the flow-encoding gradients. The imaging time is going to be different for different velocities. But to keep

the time constant, stronger gradient amplitudes are used to encode smaller velocities. It is the transverse component of the spin magnetization that can acquire a motion-induced phase shift. Therefore, it is necessary to first induce a transverse magnetization with the help of the RF pulse before the flow-sensitizing gradients can be applied.

In the phase-contrast measurement technique, some parameters need to be considered to keep the overall error minimum. An optimum value of the encoding velocity needs to be selected. To have a precise measurement, the encoding velocity should match the real velocity in the region of interest. Setting the encoding velocity below the peak velocity in the vessel of interest results in wrapping around of velocity information within a voxel (aliasing) [37, 38]. Measurements of flow are most precise if the imaging plane is positioned orthogonal to the main direction of flow and through plane flow encoding is used. Other parameters that play an important role are the spatial and temporal resolution, accelerated flows, spatial mis-registration and phase offset errors.

For the ascending aorta, the encoding velocity is approximately 200 cm/sec [11]. The imaging plane is selected on an oblique sagittal localizing image that shows the ascending aorta at the level of the pulmonary bifurcation.

This technique requires the MRI system to acquire dedicated images of the heart to determine the cardiac output. But in our research, a method needs to be developed that can continuously measure the cardiac output without the continuous engagement of the MRI scanner.

2.2.2 Thermo dilution

Thermo dilution is a technique for measuring cardiac output by monitoring temperature changes over time. A known amount of cold liquid (e.g. 10 ml of sterile, ice-cold isotonic 0.9 % saline) is injected into the right atrium. The injection is made into a proximal port of a catheter containing a thermistor mounted at the tip. The solution cools blood as it passes into the ventricle and the change in temperature is plotted over time. The cardiac output is inversely related to the area under the thermo dilution curve. Thermo dilution is an invasive technique that can be repeated at short intervals [37, 38]. This technique has been used in majority of the major clinical studies related to the field of pulmonary hypertension. This method is limited due to its invasive nature.

2.2.3 Doppler Ultrasound

A Doppler ultrasound test uses reflected sound waves to evaluate blood as it flows through a blood vessel [38]. It can show blocked or reduced blood flow through narrowing in the major arteries that could cause a stroke. During Doppler ultrasound, a handheld instrument (transducer) is passed lightly over the skin above a blood vessel. The transducer sends and receives sound waves that are amplified through a microphone. The sound waves bounce off solid objects, including blood cells. The movement of blood cells causes a change in pitch of the reflected sound waves (called the Doppler effect). If there is no blood flow, the pitch does not change. Information from the reflected sound

waves can be processed by a computer to provide graphs or pictures that represent the flow of blood through the blood vessels. The cardiac output can be derived from this blood flow information. These graphs or pictures can be saved for future review or evaluation.

An approach for measuring the continuous blood pressure based on Doppler ultrasound uses the blood pressure cuff and an ultrasound Doppler device [38]. A normal upper arm cuff is used and the tube is connected to a servo system which receives signals from the Doppler ultrasound. The Doppler ultrasound is placed proximal to the blood pressure cuff and measures the blood flow into the artery under the cuff. The pressure in the cuff is recorded by a pressure transducer. The cuff is inflated above the systolic pressure. The servo system is designed to maintain a low flow under the cuff throughout the heart cycle (the transmural pressure will be maintained close to zero). The arterial wall is then in balance between the pressure inside and the cuff. The artery is continuously in a partially constricted state. When the cuff is wide enough so that the pressure in its bladder is transmitted without significant loss to the outside artery, the pressure in the cuff represents arterial blood pressure. Hence the above process consists of three phases:

1. The first phase corresponds to the state of the arm before the cuff is inflated. Then the pressure in the cuff is raised above the systolic arterial pressure.
2. This will occlude the artery under the cuff. However, the instantaneous flow velocity is not zero proximal to the cuff but oscillates around zero.
3. In phase three, the flow in the artery is restricted and the instantaneous pressure in the cuff corresponds to the intra-arterial pressure.

The continuous blood pressure waveform obtained by this method is very accurate and matched perfectly when compared to invasive readings.

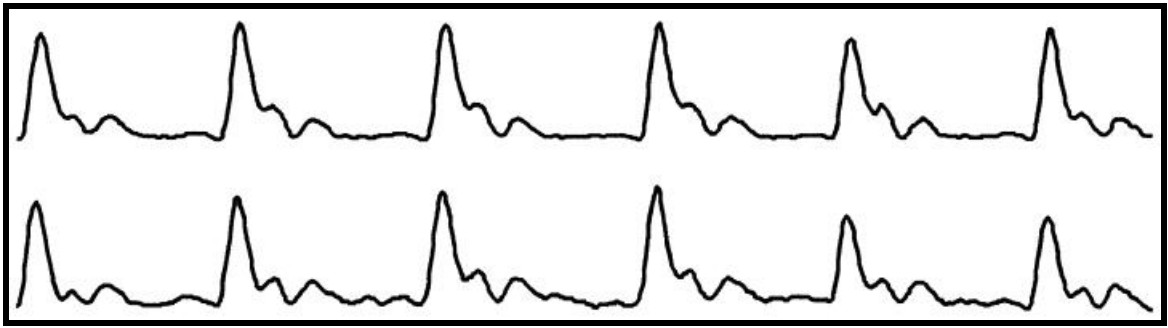
These three methods are standard methods of measuring the cardiac output of a patient. Each method has its own advantages and disadvantages. A better method is needed to measure the cardiac output that is simple and continuous. From this data, the effect of cardiac output on T wave elevation can be measured and be removed during an MRI procedure.

2.3 Relation between blood volume in the finger and cardiac output

The above methods described for measuring the cardiac output are direct methods. These methods are difficult to implement in the MRI room due to the high magnetic field of the MRI, the inaccessibility to the patient in the MRI bore and the time it takes to acquire a phase encoded MRI image. The other approach to measure cardiac output is an indirect non-invasive method and uses the photo-plethysmogram waveform obtained from the pulse oximeter.

The photo-plethysmogram is obtained from the pulse oximeters in addition to the digital readout of oxygen saturation [26, 27]. The change in the morphology of this waveform is difficult to interpret. Although they resemble the pressure waveforms recorded from arteries, they represent changes in the blood volume in the tissue bed. In a research paper

published in the British Journal of Anaesthesia [29], the intravascular volume was changed by removal of 10% of estimated blood volume and was then followed by an equal volume replacement by Haemaccel. Changes in the plethysmographic waveform correlated perfectly with the changes in the blood volume. Figure 13 shows the arterial flow waveform derived from pulse oximeter and the measured Doppler waveforms [39].



(Reproduced with permission from Wiley-Blackwell Publishing Limited.)

Figure 13 Comparison of derived arterial flow waveform (top) and the measured Doppler waveform (bottom).

From the blood volume waveform the blood flow waveform can be derived. If a value at a point in time represents volume then changes in the value represents flow. The total flow at any given time instant is calculated by the difference in the adjacent two values divided by 2 [40].

$$Q_t = (Vol_{t+1} - Vol_{t-1}) / 2 \quad (49)$$

where Q_t is the flow at time instant 't', Vol_{t+1} and Vol_{t-1} are the volumes at time instant 't+1' and 't-1' respectively. The arterial flow waveforms from pulse oximetry have been

compared with the measured Doppler flow waveforms. The similarity of the derived arterial flow to the measured Doppler flow is very clear [39, 40].

The various research papers used for relating the cardiac output and the plethysmogram are discussed below. The relation between the cardiac output and the blood volume in the finger can be sub-divided into the following relations:

1. Relation between the aortic blood flow (cardiac output) and blood pressure in the aorta.
2. Relation between the blood pressure in the aorta and the blood pressure in the finger.
3. Relation between the blood pressure in the finger and the blood volume pulse measured from a pulse oximeter.

The aim is to develop a model that directly relates the blood volume in the finger (PPG) to the cardiac output by integrating the above models with the necessary changes in each model. The system is an integration of subsystems, shown below:

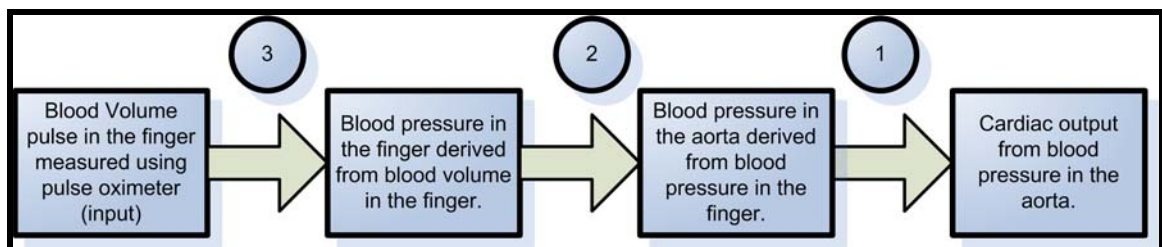


Figure 14 Relation between blood volume pulse in finger and cardiac output.

Various models have been developed relating the above parameters. These models are described briefly in the next sections.

2.3.1 Relation between the aortic blood flow (cardiac output) and blood pressure in the aorta

The aortic blood flow or cardiac output can be determined by measuring the pulse wave velocity (PWV) of the blood in the aorta [16, 17]. The motivation behind this research is that the pulse wave velocity gives us the velocity profile of blood flow in the aorta. This profile can be directly used in the Lorentz's equation to calculate the voltage induced by the magnetic fields in the ECG signal. Hence if a method of measuring the PWV of the patient in the MRI environment can be devised, then it can be used to provide a continuous measure of the cardiac output. Also when integrated over a single heart beat it can provide the stroke volume and when integrated over a minute it can provide the cardiac minute volume.

The pulse wave velocity increases when the cross-sectional area of the artery decreases or the distensibility or compliance of the artery decreases. Compliance is defined as the ratio of change in volume to the change in pressure. Typical PWV in the aorta is 3 to 5 m/s, in the subclavian or femoral artery is 7 to 9 m/s and 15 to 40 m/s in small arteries [41]. PWV can be measured by measuring the difference in arrival of the pulse wave at two different locations on the artery, for example, the wrist and the end of the middle finger. The time difference between the R wave of the subject's ECG and the onsets of the pulse

wave at the wrist and at the end of the middle finger is a measure of the time it takes the pulse wave to move between those two points. The distance between these two points divided by the time measured is the pulse wave velocity of that artery. This method of determining the blood pressure is patented (patent number 5,865,755) [42].

The use of PWV as a continuous measure of blood pressure changes is outlined in a research paper published in “The society for psycho-physiological research” by Brian Gribbin, et. al.(1976) [17]. An experiment was carried out to prove the theoretical consideration that changes in the PWV reflect changes in the blood pressure. PWV along an arm artery was monitored in 26 subjects at a time when the arterial distending pressure of the limb was altered over a wide range by means of externally applied positive and negative pressures. The research was based on the fact that the PWV is the rate of propagation of pressure pulse waves along arteries and short term changes in the parameter are due primarily to alterations in blood pressure. The velocity with which a pressure wave travels along an artery is determined by the dimensions and true compliance or distensibility of the artery. The arteries and arterial segments become progressively more resistant to stretch (less distensible) at higher distending pressures. The results obtained in this research strongly supports the hypothesis that changes in PWV can be used to detect and to follow changes in blood pressure. Its application is limited to situations where the change in blood pressure is of interest and not the absolute value.

In another research work by L. A. Geddes, et. al. (1981) [43] the pulse transit time, which is the difference in time between two pulses detected at different distances from the heart, is found to decrease with increasing blood pressure. The method employed to measure the pulse transit time measures two arterial pulse pickups located at different distances from the heart. From the pulse transit time, the PWV is computed as an inverse relation and the relationship between the PWV and the diastolic pressure is found to be very nearly linear. The method used for the measurement of pulse transit time has two disadvantages: firstly, it is difficult to monitor continuous trains of artifact-free pulses from two sites and secondly the interval between them is very short. These problems were overcome by Andrew Steptoe, et. al. [44] by dispensing with the proximal pulse detector and using the R wave of the ECG as the central trigger. Also the pulse transit time does not bear an inverse relation with the PWV. There could be a delay due to intra-cardiac events such as electrical depolarization, iso-volume contraction, the opening of semi-lunar valves and the expulsion of blood. The final results obtained in this research also suggested a very high correlation between the PWV and mean arterial pressure.

All research papers discussed above and many others confirmed the high correlation between the PWV and the blood pressure but none of them dealt with an actual mathematical relationship between the two. In the work by K H Wesseling, et. al. (1993) [16] a nonlinear, three element model is developed for the computation of aortic flow from pressure. The model elements represent aortic characteristic impedance, arterial compliance and systemic vascular resistance. Parameter values for the first two elements are computed from an age-dependent aortic pressure-area relationship. Peripheral

resistance is predicted from the mean pressure and model mean flow. Once model parameters are found, the flow can be computed from measured pressure by simulating the model. To evaluate the accuracy of the model, the results were compared with thermo dilution cardiac output estimations. The mean difference was $\pm 7\%$. But after using one comparison per patient to calibrate the model, the mean difference was reduced to $\pm 2\%$ with a SD of 8% [16]. Given these small errors the method could be used to monitor cardiac output continuously.

The first model parameter – aortic characteristic impedance (Z_0) is a dynamic property of the aorta that impedes pulsatile outflow from the ventricle. It is defined by the equation:

$$Z_0 = \sqrt{\frac{\rho}{A \cdot C'}} \quad (50)$$

ρ is the density of blood, A is the cross-sectional area of the aorta and C' is the aortic compliance per unit length. C' is the derivative of the pressure-area relationship with respect to the pressure (P). It is defined by:

$$C' = \frac{dA}{dP} \quad (51)$$

The second parameter – windkessel or buffer compliance (C_w) is the ability of the aorta and the arterial system to elastically store the cardiac stroke output from the left ventricle. The value is assumed to be equal to the compliance per unit length times the effective length of the aorta.

$$C_w = l \cdot C'$$

(52)

The third parameter – peripheral resistance (R_p) is the Poiseuille resistance of all vascular beds together. The first two parameters can be computed based on the precise and detailed results on the visco-elasticity of the human aorta available in the form of pressure-area relations. The third parameter, R_p is defined as the ratio of average pressure to average flow. Its value changes only slowly compared with a heart beat interval. Hence the current computed value is used to simulate the flow of the next beat. At the start of the simulation a reasonable initial value is assumed. From true mean pressure and computed mean flow the next approximation is computed.

The model flow is finally computed by simulating the behavior of the model under the applied arterial pressure pulsation as shown in figure 14. The model behavior is non-linear. Simulation is done digitally and model computations are repeated for each new pressure sample taken. The cardiac output is computed by multiplying the stroke volume with instantaneous heart rate. The heart beat interval is derived from the pressure waveform [16].

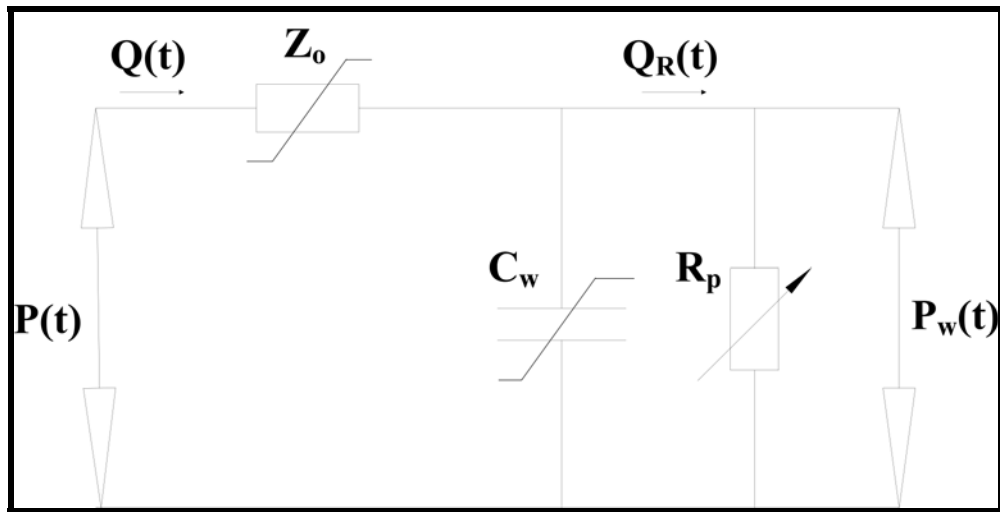


Figure 15 Three element model to compute flow.

The symbols in the circuit are defined below:

Z_0 : Aortic characteristic impedance.

C_w : Windkessel or buffer compliance.

R_p : Peripheral resistance.

$Q(t)$: Blood flow as a function of time.

$P(t)$: Arterial pressure waveform.

$P_w(t)$: Windkessel pressure.

Model flow computed from aortic pressure shows typical characteristics of an aortic flow pulsation: steep upslope at the beginning of systole, a gradual down slope terminated in a steep final phase and sharp dicrotic notch at end systole, followed by a period of almost zero flow in diastole. The model flow method extracts precise cardiac output information from arterial pressure. The aortic pressure-area relation is a useful approximation of aortic nonlinearity. Radial artery pressure can be used to compute beat-to-beat values,

although aortic pressure provides a visually better model flow waveform. For highest accuracy and precision a calibration of the model parameters is required. The model flow method provides an accurate model to obtain the cardiac output and PWV from the arterial pressure. This model is implemented in MATLAB and the results are presented in the next few chapters.

2.3.2 Relation between the blood pressure in the aorta and the blood pressure in the finger

Conventional noninvasive blood pressure techniques record blood pressure in the upper limb, but the upper limb pressure waveform differs from the ascending aortic waveform under normal conditions, during exercise and respiratory maneuvers, and after vasodilation. To resolve these differences, several attempts have been made to synthesize the ascending aortic pressure pulse from various peripheral pulses [45 - 47].

At a given arterial location, the particular shapes of pressure and flow waveforms are dictated by the properties of the cardiovascular system (geometry, wall elasticity, peripheral impedances, heart rate, cardiac output, etc.). Various computer models are developed to study the transfer from periphery (e.g. finger) to aorta. Most of these models are based on the same set of governing equations – the integrated, one-dimensional continuity and momentum equations. Throughout the arterial system, at bifurcations, the pressure is assumed constant and continuity of flow is preserved. At the distal end of each terminal branch, terminal impedance (modified windkessel model) is used to account for

the cumulative effect of all distal vessels. The modified windkessel model accounts for both the resistive and the compliant effects of vessels. The geometrical properties of the arterial segments are specified by the length and the proximal and distal cross-sectional areas. The elastic properties of the arterial wall are specified by the volume compliance. The calculated waveforms match closely when compared with the experimentally determined waveforms published in the literature [45]. Some of the well established characteristics of arterial flow are evident. The phase shift between the pressure and flow is apparent. Also the amplification of the pressure pulse (even though the mean pressure is decreasing) as the waveform progress along the system is evident. The results compare well with the experimental data.

In a research paper by Mustafa Karamanoglu, et. al.[46], ascending aorta pressure waveforms were synthesized from finger arterial recordings in real time using convolution windows derived from transfer functions. A continuous transfer function is derived that takes the possible physical properties of the upper limb into account. For this purpose, a mathematical model of the human upper limb arterial system is constructed and linked with the carotid arterial model. The resultant combined model consisted of three viscoelastic tubes connected in series and terminated with a modified windkessel. The time-domain representation of the transfer function as a convolution window can be used in human adults to synthesize the ascending aortic pressure waveform from finger recordings in real time. This procedure could be used where aortic pressure waveform features are needed in real time on a beat-by-beat basis.

Various interesting models are studied to transfer the flow velocity waveform from the finger to the aorta. The ascending aortic pressure wave during systole is virtually identical to left ventricular pressure during ejection but both are quite different from the systolic part of the pressure wave as recorded in the brachial, radial, and other peripheral arteries. Such differences are attributed to wave travel and reflection in the systemic circulation and are substantial [47]. The models studied derived a generalized transfer function that relates the flow velocity in the finger to that in the aorta.

2.3.3 Relation between the blood pressure in the finger and the blood volume pulse measured from pulse oximeter

The photoplethysmogram (PPG), representative of the blood volume pulse, is related to the underlying arterial blood pressure. Two research papers [48, 49] suggest a static relationship while others use more complex dynamic characterizations [50]. The simplest model of the relationship between the blood pressure and the volume assumes a static sigmoid curve relating the two parameters [49]. The maximum compliance occurs when transmural pressure is kept near zero. The transmural pressure (P_{tm}) is defined as follows:

$$P_{tm} = P_{ABP} + P_{height} + P_{cuff} \quad (53)$$

P_{ABP} is the internal pressure, P_{height} is the external hydrostatic pressure, and P_{cuff} consists of any additional externally applied pressure. For a given pressure change, the volume change will be maximum when the transmural pressure is kept near zero. If the pressure-volume sigmoid curve were static, it would be easy to estimate blood pressure by using a calibrated plethysmogram signal. But the sigmoid curve may change as a function of time

and physiological state and also the pressure volume curve is dynamic, showing hysteresis.

Though there is no simple relation between the blood pressure and the volume pulse, many research papers have to a certain extent successfully developed a model relating the two parameters. In one of the research works by P. Shaltis, et. al. [49], the plethysmogram waveform is used to estimate the internal mean arterial pressure by finding the height at which the amplitude of the plethysmogram signal is maximum. Once a mean arterial pressure (MAP) is known, it is then possible to continuously estimate this pressure for all points of the plethysmogram waveform $[y_{PPG}(t)]$. A nonlinear calibration curve based upon the equation below is generated from a training set of data:

$$MAP_{est} = a \times \exp(b \times y_{PPG}(t)) + c \times \exp(d \times y_{PPG}(t)) \quad (54)$$

The above method was found to rapidly converge to unique parameters (a, b, c, d) for all subject data sets. After generation of the compliance curve a second test set of data from the same volunteer was utilized to validate the calibrated model.

One method to estimate continuous and non-invasive blood pressure that has been extensively studied uses pulse transit time (PTT). PTT is the time interval for the arterial pulse pressure wave to travel from the aortic valve to a peripheral site (e.g. finger). The peripheral pulse is measured using pulse oximeter and the time difference between the R peak of ECG and the peak of PPG waveform is considered as PTT. The pulse wave velocity is considered to be the inverse of PTT. The Moens-Kortweg equation, modified

by Bramwell and Hill (1922) relates the change in pressure (ABP) to the pulse wave velocity and the volume (PPG) in an elastic artery.

$$\Delta P \propto c^2 \times \left(\frac{\Delta V}{V} \right) \quad (55)$$

V is the initial volume of the artery, ΔV is the change in volume resulting in the pressure pulse ΔP and c is the pulse wave velocity (PWV). The change in volume and the initial volume are measured from the blood volume waveform. Hence the pressure pulse ΔP can be computed. The equation may require introduction of some calibration constants.

To determine the blood pressure from the PPG waveform, four features of PPG signals were analyzed by X. F. Teng, et. al. [50], namely, width of 2/3 pulse amplitude, width of 1/2 pulse amplitude, systolic upstroke time (t_1), and diastolic time (t_2). The accurate positions of the peak and the foot are important for determining the values of these features. In some PPG recordings, it is difficult to find the accurate position of the foot because of the poor signal quality. Continuous wavelet transform (CWT) was used to deal with this problem. Twice the heart rate frequency was selected as the scale of CWT and the mother wavelet was Mexican hat [50]. The feature that has the highest mean correlation coefficient with ABP was found to be the diastolic time (t_2), which is used in the further regression analysis. Linear regression line in the form of $y = a \cdot x + b$ was set up for systolic BP and diastolic BP with the data of six trials. Then the data of another six trials from the same subject were used to estimate blood pressure. There is inter-subject difference in the estimation results, because the cardiovascular parameters are different from subject to subject. Therefore, individual calibration is needed in reality.

In another research work by John Alley, et. al. (1998) [51], the relationship is derived using linear and neural network system identification techniques. The blood volume waveform is the input to the system and the blood pressure is the output of the system. Both the waveforms are measured and the transfer function of the system is determined. The blood volume waveform is obtained using a pulse oximeter and the finger arterial blood pressure waveform is obtained using a commonly used device called Finapres [52].

Finapres is a non-invasive continuous finger arterial blood pressure monitor, based on the vascular unloading technique. Finapres is the acronym for finger arterial pressure, the variable that is measured continuously by the Finapres [52]. With the volume-clamp method, the finger arteries are clamped at a fixed diameter, although intra-arterial pressure changes continuously, by applying an external pulsating pressure via an inflatable bladder mounted in a finger cuff and a fast acting servo system. The diameter at which the finger arteries are clamped is determined from an infrared plethysmograph mounted in the finger cuff such that transmural pressure is zero and intra-arterial and cuff pressure are equal both in shape and in level at all times. The more sophisticated neural network system identification technique performed better than the simpler linear system identification technique by providing a more accurate model fit.

2.4 Effect of magnetic field on blood flow

Blood is an electrical conducting fluid and the effect of magnetic field on blood flow is the study of magnetic field on a fluid charged to a particular charge density flowing with a particular velocity [53]. The Lorentz force is defined as the force exerted on a charged particle in a magnetic field. The particle will experience a magnetic field's exerted force and is given by the equation [12]:

$$F = q \cdot v \times B \quad (56)$$

where F is the Lorentz force, B is the magnetic field induction, q is the charge of the particle, v is its current velocity (vector) and x is the cross product. When applied to a fluid (with density ρ) that is charged with a charge density q per unit volume the body force per unit mass becomes [12]:

$$F = (v \times B) \cdot q / \rho \quad (57)$$

The force is perpendicular to both the velocity v of the charge q and the magnetic field B.

The magnitude of the force is:

$$F = q \cdot v \cdot B \cdot \sin \theta \quad (58)$$

The angle θ in the above equation is the angle less than 180 degrees between the velocity and the magnetic field [12]. This implies that the magnetic force on a stationary charge or a charge moving parallel to the magnetic field is zero.

The Reynolds Number is important in analyzing any type of flow when there is substantial velocity gradient - shear. The Reynolds Number indicates the relative

significance of the viscous effect compared to the inertia effect. The Reynolds number is proportional to inertial force divided by viscous force. The Hartmann number is the ratio of the magnetic force to the viscous force and is used to describe viscous magnetohydrodynamics channel flow. The effect of magnetic field on the flow of blood has been an interesting topic of research.

In one of the research works, V A Vardanyan [53] studied the blood flow in large arteries in the presence of a magnetic field. The artery is considered to be a round tube of constant cross-section with non-conducting walls. It is assumed that the blood flows under a certain pressure gradient and the speed of blood in the radial and azimuthal directions is zero. The blood flows in a direction parallel to the axis of the tube dependent only on the radius of the tube. The applied magnetic field is homogenous and is directed perpendicular to the flow. The movement of electric charges of the blood itself induces a magnetic field. But the Reynold's magnetic number for blood is much smaller than unity and hence this induced magnetic field is disregarded.

Working on the solution to the Navier-Stokes equation and considering strong magnetic fields (Hartmann number $\gg 1$), it is shown that with increase in the strength of the magnetic field the speed of blood flow and minute volume diminishes. The body may counteract the tendency of external factors by keeping the minute volume constant. But in such a case, the pressure gradient increases by either a fall in diastolic pressure or an increase in systolic pressure by an increase in the mechanical activity of the heart. The magnetic forces slow down the faster layers of fluid and accelerate the slower ones.

Figure 16 shows how the velocity profile changes from a parabolic profile [53]. Close to the walls of the tube, the gradient of the speed increases solely due to the action of viscous forces. On the basis of the above analysis, it is concluded that a very strong magnetic field is harmful to the body and could cause vascular disorders and can also influence the activity of the heart.

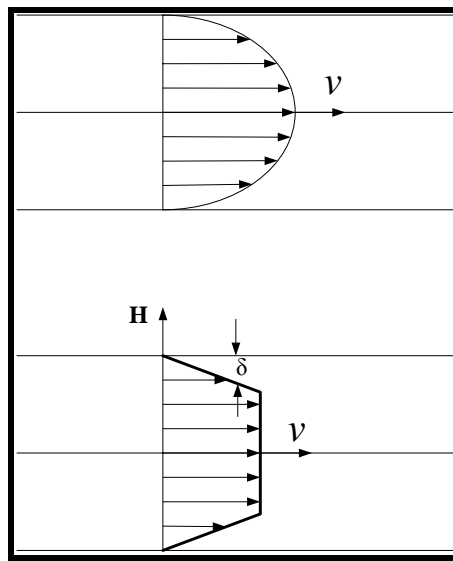


Figure 16 Change in the velocity profile of viscous conducting fluid when subjected to a magnetic field

E M Korchevskii, et. al. [54] performed an analysis on the movement of blood in a magnetic field with reference to the principle of “freezing in”, known in magnetic hydrodynamics. A tube of conducting fluid is surrounded by electromagnets through which currents shifted in phase are passed. By the principle of “freezing in” the lines of force of the magnetic field are sealed to the fluid and move together with it. Two points in the liquid present in a given line of force will continue to be present in the line of force, irrespective of the movement the liquid performs. If the fluid travels through the

tube at a speed less than the phase speed of the field, then by the principle of “freezing in” the lines of force of the field will accelerate the fluid. If the phase speed of the field is less than the speed of the fluid then the field reduces the speed of the fluid. According to the analysis presented, the magnetic field begins to exert an effect on blood flow when the criterion in the equation below is satisfied:

$$H \geq (2 \times 10^3 / a) \quad (59)$$

where H is the magnetic field in gauss and ‘a’ is the radius of the tube. The field begins to influence the character of blood flow at values of the order of 1000 gauss and above.

In another research paper by Y. Kinouchi, et. al. [55], a solution of the complete Navier-Stokes equation is obtained using finite element analysis for the assumption that the walls of the aorta are electrically conductive and not conductive. Also the propagation of the magnetically induced voltages to the neighboring tissues and the effect on the sino-atrial node is analyzed. Also the author discussed the reduction of blood volume flow at high magnetic fields of about 10 T. The magnetically induced voltage is quantitatively computed considering the aorta as cylinder of infinite and finite length. The results from this paper are discussed in the later chapters and compared with the results from the simulation package developed.

In summary, this chapter discusses several papers, theories and models that will be used as a reference for developing the T wave elevation simulation package. Based on the models for the blood flow in the arteries, our simulation model will model the blood flow

in the aorta and apply a static magnetic field to this blood flow. The section that describes the relation between blood volume in the finger and the cardiac output will be used to develop an easy method to measure the cardiac output and relate it with the T wave elevation magnitude. The next chapter continues the review of literature directly related to experiment on animals and simulation models. The chapter discusses the different experiments on animals performed to measure the effect of strong magnetic fields on blood flow and the effect on the T wave of the ECG signal. The result of the experiments on monkeys and rabbits are presented. Also the next chapter discusses different heart simulation models. These models are used as a reference to develop the simulation model to simulate the T wave elevation of ECG signal in the MRI.

CHAPTER 3

REVIEW OF EXPERIMENTS ON ANIMALS AND PRESENT MODELS

In this chapter, experiments on animals are discussed that study the effect of magnetic field on the ECG of the animals. Two particular results of experiments on monkeys [3, 57], rats [80] and rabbits [56] are presented. The results of the simulation model developed will be compared with these results. Also this chapter discusses different heart simulation models [58–64]. These models are used as a reference to develop the simulation model to simulate the T wave elevation of ECG signal in the MRI. Three models – a dynamic model of the cardiac electromechanical activity [58-60], a model to simulate the cardiac electrical activity [61] and a model that simulates the ECG signals on the thorax [62-64], are discussed. The model developed by A van Oosterom, et. al. [62-64], is of particular interest to this research. The outputs of these simulation models are also presented and their importance in this research is discussed.

3.1 Elevation of T wave in magnetic fields – experiments on animals

Changes in the ECG signal of several animals have been demonstrated when exposed to magnetic fields. This change has been observed in monkeys [3], baboons [57], rabbits [56], rats [65] and dogs [66]. Togawa, et. al. [56] experimented with rabbits by placing them in a static magnetic field of a maximum of 10,000 G to observe blood flow induced e.m.f (electromagnetic force). Figure 17 shows the ECG recordings with no magnetic

field, with 10,000 G field (upward deflection corresponds to descending flow) and with inverted 10,000 G field (upward deflection corresponds to ascending flow).

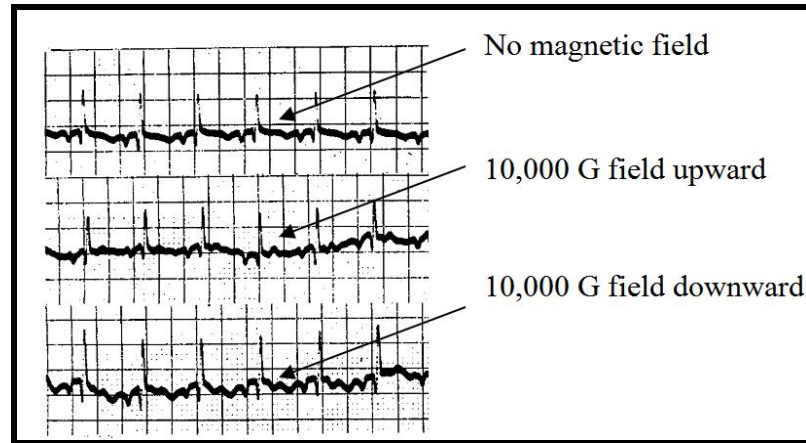


Figure 17 T-wave elevation in rabbits

When the magnetic field was applied in the direction from back to front, the ascending blood flow induced a current from left to right arm – an upward deflection in standard lead I of ECG [56]. The e.m.f induced on the surface of the blood vessel is expressed as:

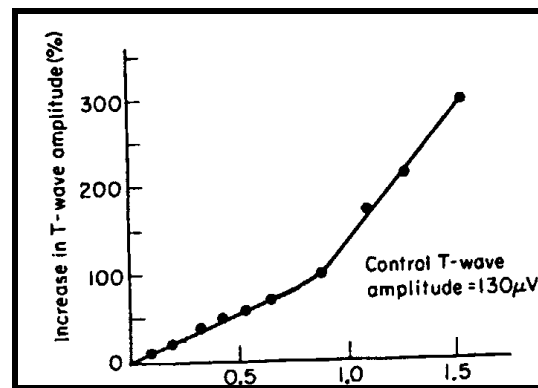
$$E = V \cdot B \cdot D \times 10^{-8} \quad (60)$$

where E in the e.m.f. in volts, V is the velocity of flow in cm/sec, B is the magnetic flux density in gauss and D is the internal diameter of the vessel in cm. The heart and main arteries contributed to the induced voltage.

When the body is placed in a magnetic field, all vessels and organs with a blood flow across the magnetic field polarize. With a magnetic field of 10,000 G, velocity of 50 cm/sec, an e.m.f of 8 mV is induced [56]. This induced voltage appeared between the S

and the end of the T wave. In another experiment, squirrel monkeys were placed in a strong magnetic field of up to 70,000 G for over 3 hours and no serious effect was observed. Also the change in pulse rate and ECG due to the magnetic field disappeared after the removal of the field [56].

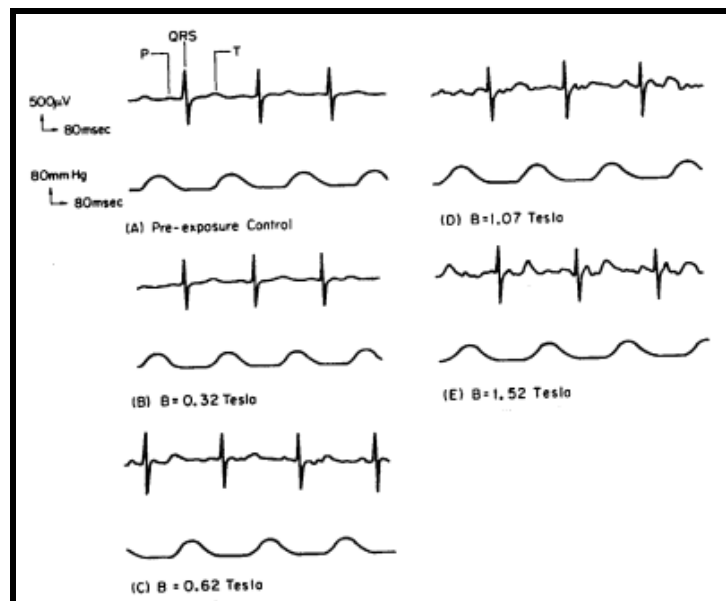
T. S. Tenforde, et. al. [1, 3] performed experiments to measure the magnitude of magnetically induced blood flow potentials and blood pressure changes in Macaca monkeys exposed to stationary magnetic fields up to 1.5 T. The subjects were placed in a reclining position, with the vertical lines of magnetic induction transverse to the longitudinal body axis. The ECG recordings were made using a conventional three-lead electrode configuration. An instantaneous, field strength dependent increase in the ECG signal amplitude at the locus of the T wave was noted. Figure 18 shows the percentage increase in T-wave amplitude as a function of field strength increase.



(Reproduced with kind permission of Springer Science and Business Media)

Figure 18 Percentage increase in T wave amplitude in Macaca monkeys as a function of magnetic field strength.

The increase in the T wave amplitude in Macaca monkeys was found to be reversible and there was no effect on the average heart rate or on the amplitudes of the P, Q, R and S signals. The increase in the T-wave amplitude results from an induced electrical potential associated with blood flow in the presence of a magnetic field. Due to the temporal nature of this magnetically induced potential the authors suggested that it is primarily associated with pulsatile aortic blood flow. Also a further superposition of a second induced flow potential was detected at high fields and this is associated with blood flow in the pulmonary artery [1]. The predominant affect a strong magnetic field has on an ECG is an increase in the T wave amplitude of the measured ECG.



(Reproduced with kind permission of Springer Science and Business Media)

Figure 19 Elevation of T wave for different magnetic fields (0 T to 1.52 T) in Macaca monkeys.

The intra-arterial blood pressures of the monkeys did not vary significantly during exposure to the stationary magnetic fields. It was concluded [1] that the magneto hydro dynamic interaction was too small to produce a measurable increase in blood pressure.

3.2 Simulation models of the heart

Many simulation packages have been developed to study the relation between the ECG, the potential on the heart surface and the potential on the thorax. A few models of interest are discussed below. M Sermesant, et. al. [58-60] developed a dynamic model of the cardiac electromechanical activity for the analysis of the time series of medical images and the simulation of cardiac function. The action potential is simulated using FitzHugh-Nagumo reaction- diffusion equations, enabling the introduction of pathologies and the simulation of surgical procedures.

Gunnar Seemann, et. al. [61] simulated the cardiac electrical activity and calculated the electrical fields on the body. An interactive user interface was created in order to control the simulation process and visualize the results. The electrical field in the body is determined by solving the forward problem of electrocardiology using generalized Poisson equation. The simulation comprises physiological and pathological behavior of the human heart.

A. Van Oosterom, et. al. [62-64] developed a simulation package (ECGSIM) for computing electrocardiographic signals on the thorax and also electrocardiograms on

endocardium and epicardium. The interesting features of this simulation are the use of equivalent double layer, a realistic thorax model and the feature of interactively changing the timings and the local source voltages. This research is of particular interest to the simulation model developed.

3.2.1 Electromechanical Model of the Heart

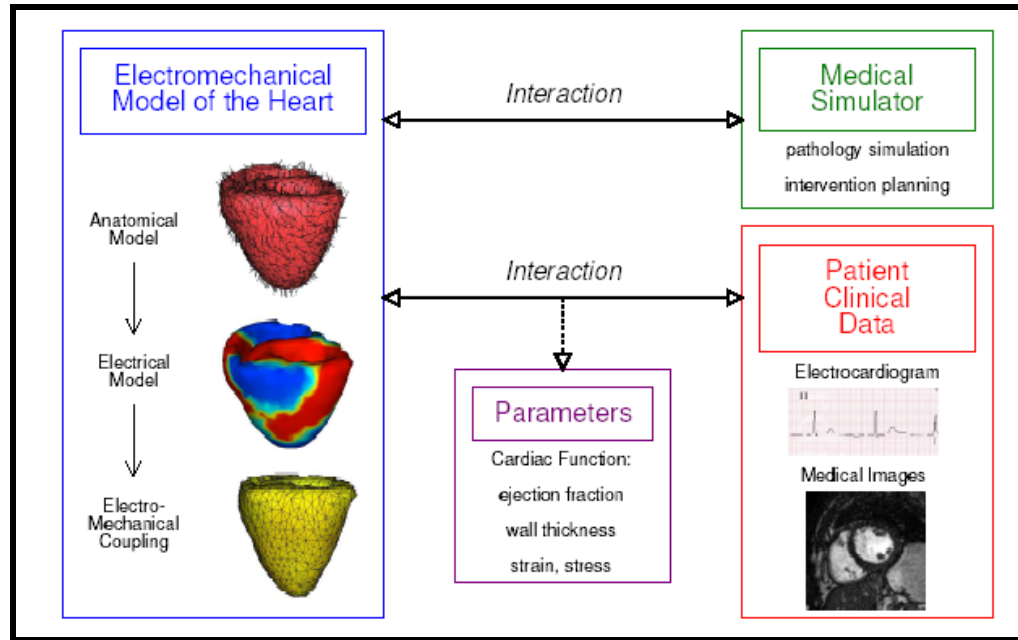
A dynamic model of the cardiac electromechanical activity for the analysis of the time series of medical images and the simulation of cardiac function is developed [58-60]. The project worked on building a generic deformable model of the beating heart and a procedure to automatically adjust the parameters to any specific patient from measurements like the ECG and volumetric medical images. A volumetric biomechanical model is built based on tetrahedral meshes. The action potential is simulated using FitzHugh-Nagumo reaction- diffusion equations, enabling the introduction of pathologies and the simulation of surgical procedures. The modeling is based on a multi-scale analysis ranging from microscopic to macroscopic and integrates a priori information on the overall geometry and on the fiber directions extracted from specific medical imaging techniques.

3.2.1.1 Anatomical Model

The myocardium is represented as a tetrahedral volumetric mesh including anatomical information – myocardium geometry, location of different anatomical parts and muscle

fiber directions [Figure 20]. From a 3D image of the heart, extracted from different medical image modalities, the myocardium is segmented using classical image processing methods like thresholding and mathematical morphology. Then, a triangulated surface is obtained (marching cubes method) and decimated to the required size. Finally a volumetric tetrahedral mesh is created. The muscle fiber direction (obtained from diffusion tensor MRI) is used for:

1. Preferential propagation directions for the electrical action potential propagation.
2. Transverse anisotropy direction in the passive elastic element of the mechanical constitutive model.
3. Direction of contraction stress in the contractile element of the mechanical constitutive model.



(Reproduced with kind permission of the author [58])

Figure 20 Electromechanical model construction, simulation of cardiac activity and clinical data analysis.

3.2.1.2 Electrical Model

The cardiac electrophysiology is simulated by computing the extra-cellular potentials, intra-cellular potentials and their difference - the action potential. The action potential wave propagation is simulated using a system based on modified FitzHugh-Nagumo model using the following assumptions:

1. A cell is activated only for a stimulus larger than a certain threshold.
2. The shape of the action potential does not depend on the stimulus.
3. Presence of a refractory period during which the cell cannot be excited.
4. The cell can act as a pacemaker.

The set of differential equations of the modified FitzHugh-Nagumo used are:

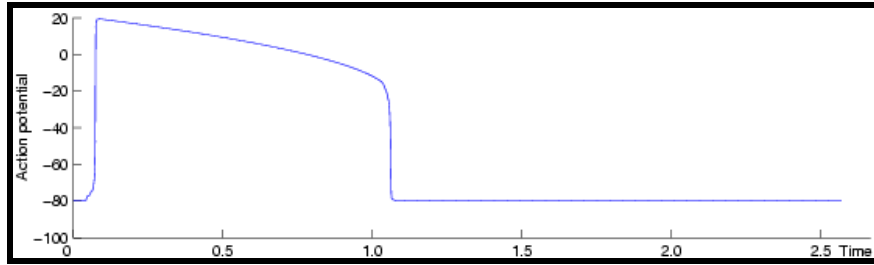
$$\partial_t u = \text{div}(D\nabla u) + ku(1-u)(u-a) - uz$$

$$\partial_t z = -\varepsilon(ku(u-a-1) + z)$$
(61)

(62)

where u is the normalized action potential, z is the secondary variable for repolarization, k and ε control the repolarization and a controls the reaction phenomenon. The parameter values derived from the above equations are: $\varepsilon = 0.01$, $k = 8$ and $a = 0.15$.

Action potential propagates twice as fast in the fiber direction than in the orthogonal direction. The simulated action potential generated by this model with an excitation above the initialization threshold is shown in figure 7.



(Reproduced with kind permission of the author [58])

Figure 21 One dimensional measure of action potential simulation.

3.2.1.3 Electromechanical Model

The electromechanical model is specifically designed for cardiac image analysis and simulation. The model can be directly compared with in vivo measures through medical images and thus making a validation possible. The model has:

1. A contractile element, which creates a stress tensor.
2. A parallel element, which is anisotropic linear visco-elastic and creates a stress tensor.

To control the coupling, the contraction intensity is directly controlled by the action potential. A solution to the following dynamic equation is used to perform the electromechanical simulations:

$$M \frac{d^2 U}{dt^2} + C \frac{dU}{dt} + KU = F \quad (63)$$

where U is the displacement vector, M is the diagonal mass matrix, C the Rayleigh damping matrix, K the anisotropic linear elastic stiffness matrix and F the different loads, including the stress tensor from the contraction.

3.2.1.4 Complete Cardiac Cycle Simulation

The interaction of myocardium with blood is very important for the simulation. Different phases of the cardiac cycle with different boundary conditions are used to simulate the entire cardiac cycle. The cardiac cycle is divided into four phases:

1. Filling: a pressure is applied to the vertices of the endocardium.
2. Isovolumetric contraction: a constraint is applied to keep the ventricular volume constant.
3. Ejection: a pressure is applied to the vertices of the endocardium.
4. Isovolumetric relaxation: a constraint is applied to the vertices of the endocardium, keeping the volume constant.

The succession of different phases is triggered by a synchronization mechanism based on a standard ECG. For the isovolumetric phases, the pressure is estimated as the stress required maintaining the volume constant. For the other phases, the valves can close when there is a change in flow direction (volume variation changes sign). This provided for continuity in the stress and more realistic simulations.

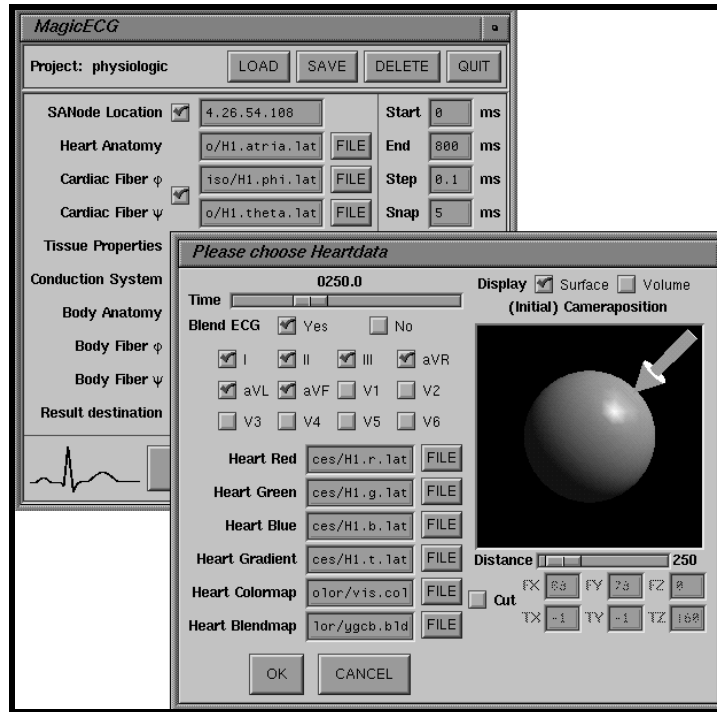
3.2.1.5 Simulated Cardiac Function parameters

The simulation performed includes the propagation of the action potential in the myocardium coupled with the mechanical contraction using different boundary conditions depending on the phase of the cardiac cycle. The volumes of the ventricles are determined during simulation and this sets the contractility parameter and maximum contraction. The inertia axis of the left ventricle is used to compute the local rotation of any point around this axis and the radial contraction (variation of distance from the axis) of any point of the myocardium during the simulated cycle. The electromechanical model is designed for medical image analysis and simulation and is validated using different global and local parameters and is then used for the segmentation of 4D medical image sequences. This model helps in understanding pathologies and introduces a priori knowledge on the cardiac motion improving the segmentation of medical image sequences.

3.2.2 Simulation Model of Cardiac Electrical activity

This package is developed to simulate the cardiac electrical activity and calculate the electrical fields in the human body [61]. This package is developed to serve as an aid in the diagnosis of cardiac pathologies and in medical education. The anatomical model of the heart is obtained from MEET Man project [67]. Tissue classification and muscle fiber orientation is created with the help of digital image processing. Various parameters such as excitability and velocity of propagation were added to form the physiological model. Cardiac source distribution is calculated from transmembrane potentials and the electrical field in the body is determined by solving the forward problem of electrocardiology using generalized Poisson equation. The electrocardiograms are obtained by subtracting potentials of two specific derivation points from the body surface potential maps.

The interactive tool is suitable for easily simulating and visualizing heart excitation and field distribution in the human body. It handles the whole simulation process – animations, images and ECGs. Electrical transmembrane potential distribution is presented in anatomical context with standard ECGs and color scale. Figure 8 shows the interactive user control. To study different pathologies, individual models need to be constructed.



(Reproduced with kind permission of the author [61])

Figure 22 Interactive user control – controls for simulation and visualization.

3.2.3 ECG Simulation Package - ECGSIM

ECGSIM is an interactive simulation program that enables one to study the relationship between the electric activity of the ventricular myocardium and the resulting potentials on the thorax: QRST waveforms as well as body surface potential maps [62-64]. From a default specified timing of depolarization and re-polarization of the trans-membrane potentials on the closed surface bounding ventricular mass, QRST waveforms are simulated. The program allows the interactive changing of the timing of depolarization and re-polarization as well as the magnitude of the upstroke of the local trans-membrane potentials.

Figure 23 shows a display of the ECGSIM window. The centre of the window displays the ventricular surface S_h showing the nodes, grids and the leads (four heavy dots). The color coded function on S_h is the timing of depolarization. Upper right corner consists of two waveforms – the simulated and measured ECG for a selected lead (lead II shown).

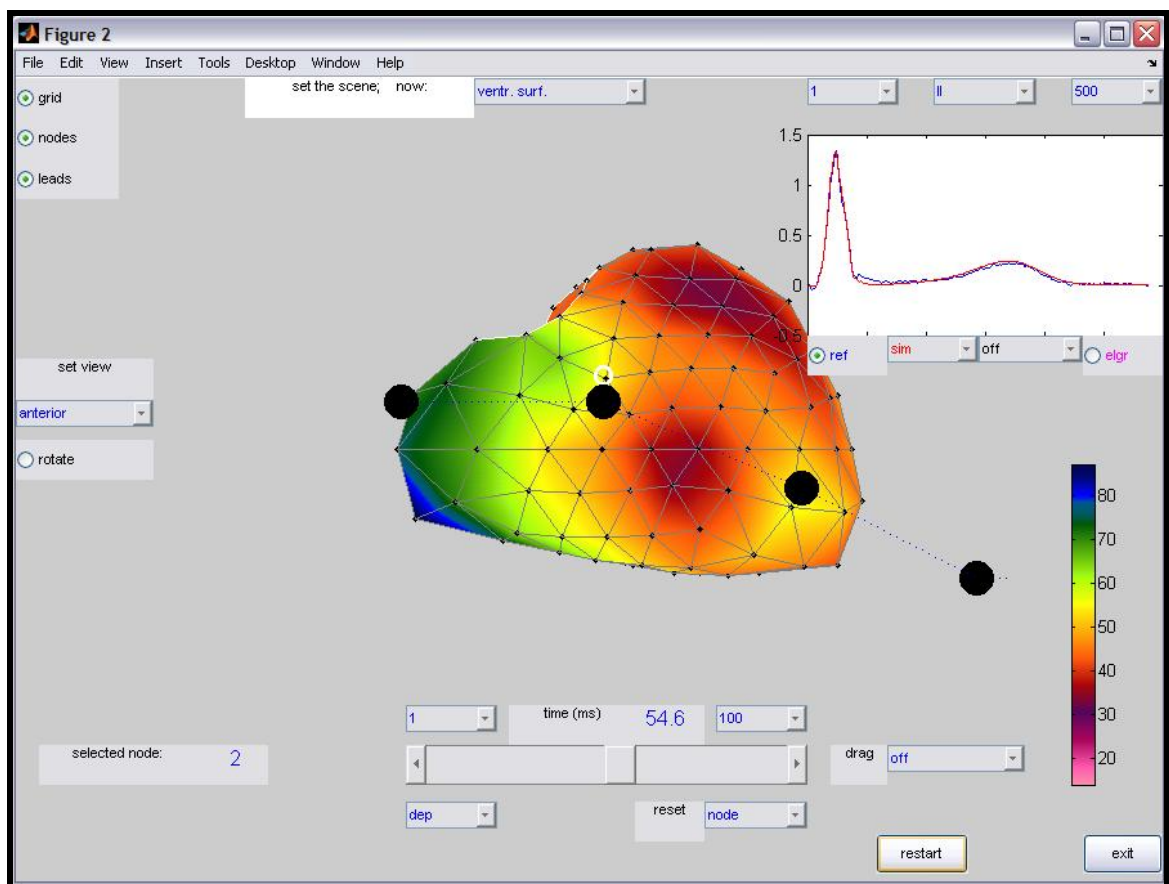


Figure 23 Display of the ECGSIM window.

3.2.3.1 The EDL source model

The source model used in the simulation is the equivalent double layer (EDL) [62]. All myocardial electric activity is represented by equivalent sources on a surface. The EDL model expresses the entire electrical activity within the ventricles by means of a double layer source situated on the closed surface bounding the ventricular myocardium—that is, epicardium, endocardium, and their connection at the base. This closed surface is represented by the symbol S_h .

For any position on S_h the time course of the local source strength is taken to be proportional to the transmembrane potential, $\varphi_m(t)$, of the cells near S_h . The maximum strength at any point is assumed to be the same (uniform double layer – UDL). This result is derived from an analysis of the electrical properties of ventricular cells by means of the bidomain approach. The main equation of the bidomain approach is [62]:

$$\varphi(y) = - \int_{S_h} g_i \cdot \varphi_m(x) \nabla Z \cdot dS_h \quad (64)$$

where $\varphi(y)$ is the potential at some observation point y outside the heart, g_i the conductivity of the intracellular aspect of the bidomain, $\varphi_m(x)$ the transmembrane potential at all points x throughout the heart and $Z = Z(y,x)$ is the lead field of the electrode configuration. Equation 65 involves integration over the surface S_h and x specifying the source location on S_h . Considering a hypothetical infinite homogenous medium surrounding the heart, the potential in this medium is [64]:

$$\varphi_\infty(y,t) = - \frac{g_i}{4\pi\sigma_o} \int_{S_h} \varphi_m(x,t) \nabla \frac{1}{R} \cdot dS_h$$

(65)

where σ_0 is the conductivity of the medium and R the distance between x and y .

In the ventricles, the measured wave front strength during depolarization in the fiber direction is approximately the same as that in the cross fiber direction. Hence the ratio of extra cellular to intracellular conductivity in the fiber direction can be taken to be the same in cross fiber direction. This point dominates the application of the equivalent surface model.

The surface S_h bounding ventricular mass is derived from MRI data. The surface is discretised into small triangles, i.e. N nodes ($N=257$), which serve as the locations of the equivalent double layer elements. The time course of the source strength of any node n is assigned a stylised version of the shape of the transmembrane potential of ventricular muscle cells, specified at 1 ms intervals [62]. The general shape of this curve was taken to be identical for all nodes. This shape was derived from a weighted mean of the measured ECG during the T wave.

The difference of the timing of local depolarization and local re-polarization for a particular node n is taken as a measure of the local action potential duration. The magnitudes of the upstroke of the local transmembrane potential are used to specify local source strength. These magnitudes scale the corresponding rows of the source matrix S . By reducing the magnitude of the source strength at node n the effect of, for example, local ischaemia on body surface potentials may be studied [62].

3.2.3.2 The Forward Transfer

The transfer between the elements of the EDL and the potentials on the thorax is dominated by the position and orientation of the heart inside the thorax, the position of the electrodes on the thorax, and the overall geometry of the thorax. The transfer between the elements of the EDL and the potentials on the thorax is computed by using the geometry of the torso and that of the relevant conductivity interfaces, measured by means of MRI. The model takes into account the relatively low conductivity of the lungs and the relatively high conductivity of blood in the ventricular cavities [62].

The potential at any point y within the thorax or on the body surface is defined by the equation:

$$\varphi(y, t) \propto - \int_{S_h} A(y, x) \varphi_m(x, t) d\omega(y, x) \quad (66)$$

where $A(y, x)$ considers the full complexity of the volume conductor including the geometry and conductivity and $d\omega$ is the solid angle subtended by the elementary surface element $dS_h(x)$ at y .

The elements of the computed transfer matrix A express the source strengths of all N ($N=257$) nodes on the heart as potentials at L ($L=198$) lead positions on the thorax surface. A subset of these elements is involved in the simulation of the standard 12 lead ECG [64].

3.2.3.3 Matrix formulation of the forward problem

The discretization of the EDL source model is carried out by specifying the time course of the electric source strengths of N elements of the EDL model at T subsequent time instants. This leads to a matrix representation of the source, the S matrix (dimension $N \times T$), having as its elements: $s_{n,t}$ $n=1 \dots N$; $t=1 \dots T$. In the same manner, the volume conduction effects are represented by a transfer matrix A (dimension $L \times N$), representing the potential in lead l ($l=1 \dots L$) generated by a source of unit strength at node n . By using both matrix formulations, the forward computation can be expressed simply by the matrix multiplication:

$$\Phi = A \cdot S \quad (67)$$

where Φ is a matrix (dimension $L \times T$) representing the potentials at L thorax locations (lead positions) at the T discrete time instants. The same formalism, involving a dedicated transfer matrix, can be used to compute the waveforms of the electrograms at the nodes of S_h based on the identical source matrix S .

3.2.3.4 Software Package

Starting from their default setting any of the source parameters may be varied at any of the nodes; the effect of this on heart and body surface potentials is visible instantaneously. While changing the value of a node parameter, the values at the surrounding nodes may be set to change by a factor that decreases with distance. The distance involved (corresponding to, for example, the extent of an ischaemic region) may be set interactively, and may be chosen to be effective either over the surface that carries

the node operated on, or throughout the myocardium. In this way epicardial, endocardial, or transmural changes may be induced. With this model, electrocardiographic signals on the thorax and also electrocardiograms on endocardium and epicardium can be computed.

In summary, this chapter discussed the results of experiments on animals to study the T wave elevation. Also three simulation models important to this research are discussed. Of the three models, the ECGSIM model is of particular interest to this research. The ECGSIM model is important for solving the T wave elevation problem as this model can be modified to study the ECG signals in a static magnetic field. The details of the modified ECGSIM model are discussed in the next chapter. Also in the next chapter a simulation package developed based on discretization of an aorta model and the use of magneto hydro dynamic equations is discussed. The model of the aorta developed, the various parameters considered and the step by step procedure of computing the induced T wave voltage are discussed in detail.

CHAPTER 4

METHOD TO COMPUTE AND SIMULATE THE INDUCED T WAVE POTENTIAL

This chapter discusses the method of computing and simulating the elevation of the T wave of the ECG signal in the MRI environment. The first section of this chapter discusses a basic simulation based on Lorentz equation which uses the ECGSIM package [62-64], discussed in the previous chapter. The ECGSIM package simulates the ECG signal on the thorax starting with the potential on the endocardium and epicardium. This package is modified to simulate the ECG signals in the presence of a static magnetic field. The first section of this chapter discusses this simulation.

As mentioned in the first chapter of this dissertation [1.4.1], the Lorentz equation does not consider many important parameters required to compute the magnetically induced potential. The Lorentz equation is derived considering a channel with rectangular cross-section and conducting walls. In the MRI, a voltage is induced due to the effect of the magnetic field on the blood flow in the aorta. The aorta wall has a circular cross-section and also the walls of the artery are non-conducting. The Lorentz equation does not consider parameters like the Hartmann number, the aortic blood pressure, and the density, conductivity and viscosity of blood. To make the simulation accurate it is essential to consider these important parameters and hence the second section of this chapter discusses a model to compute the T wave elevation based on magneto-hydro-dynamic equations. Each step involved in computing the potential including the magneto-hydro-

dynamic equations, the model of the aorta, the transfer matrix and the final computations are discussed in great detail.

The next section of this chapter discusses different methods to measure various parameters required to compute the potential as discussed in the previous section. The discussion considers the fact that the patient in the MRI is not easily accessible and the considerable amount of time required to obtain an MRI image [68, 69].

The final section of this chapter discusses the GUI simulation package developed in MATLAB. The package simulates the ECG signals on the thorax in the presence of a static magnetic field. The input parameters to this package are the magnetic field strength, the aorta diameter, the orientation of the aorta with respect to the heart and the ECG signal of the patient outside the MRI. Based on these input parameters the package computes the potential induced in the aorta due to the flow of blood in it in the presence of a static magnetic field. This potential is then transferred to the thorax and the package outputs the magnitude of the potential induced and the ECG signal with T wave elevation.

4.1 ECGSIM Model modified to study the elevated T waves of an ECG inside a static magnetic field based on Lorentz Equation

When a stationary, transverse magnetic field is applied to a moving electrically conducting fluid, electrical currents are induced in the fluid. The interaction between the

induced currents and the applied magnetic field produces a body force known as Lorentz force. As the heart muscle contracts periodically, blood is pumped from the left ventricle into the aorta through the aortic valve. The artery is considered to be round tubes of constant cross-section with non-conducting walls. Since blood is an electrical-conducting fluid, its flow in a uniform magnetic field produces a Lorentz force. The Lorentz force per unit volume due to the electrical conductivity of blood, arises in the direction of the flow and perpendicularly to the direction of the application of the magnetic field. In the analysis, the speed of blood flow in the radial and azimuthal directions is equal to zero and in the z direction depends only on the radius of the tube (see Figure 24). The applied magnetic field is homogenous and is directed perpendicular to the flow. Since for blood, the Reynold's magnetic number is much smaller than unity, the induced magnetic field is disregarded [53].

Since the maximum flow of blood from the heart is through the aortic valve into the aorta and this coincides with the occurrence of the T wave in the ECG, there is the superposition of the induced voltage on the T wave. In the MRI bore, the ascending aortic vessel is nearly orthogonal to the lines of magnetic induction and hence the magnitude of induced potential is determined by:

$$\psi = d \cdot V \cdot B \quad (68)$$

ψ is the induced voltage, d is the diameter of the artery, V is the velocity of blood flow and B is the external magnetic field applied. An average diameter of 32 mm is considered for the ascending aorta [24]. The external magnetic field applied (B) is a scalar and a

value of 1.5 T and 3.0 T is considered, as this is the magnetic field strength used in MRI scanners.

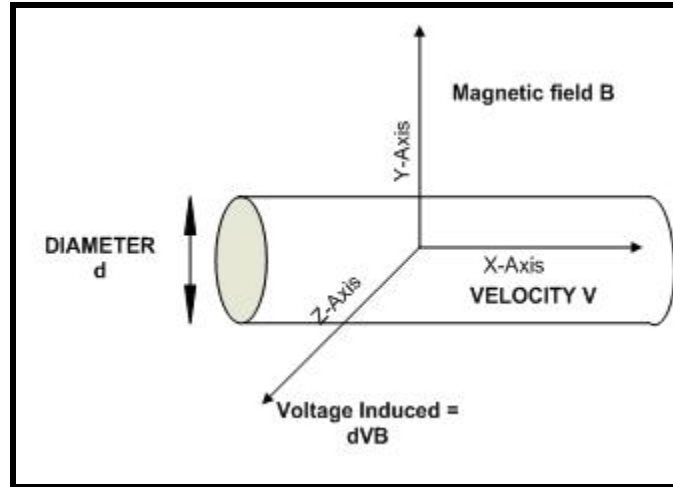


Figure 24 Mechanism responsible for induced potential.

The blood velocity profile is substituted in equation 68 to obtain the induced potential. This induced potential is then applied to the EDL source model of the heart at the nodes surrounding the aorta. The data for the blood velocity profile is obtained from the work by Joachim Lotz, et. al. in Medical School Hannover [11]. This profile is shown in figure 25.

This profile is then interpolated in MATLAB and substituted in equation 68 to obtain the induced potential. The magnetic field strength is considered a value of 1.5 T, the normalized flow in Figure 25 is multiplied by a factor of 350×10^{-6} (average peak value of blood flow in the human aorta is 350 ml/sec) [11] and the diameter of the aorta is substituted a value of 32 mm [24]. To notice a significant change in the ECG signals this

potential is multiplied by a factor of 10^3 . This potential is applied at the nodes surrounding the aorta in the equivalent double layer (EDL) model.

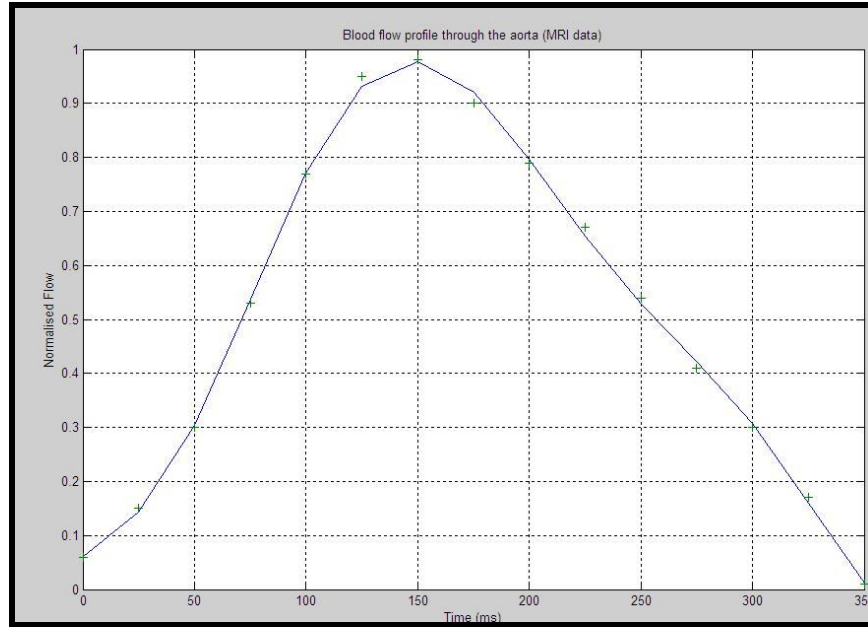


Figure 25 Blood flow profile in the aorta obtained from MRI.

As the potential is applied at the ascending aorta, there is a corresponding elevation in the T wave. The ECG tracing at the lead II in the presence of a magnetic field of 1.5 T and 3 T is shown in Figure 26 and Figure 27. The original T wave has amplitude of 0.22 mV and due to the magnetic field of 1.5 T and 3.0 T there is an increase in the T wave amplitude to 0.6 mV and 1.1 mV respectively. Hence there is an increase of 125 % and 400 % in the T wave amplitude for magnetic fields of 1.5 T and 3.0 T respectively.

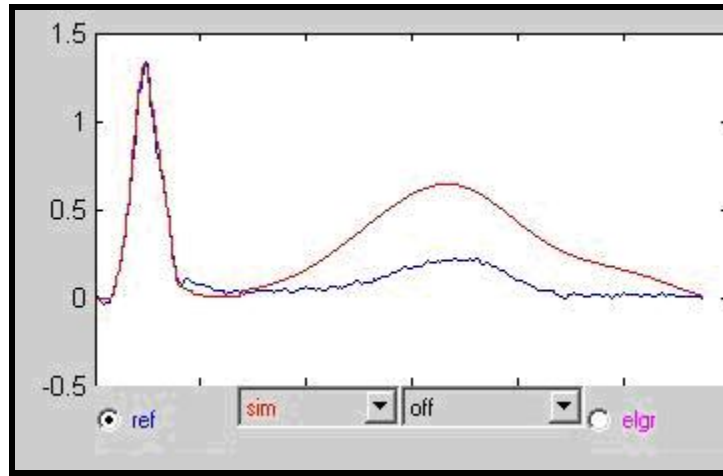


Figure 26 ECG tracing at lead II showing the elevated T wave for a field of 1.5 T.

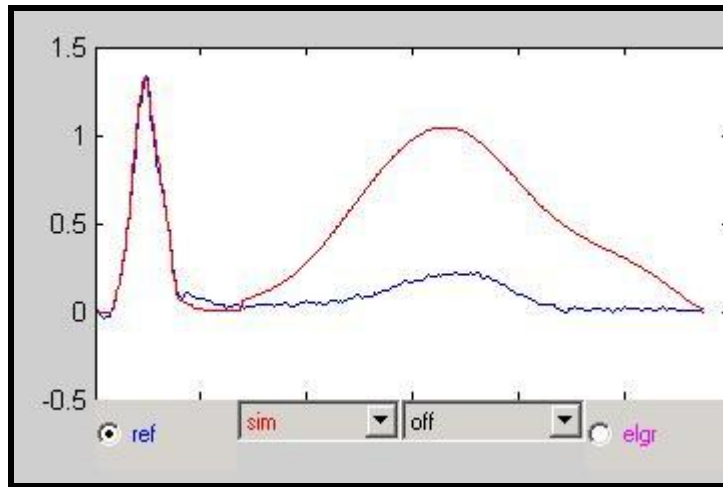
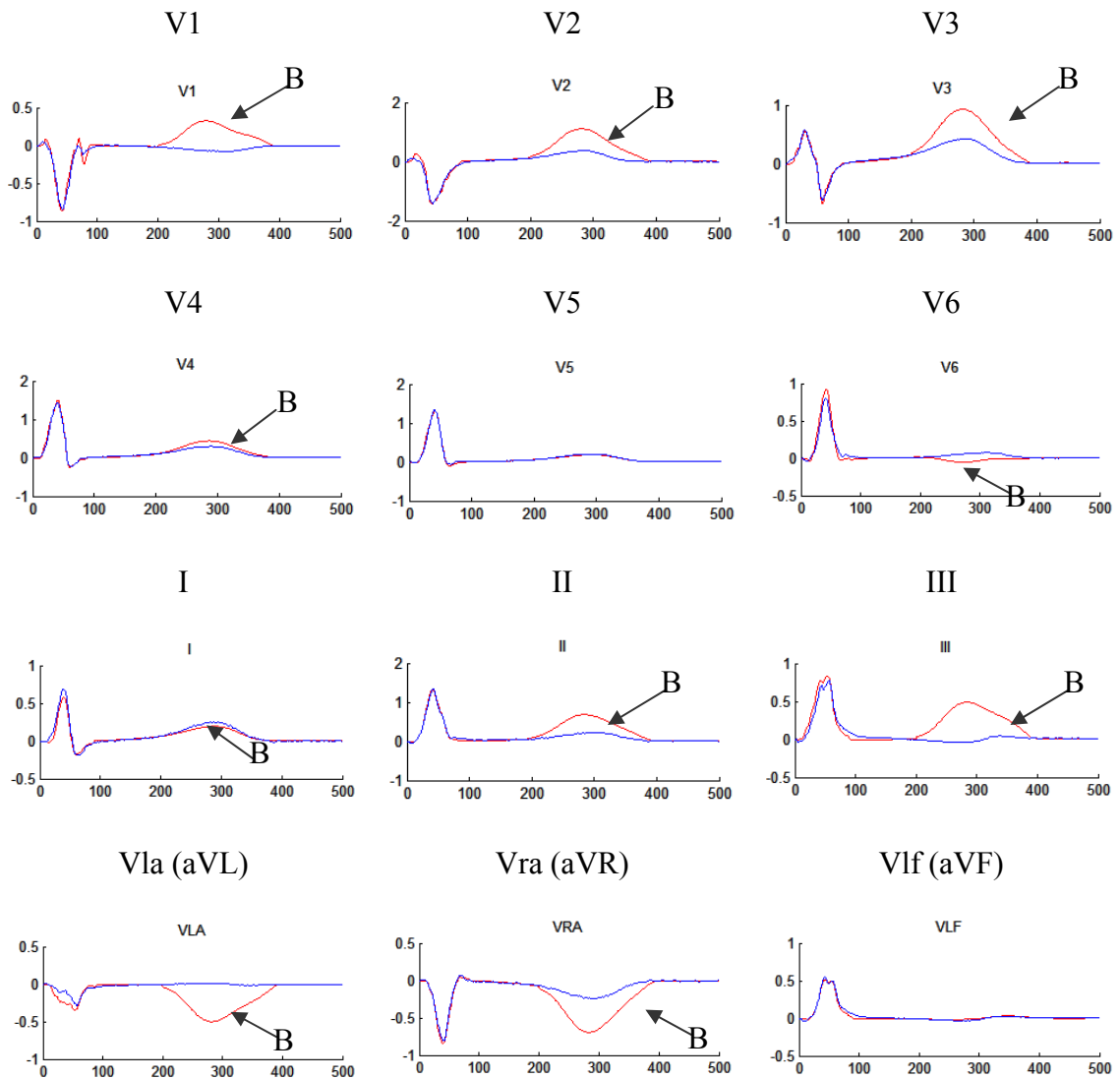


Figure 27 ECG tracing at lead II showing the elevated T wave for a field of 3.0 T.

Table 3 shows the ECG tracing at the 12 leads in the presence of a magnetic field of 1.5 T. A positive voltage is induced at leads V1, V2, V3, V4, II and III, a negative voltage is induced at leads V6, VLA and VRA and there is no significant voltage induced at leads V5, I and VLF. The results shown in table 3 are obtained only when the magnitude obtained using equation 68 (Lorentz equation) is multiplied by 10^3 . Consider the diameter of the aorta as 32 mm, the peak blood flow in the aorta as 350 ml/sec and a magnetic field

of 1.5 T. Substituting these values, the value of induced voltage is 16 microvolt. When this voltage is transferred to the thorax the magnitude will reduce further and hence this value is too small to make any difference in the ECG signals. Hence a factor 10^3 needs to be multiplied. This signifies that there are other significant terms essential to compute the induced potential not considered in the Lorentz equation.

Table 3 Simulation of 12 lead ECG in presence of 1.5 T magnetic field.



In spite of the small magnitude of potential obtained from the Lorentz equation, the simulation confirms that the blood flow in the aorta coincides with the instant of occurrence of the T wave. Also the temporal nature of this elevation and the field dependent increase of this elevation is confirmed.

This simulation is a basic model based on the simple Lorentz's equation. The potential computed from the Lorentz equation is applied at the nodes surrounding the aortic valve and not on a model of the aorta. This model is improvised by developing a 3D model of the aorta and using the magneto-hydro-dynamic equations and considering many important parameters. This model is discussed in the next section.

4.2 Model to compute the induced T wave potential

To understand the complete working of the GUI simulation model, the following subsections describe each aspect of the model in detail. First the magneto-hydro-dynamic (MHD) equations are derived, followed by the model of the aorta, the MHD equations applied on the aorta model, the transfer of the potential on the aorta to the thorax and finally the ECG waveforms simulated on the thorax. Figure 28 shows the entire system.

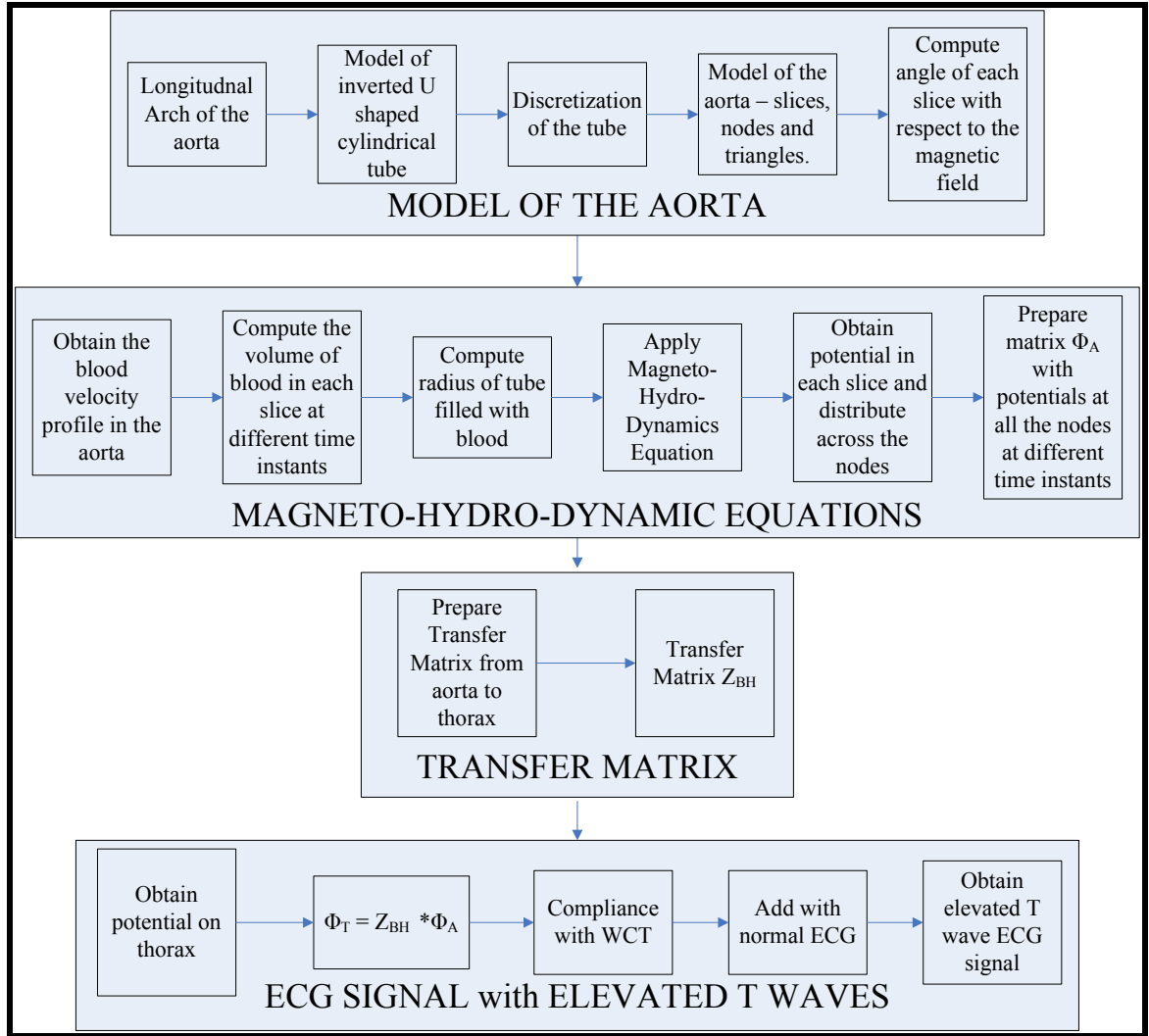


Figure 28 Block diagram of the entire model to compute the T wave elevated ECG signal.

4.2.1 The Magneto Hydro Dynamic Equations

The basic Lorentz equation, the Navier Stokes equation and the standard MHD equations are discussed in the first chapter of this dissertation. This section derives the MHD equations for a fully developed flow of a conducting fluid in a non-conducting round pipe subjected to a transverse magnetic field.

In a paper by Richard R Gold titled “Magneto-hydro-dynamic pipe flow” [19] the MHD equations are derived for the problem of flow of an incompressible, viscous, electrically conducting fluid through a circular pipe in the presence of an applied uniform magnetic field. The solution is exact and is thus valid for all values of Hartmann number. The induced voltage difference is derived as a function of magnetic field, radius of aorta, Hartmann number, aortic blood pressure, pulse wave velocity, the density, conductivity and viscosity of blood.

For the derivation, the flow of the electrically charged fluid is considered in the positive z direction and the magnetic field is in positive x direction (see Figure 24). The standard MHD equations considering an incompressible fluid and assuming no displacement currents are:

$$\rho(v \cdot \nabla)v - \mu_e(H \cdot \nabla)H = -\nabla(p + \frac{\mu_e H^2}{2}) + \mu \cdot \nabla^2 v \quad (69)$$

$$\mu_e \cdot \sigma \cdot \nabla \times (v \times H) + \nabla^2 H = 0 \quad (70)$$

$$\nabla \cdot v = 0 \quad (71)$$

$$\nabla \cdot H = 0 \quad (72)$$

ρ – fluid density; v – velocity; H – Magnetic field intensity; μ – fluid viscosity; μ_e – permeability; σ - conductivity; η – co-efficient of viscosity and p is the pressure. Consider the standard boundary conditions that the velocity and the induced magnetic field are zero at the wall. Then in cylindrical co-ordinates these boundary conditions are:

$$v_r = v_\theta = 0; v_z = v_z(r, \theta)$$

(73)

$$H_r = H_0 \cos \theta; H_\theta = -H_0 \sin \theta; H_z = H_z(r, \theta)$$

(74)

Considering equations 71 and 72, the boundary conditions and the fully developed flow assumption, only pressure will be a function of the direction of flow.

$$\frac{\partial p}{\partial z} = K_1$$

(75)

K_1 is a constant. To obtain the pressure variation, equation 69 is integrated with z . This leads to the equation:

$$p(r, \theta, z) = -\frac{\mu_e}{2} H_z^2 + K_1 z + K_2$$

(76)

Using equations 73-76 and expanding the dot and the cross products in equations 69-72, the following set of equations are obtained:

$$\mu \left(\frac{\partial^2 v_z}{\partial r^2} + \frac{1}{r} \frac{\partial v_z}{\partial r} + \frac{1}{r^2} \frac{\partial^2 v_z}{\partial \theta^2} \right) + \frac{\mu_e}{r} H_\theta \frac{\partial H_z}{\partial \theta} + \mu_e H_r \frac{\partial H_z}{\partial r} = K_1$$

(77)

$$\frac{\partial}{\partial r} \left(r \frac{\partial H_z}{\partial r} \right) + \frac{1}{r} \frac{\partial^2 H_z}{\partial \theta^2} + \sigma \cdot \mu_e \left(H_r \frac{\partial r \cdot v_z}{\partial r} + \frac{\partial v_e \cdot H_\theta}{\partial \theta} \right) = 0$$

(78)

$$v_z(a, \theta) = 0; H_z(a, \theta) = 0$$

(79)

Equations 77 and 78 can be non-dimensionalized by introducing the following terms:

$$v = \frac{v_z}{v_0}, H = \frac{H_z}{H_0}, \rho = \frac{r}{a}$$

(80)

where v_0 is some characteristic velocity, H_0 is the magnetic field and a is the pipe radius.

Using equation 80, equations 77 and 78 can be now written as:

$$\nabla^2 v - \frac{H_a^2}{R \cdot \sigma} \left(\left(\frac{\sin \theta}{\rho} \right) \frac{\partial H}{\partial \theta} - \cos \theta \frac{\partial H}{\partial \rho} \right) = K = \frac{K_1 a^2}{\mu \cdot v_0} \quad (81)$$

$$\nabla^2 H - R \cdot \sigma \left(\left(\frac{\sin \theta}{\rho} \right) \frac{\partial v}{\partial \theta} - \cos \theta \frac{\partial v}{\partial \rho} \right) = 0 \quad (82)$$

The solution to these equations and boundary conditions for the velocity is:

$$v = -\frac{K}{2\alpha} [X - Y] \quad (83)$$

$$X = \cosh(\alpha \rho \cos \theta) \sum_{n=0}^{\infty} \epsilon_n \frac{I'_{2n}(\alpha)}{I_{2n}(\alpha)} I_{2n}(\alpha \rho) \cos(2n\theta) \quad (84)$$

$$Y = \sinh(\alpha \rho \cos \theta) \sum_{n=0}^{\infty} 2 \frac{I'_{2n+1}(\alpha)}{I_{2n+1}(\alpha)} I_{2n+1}(\alpha \rho) \cos((2n+1)\theta) \quad (85)$$

where I_n is the modified Bessel functions of order n . The value of ϵ_n is 1 for $n=0$ and 2 for $n>0$. If two electrodes are placed on opposite sides of the pipe perpendicular to the magnetic field then the induced potential difference measured is a measure of the flow rate. The flow rate can be determined from equations 83-85 by determining the mean velocity. The induced voltage difference between θ equal to $\pi/2$ and $3\pi/2$ can be determined from the flow rate and is given by the equation:

$$V = 2 \cdot \mu_e \cdot H_0 \cdot v_0 \cdot a \cdot \frac{K}{2 \cdot \alpha} \int_{\rho=0}^1 \{X + Y\} d\rho$$

(86)

$$X = \frac{1}{\alpha\rho} \sum_{n=0}^{\infty} (-1)^n (2n+1) \frac{I'_{2n+1}(\alpha)}{I_{2n+1}(\alpha)} I_{2n+1}(\alpha\rho)$$

(87)

$$Y = \frac{1}{2} \sum_{n=0}^{\infty} (-1)^n \varepsilon_n \frac{I'_{2n}(\alpha)}{I_{2n}(\alpha)} I_{2n}(\alpha\rho) - \frac{1}{2\alpha}$$

(88)

Equation 86-88 is used in computing the induced potential in the aorta due to the static magnetic field. The next section discusses the model of the aorta and following this is the section on how these equations will be applied on the model to compute the voltage induced.

4.2.2 Model of the aorta

The aorta is the largest artery in the human body and carries oxygenated blood from the heart to different parts of the body [13]. The aorta originates from the left ventricle and is an elastic artery. When the left ventricle contracts and forces blood in the aorta, the aorta expands. The aorta contracts during the diastole period which is the relaxation phase of the heart. The potential energy acquired during expansion of the artery helps maintain pressure during diastole.

The aorta is divided into three sections – the ascending aorta, the arch of the aorta and the descending aorta [13]. The ascending aorta is the section from the left ventricle of the heart to the aortic arch. The aortic arch is the section that looks as an inverted U shape. The descending section is the part of the aorta from the aortic arch to the division of the

common iliac arteries. The arteries branching from the aortic arch are the brachiocephalic trunk, the left common carotid artery and the left subclavian artery [13]. The brachiocephalic artery further divides into the right subclavian artery and the right common carotid artery.

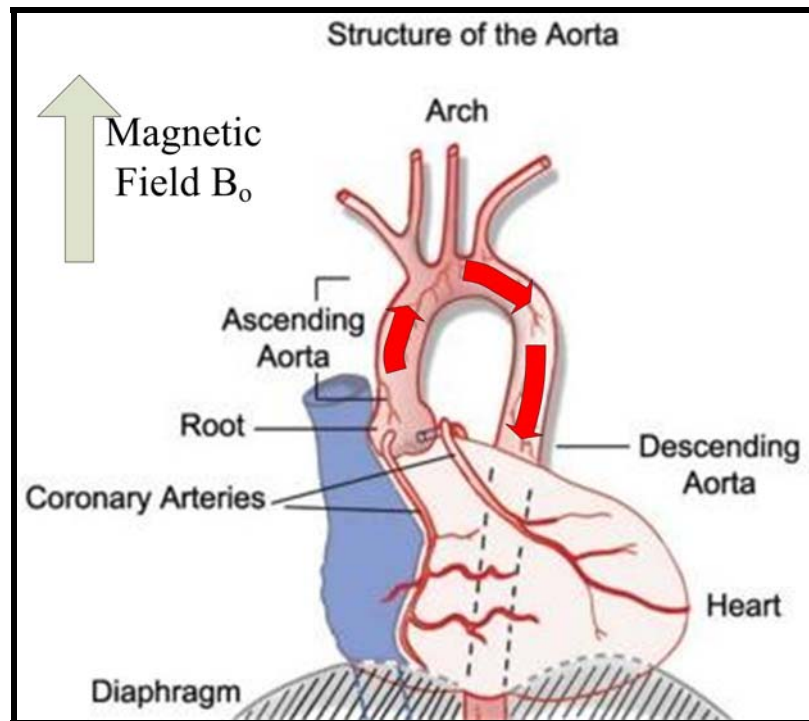


Figure 29 The structure of the aorta showing the three different sections.

The maximum potential induced due to the magnetic field will occur when the blood flows perpendicular to the magnetic field according to the Lorentz force. The blood flow in the aortic arch is perpendicular to the magnetic field and the blood flow in the ascending and the descending aorta is parallel to the magnetic field lines. Hence in the simulation, only the inverted U shaped aortic arch is modeled.

The aortic arch is developed using the mathematical equations developed by H. Fujiko, et. al.[70]. The model geometry is described by a set of formulas based on physiological data, obtained from computer tomography images. Although the model artery retains the curvature and torsion of the original, it has a constant, circular cross-section and no bifurcations. In the work of H. Fujiko, et. al. twenty co-planar images of the chest cavity were obtained from computer tomography [70]. From each image the wall of the aorta was detected and the aortic arch reconstructed. The longitudinal axis is obtained by taking a slice of data points through the volume of the reconstructed aortic arch. The data points obtained were updated by determining the centroid of each of the images to obtain true longitudinal axis of the aorta. The axis is defined in spherical coordinate system by the following equation (θ increases with the longitudinal distance along the aorta):

$$X_i = (R_a(\theta)\cos(\psi_a(\theta))\cos(\theta), R_a(\theta)\sin(\psi_a(\theta)), R_a(\theta)\cos(\psi_a(\theta))\sin(\theta)) \quad (89)$$

$$R_a(\theta) = A\theta^4 + B\theta^3 + C\theta^2 + D\theta + E \quad (90)$$

$$\psi_a(\theta) = -(\Psi_1 + (\Psi_2 - \Psi_1)\chi(\frac{\theta}{\Theta}))\cos(2\theta) \quad (91)$$

$$\chi(s) = 0(s < 0); 3s^2 - 2s^3 (0 \leq s \leq 1); 1(s > 1) \quad (92)$$

The coefficients in the above equations (89-92) were determined by least square fitting of the data obtained from computer tomography.

$$A = 5.01 \times 10^{-2}; B = -3.242 \times 10^{-1}; C = 5.948 \times 10^{-1}; D = -2.504 \times 10^{-1}; E = 2.759$$

$$\Psi_1 = 9.559 \times 10^{-2}; \Psi_2 = 1.598 \times 10^{-1}; \Theta = \frac{3}{4}\pi$$

(93)

Using the values in equation 93 the 3D co-ordinates of the longitudinal axis of the aorta are obtained. Figure 30 shows the longitudinal axis of the aorta.

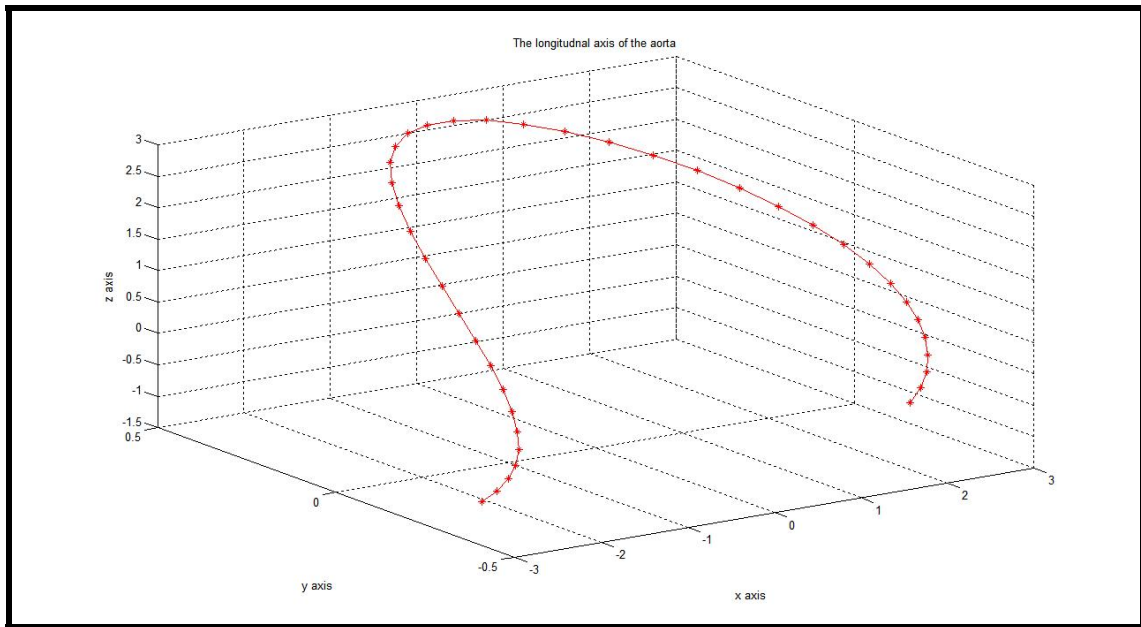


Figure 30 The longitudinal axis of the aorta.

Starting with the longitudinal axis of the aorta, a tube of constant radius is developed around the axis. The radius of the model aorta is taken to be 19 mm. Figure 31 shows the tube of constant radius developed around the axis. The tube is divided into a number of slices each having a constant width. A fixed number of points (nodes) uniformly spread on either edge of each of the slices are defined. These nodes form the vertices of the triangles and each of the slices is divided into a fixed number of triangles. The geometry is closed by considering a node on either side of the opening of the aorta. If the geometry is left open then the potential on the closing surfaces is zero and this may not be correct.

Hence it is essential for the geometry to be closed and the potential at the closures specified.

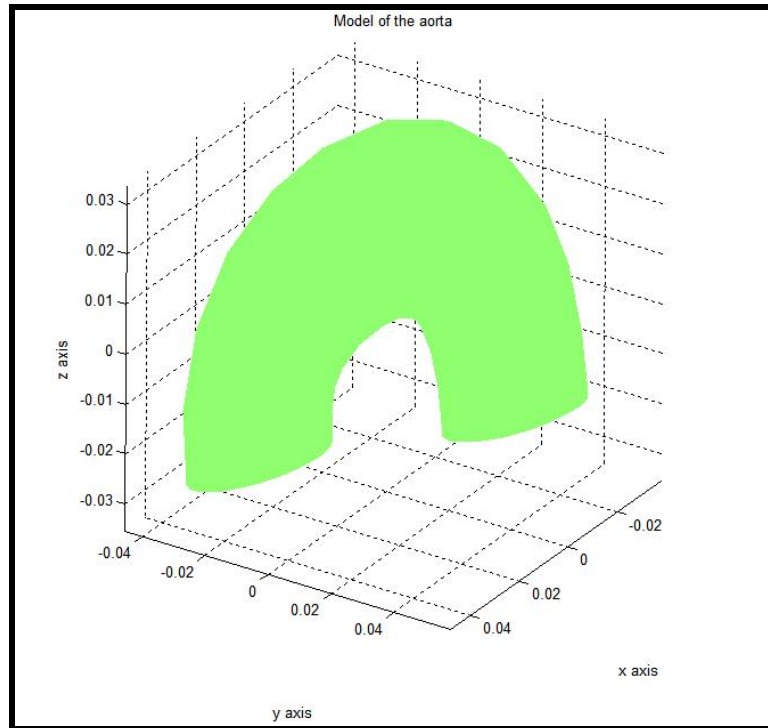


Figure 31 Tube of constant radius developed around the axis of figure 30.

The potential computed from the MHD equations for each of the slices is distributed across the slice in such a way that the maximum potential for each slice occurs in the direction perpendicular to the flow and perpendicular to the magnetic field according to the right hand rule. The potential decreases on either side and is minimum on the triangle on the opposite side of the maximum potential triangle. The potential at the two closure nodes are considered to be the mean value of the nodes surrounding it.

In the model developed there are 12 slices on the model of the aorta. Each slice has 40 triangles and there are 20 triangles on each of the closing surfaces (total triangles – $12 \times 40 + 20 \times 2 = 520$ triangles). The 12 slices have 13 edges and each edge has 20 nodes and there are two nodes on the closing surface ($13 \times 20 + 2 = 262$ nodes). Figure 32 shows the model of the aorta with the triangles and the nodes.

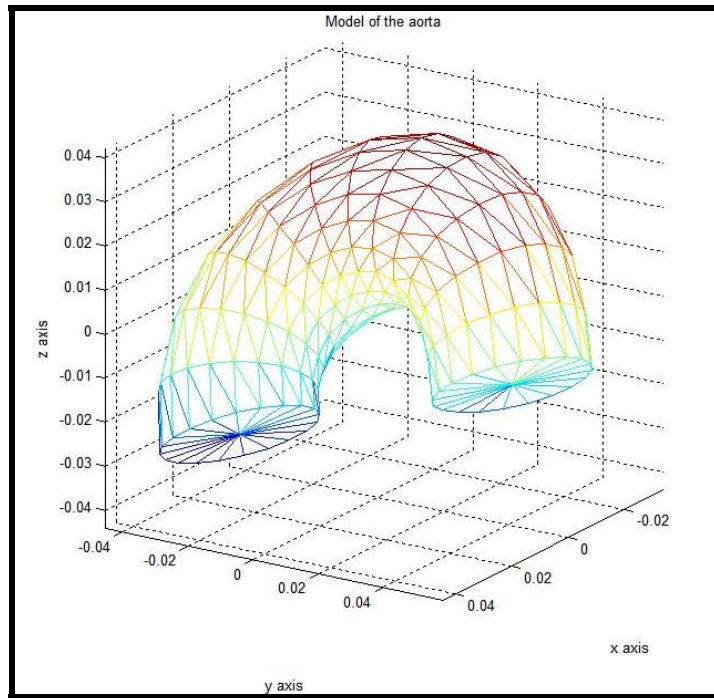


Figure 32 Model of the aorta showing the nodes and triangles.

4.2.3 Computing the potential induced for each of the slices of the aorta

The magneto hydro dynamic equations (equations 86-88) are applied to the flow of blood in each of the slices. The angle (θ) of each slice of the aortic arch with respect to the magnetic field B is determined geometrically. The corresponding component of $B \bullet \cos \theta$

is used for each slice in the MFD equation. The angle of each slice with respect to the magnetic field is shown in Figure 33. In the MRI bore, the uniform magnetic field passes through the length of the body of the patient. The slices 5 and 6 (see Figure 33) perpendicular to the field will have the maximum induced voltage. As the angle between the magnetic field and the slice decreases from 90° to 0° , the magnitude of the voltage induced decreases proportionately. Slices 11 to 13 have a negative angle because the orientation of the aorta is not parallel to the magnetic field.

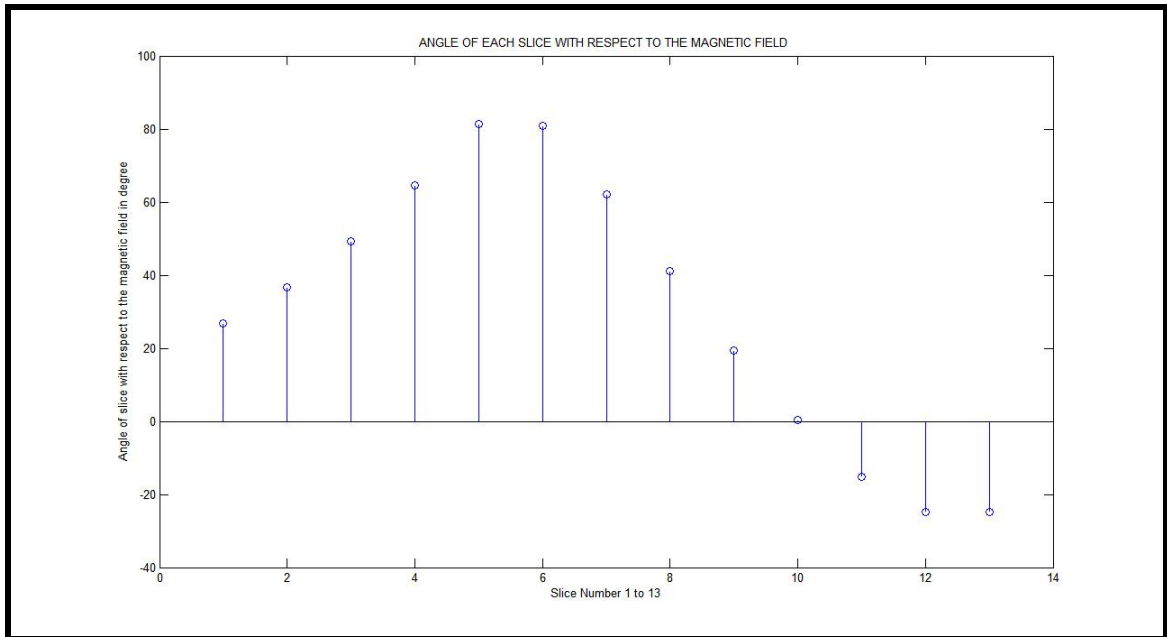


Figure 33 Angle of each slice with respect to the magnetic field.

The induced voltage is computed for each of the slices using the MFD equation (equation 3). First the blood velocity profile of the flow of blood in the aorta is obtained. This is required to obtain the volume of blood in each slice. The pulse wave velocity (PWV) is the velocity with which the blood velocity profile travels through the aorta. Based on the

pulse wave velocity, the time taken for velocity profile pulse to travel from one slice to another ‘ δt ’ is computed by the following simple equation.

$$\delta t = \frac{\delta w}{PWV} \quad (94)$$

‘ δw ’ is the width of each slice. The blood velocity profile is discretized into ‘ δt ’ time instants. During the first ‘ δt ’ instant, there will be some blood in the first slice. During the second ‘ δt ’ instant, there will be blood in the first and second slices and so on. At each of the ‘ δt ’ time instants, the volume of blood in each of the slices is measured by integrating the velocity profile curve within the limits of the particular ‘ δt ’ time instant. Using the volume of blood in each slice, the radius of a cylinder completely filled with that particular volume of blood is determined using the volume equation for a circular cylinder. This is required as the MHD equations are derived for a fully developed flow. Using this radius value and the component of B ($B \cdot \cos \theta$) for a particular slice, equations 19-21 are applied to determine the induced voltage across it at any particular time instant.

After computing the potential induced in each slice this potential needs to be distributed to the various nodes in each slice. To analyze the distribution of potential on the aorta surface for each slice Maxwell 2D software is used. The MHD equation computes the potential measured by two electrodes on either side of the cylinder carrying the charged fluid. The same situation is simulated in Maxwell 2D and the distribution of potential is studied. Figure 34 shows the distribution of potential around the aorta (dark red – maximum positive potential and dark blue – minimum potential). The center cylinder

represents the aorta and the two cylinders on either side are the two electrodes measuring the potential.

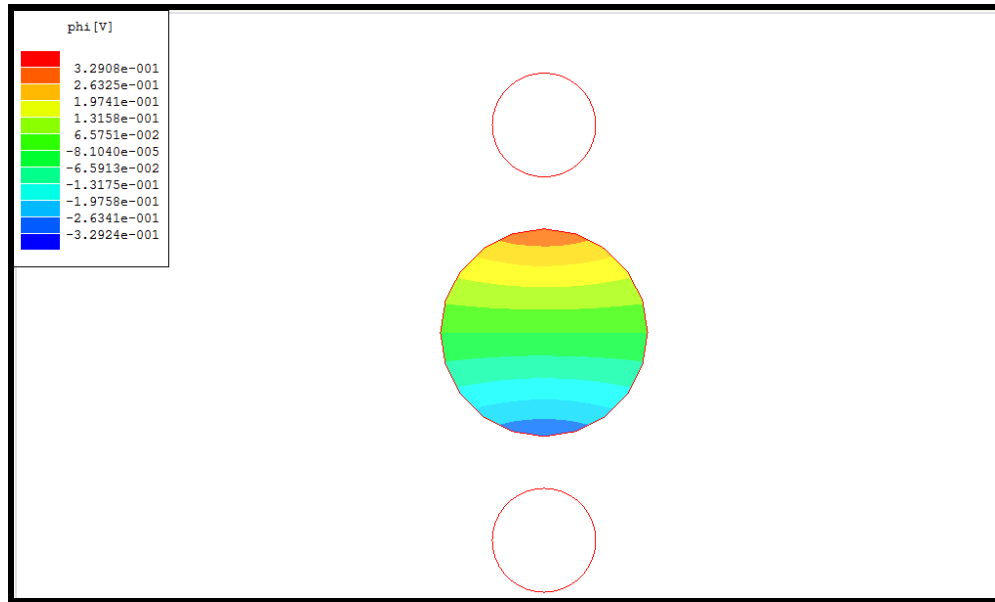


Figure 34 The potential distribution on the aorta surface determined from Maxwell 2D.

As an example, a potential of 1 V is assigned to the top electrode and a value of -1 V is assigned to the lower electrode. The potential around the aorta varies from -0.3 V to 0.3 V as shown in the figure. A similar variation of potential is assigned to the various nodes in each slice. Also as described earlier, the maximum potential for each slice is assigned to the node which is perpendicular to the flow and perpendicular to the magnetic field according to the right hand rule. The potential decreases on both sides and the minimum potential is assigned to the node on the opposite side of the maximum potential node. The potential at the two closure nodes are considered to be the mean value of the nodes surrounding it.

A matrix Φ_A of voltages induced in all the nodes of the aorta at different time instants is formulated. The voltage induced in each node is then transferred to the thorax by computing a transfer matrix based on the geometry, position and shape of the aorta and thorax. The details involved in computing this transfer matrix is presented in the next section.

4.2.4 Transfer Matrix

This section discusses the transfer matrix to relate the induced voltage on the aorta to the body surface potential distributions on the thorax. Each of the slices is triangulated uniformly to have N number of triangles on the entire aorta surface, as discussed earlier. The potential induced in each slice is computed using the MFD equation and a linearly varying potential is assigned to the nodes on each slice as discussed earlier. The next step is to transfer this potential to all the nodes on the thorax.

The induced voltage on the nodes of a closed surface can be transferred to a set of nodes on a different closed surface using the algorithm described in a paper by Roger C Barr, et. al.[71, 78]. The paper provides a method for finding transfer coefficients that relate the epicardial and body surface potential distributions to each other. The method is based on knowing the geometric location of each electrode, on having enough electrodes to establish the geometric shape and the potential distribution of closed epicardial and body surfaces. The method does not require any electrical quantities, such as voltage gradients,

be known in addition to the potentials. The method also does not require the heart or body surface to have any special shape, such as that of a sphere.

Two closed surfaces are defined - the outer surface S_B (representing the body) and the inner surface S_A (representing the aorta). The potential at any observation point in the volume V between the two surfaces in terms of the potential on S_B and the potential and gradient on S_A is defined by the equation:

$$\phi = -\frac{1}{4\pi} \int_{S_A} \phi_A \frac{\bar{r} \cdot \bar{n}}{r^2} dS_A - \frac{1}{4\pi} \int_{S_A} \frac{\nabla \phi_A \cdot \bar{n}}{r} dS_A + \frac{1}{4\pi} \int_{S_B} \phi_B \frac{\bar{r} \cdot \bar{n}}{r^2} dS_B \quad (95)$$

where r is the distance from an observation point to the surface, \bar{r} is the unit vector in the direction of r and \bar{n} is an outward pointing vector normal to the surface. ϕ_A and ϕ_B are the potentials on the aorta and the body. Any number of equations can be generated in the form of Equation 95 by placing the observer at different locations within the volume V . Figure 35 shows the volume V with the inner and outer surfaces, the normal vector and the observer [71]. The next step is to convert these set of equations in to a set of simultaneous linear equations.

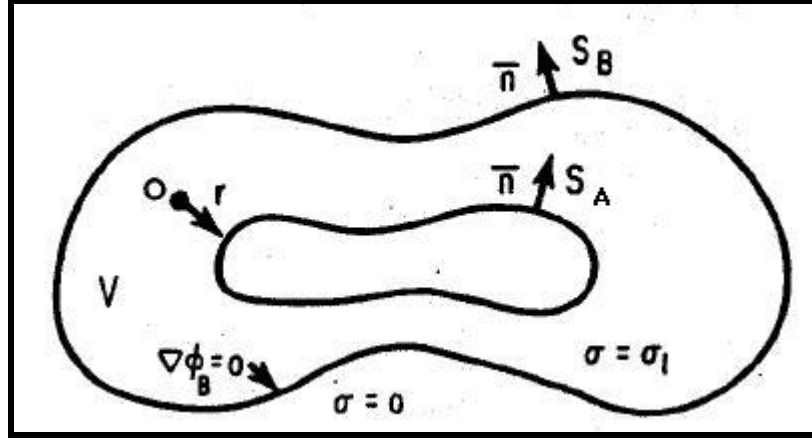


Figure 35 Volume V showing the inner and outer surfaces and the observation point o.

Consider a set of N_A locations on the surface of the aorta S_A and N_B locations on the body surface S_B . Two specific forms of equation 85 can be obtained by placing the observer at any node, where the potential needs to be determined, on the inner and the outer surface. Discretization of the specific equation for the observer on the body surface defines the following set of equations:

$$-\phi_B^i + \frac{1}{4\pi} \int_{S_B} \phi_B \cdot d\Omega_{BB}^i = \sum_{j=1}^{N_B} p_{BB}^{ij} \Phi_B^j \quad (96)$$

$$-\frac{1}{4\pi} \int_{S_A} \phi_A \cdot d\Omega_{BA}^i = \sum_{j=1}^{N_A} p_{BA}^{ij} \Phi_A^j \quad (97)$$

$$-\frac{1}{4\pi} \int_{S_A} \frac{\nabla \phi_A \cdot \bar{n}}{r^i} \cdot dS_A = \sum_{j=1}^{N_A} g_{BA}^{ij} \Gamma_A^j \quad (98)$$

Discretization of the specific equation for the observer on the aorta surface defines the following set of equations:

$$\frac{1}{4\pi} \int_{S_B} \phi_B \cdot d\Omega_{AB}^i = \sum_{j=1}^{N_B} p_{AB}^{ij} \Phi_B^j \quad (99)$$

$$-\phi_A^i - \frac{1}{4\pi} \int_{S_A} \phi_A \cdot d\Omega_{AA}^i = \sum_{j=1}^{N_A} p_{AA}^{ij} \Phi_A^j \quad (100)$$

$$-\frac{1}{4\pi} \int_{S_A} \frac{\nabla \phi_A \cdot \bar{n}}{r^i} \cdot dS_A = \sum_{j=1}^{N_A} g_{AA}^{ij} \Gamma_A^j \quad (101)$$

Φ_B and Φ_A are matrices containing the potentials at the N_B and the N_A locations on surfaces S_B and S_A respectively. Γ_A contains the normal components of the gradients on S_A . In the equations 96-101, the first superscript and the first subscript of the p's and g's coefficients identifies the location and surface where the observer is stationed. The second superscript and the second subscript of the p's and g's coefficients identifies an element of the corresponding surface of integration.

By choosing the location of the observer successively at all N_B locations and then at all N_A locations, two sets of equations are obtained:

$$P_{BB} \Phi_B + P_{BA} \Phi_A + G_{BA} \Gamma_A = 0 \quad (102)$$

$$P_{AB} \Phi_B + P_{AA} \Phi_A + G_{AA} \Gamma_A = 0 \quad (103)$$

The P's in the above equations are coefficients of potential Φ_B and Φ_A . The G's are coefficients of the normal components of gradients Γ_A . The different rows of matrices P_{BB} , P_{BA} and G_{BA} correspond to different locations of the observer on the body surface

(first subscript) and hence have N_B rows. P_{AB} , P_{AA} and G_{AA} correspond to the observer being at different locations on the aorta and hence have N_A rows. The number of columns can be deduced from the second subscript and hence can be N_B or N_A .

Eliminating the term Γ_A from the equations 102-103 and separating the coefficients of Φ_B and Φ_A , the following equation is obtained:

$$(P_{BB} - G_{BA} G_{AA}^{-1} P_{AB}) \Phi_B = (G_{BA} G_{AA}^{-1} P_{AA} - P_{BA}) \Phi_A \quad (104)$$

This equation relates the potential at the N_B locations on the body surface with the potential at the N_A locations on the aorta. Hence the transfer matrix Z_{BA} can be defined as:

$$Z_{BA} = (P_{BB} - G_{BA} G_{AA}^{-1} P_{AB})^{-1} (G_{BA} G_{AA}^{-1} P_{AA} - P_{BA}) \quad (105)$$

Each of the P's and G's in the above equation (equation 105) is a matrix of coefficients depending entirely on the geometry. The surface integrals to obtain the P's and G's matrices is divided into the close and distant surfaces. The close surface covers the area covered by the triangles that have an apex at the observer's location. For the matrices P_{AB} , P_{BA} , G_{BA} and G_{AB} the close surface integral is zero. The integral over the distant surface is further subdivided as a collection of integrals over each triangle in the distant region. After computing the six matrices, these matrices are substituted in Equation 105 to obtain the transfer matrix Z_{BA} . Hence, the potential at the nodes on the thorax is obtained by substituting the transfer matrix Z_{BA} and the potentials on the aorta Φ_A in the following equation:

$$\Phi_B = Z_{BA} \cdot \Phi_A \quad (106)$$

The potential obtained at the N_B electrodes on the thorax is the potential induced due to the flow of blood in the aorta subjected to a uniform magnetic field. The induced potential at the standard 12 leads can be derived as a subset of the N_B electrodes on the thorax. In the next section, how this potential obtained on the thorax is incorporated in the normal ECG signal is discussed.

4.2.5 Final Computations

In this section, first the significance of the Wilson's Central Terminal (WCT) [72] is discussed and then the potential obtained on the thorax is incorporated in the waveform of a normal ECG signal.

For a volume conductor, the reference of the ECG potential cannot be considered as infinite. The reference of the potential field on the thorax remains undetermined. Hence, the potential on the thorax is made specific by choosing a central terminal. This terminal is called Wilson's Central Terminal (WCT) [72]. This is computed by determining the mean of the potentials VRA, VLA and VLF, as these three terminals are the extreme leads on the thorax. This reference potential is then subtracted from all the electrodes including VRA, VLA and VLF.

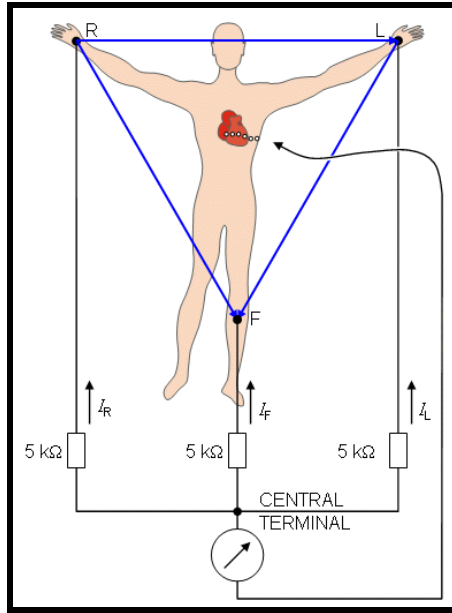


Figure 36 Wilson Central Terminal (WCT) – average of limb potentials.

After computing the induced potential Φ_B at the N_B nodes on the thorax, the potential at the standard 12 leads is derived from the Φ_B matrix. From the potential at the 12 leads, the mean of the potentials VRA, VLA and VLF is obtained and subtracted from the potentials at all the 12 leads including VRA, VLA and VLF. This new potential values obtained complies with WCT. This potential is now added to a normal ECG waveform (from the ECGSIM package) to obtain the ECG waveforms in the presence of the magnetic field. The results obtained are discussed in chapter 6.

4.3 Parameters required to compute the induced potential

This section discusses the various input parameters required to compute the induced potential and the feasible method to measure them. The main input parameters are the

magnetic field strength, the blood density, viscosity and conductivity, the differential pressure component ($\delta p/\delta z$), the pulse wave velocity, the aorta radius and the blood velocity profile in the aorta.

The magnetic field strength can be directly known from the MRI system used. The normal MRI machines use a static magnetic field of 1.5 T to 3 T. The blood density, viscosity and conductivity can be assumed a constant value for all the computations. In this simulation, the blood density, viscosity and conductivity have been considered a value of 1.055 g/cm³ (value in human varies from 1.05 to 1.06), 0.04 N.sec/m² and 0.667 respectively [19].

The pulse wave velocity (PWV) can be determined from the ECG and the pulse oximeter waveform – the photo-plethysmogram (PPG) [39, 40, 43, 44]. The PPG is an indication of the blood volume profile at the peripheral site, where the pulse oximeter is placed. The pulse wave velocity is defined as the velocity with which the blood velocity pulse travels from the aortic valve to any peripheral location. The pulse transit time (PTT) is the time interval for the arterial pulse wave to travel from the aortic valve to the peripheral site [43]. The time interval between the ECG R wave and the peak of the peripheral pulse is usually selected as the PTT. The inverse of the pulse transit time gives the pulse wave velocity.

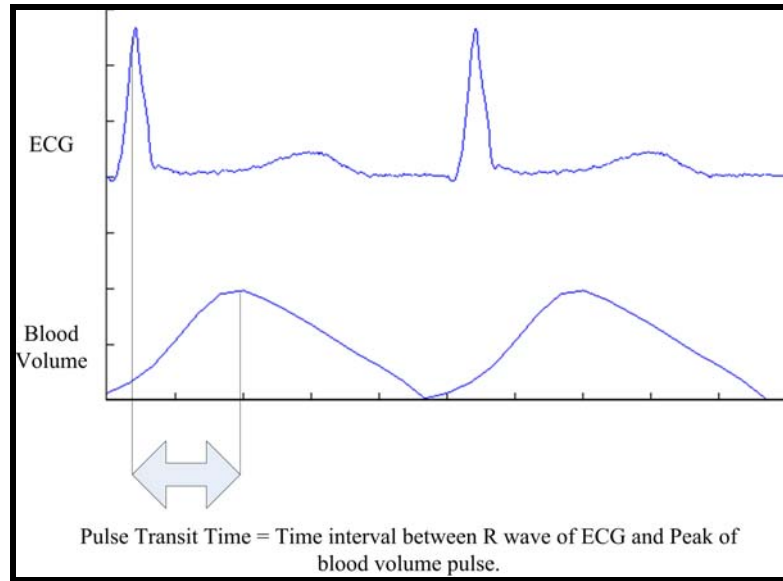


Figure 37 Pulse transit time (PTT) calculation.

The next input parameter required is the differential pressure component. This component is related to the difference between pressure in the ascending aorta and the pressure in the thoracic aorta (or a peripheral site), which is responsible for the flow of blood in the aorta. The pressure drop in the aorta is considered a constant value of 40 mm Hg.

The other important input parameter is the blood velocity profile in the aorta, as this parameter is directly related to the cardiac output. This profile is used in the model to obtain the blood volume in each slice of the aorta, as discussed in the previous section. In a research model developed by Nicolaas Westerhof, et. al. [73], an electrical network is derived to represent each arterial segment in the entire human arterial system. Using the Navier-Stokes equations, the continuity equation for the motion of fluid, the equation of motion of the vessel wall and Hooke's law for elastic material, mathematical expressions for the longitudinal and transverse impedance of a segment of artery is obtained. The

Navier-Stokes equations are linearized. Each artery is assumed as a cylinder with circular cross-section. The flow in the artery is considered to be laminar and rotationally symmetric. The relative variations in radius resulting due to the transmission of the pressure wave are small relative to the radius itself. Also the peculiarities in flow at the branching arteries are ignored.

The longitudinal and transverse impedances for a segment of artery can be represented as passive electrical networks as the vessel wall is assumed to be purely elastic. The resistors, inductors and capacitors in the electrical network represent viscous and inertial properties of blood and compliant properties of the arteries and are defined by the equations below [73]:

$$R'_n = \frac{8\pi\eta}{(\pi \cdot r^2)^2} n \quad (107)$$

$$L'_n = \frac{\rho}{\pi \cdot r^2} \frac{1}{2n-1} \quad (108)$$

$$C' = \frac{3 \cdot \pi \cdot r^2 \left(\frac{r}{h} + 1\right)^2}{E \cdot \left(2\frac{r}{h} + 1\right)} \quad (109)$$

where r is the radius, h is the wall thickness, E is the Young's modulus of the vessel wall, ρ is the density of blood and η is the viscosity of blood. In the above equations 107-109, the value of n varies from 1 to at least 3 and at most 5 depending on the radius. Figure 38 shows the electrical representation of a segment of artery of unit length.

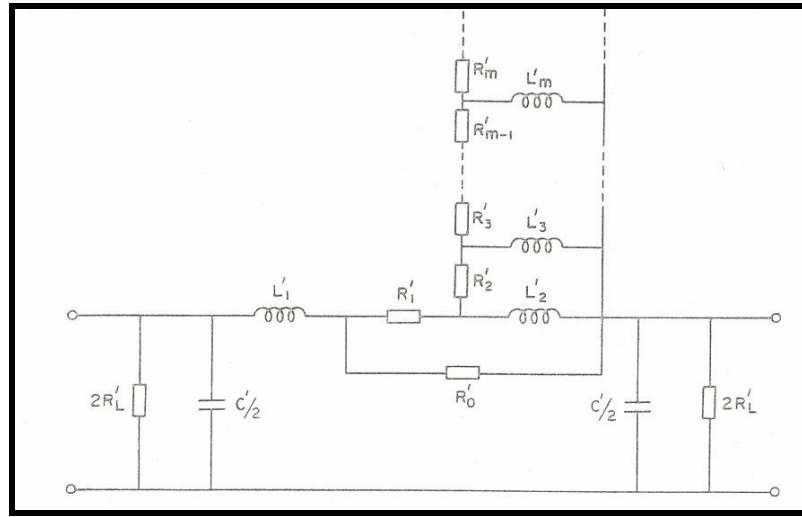


Figure 38 Electrical representation of a segment of artery of unit length

If the arteries are divided into segments, each segment can be replaced by this network by multiplying the resistors, capacitors and inductors by the length of the segment. The entire arterial tree can be sub-divided into a large number of segments. Each segment can be represented as an electrical network as shown in Figure 38 if the radius, segment length, density and viscosity of blood, wall elasticity (Young's modulus) and wall thickness are known. The source of the entire electrical network can be a pressure pattern (voltage source) or any ejection flow (current source).

This entire network starting from the aorta to the finger is modeled in MATLAB. The arteries modeled include: aorta ascendens (two segments), arcus aorta (one segment), subclavia (two segments), axillaris (two segments), brachialis (four segments), ulnaris (four segments) and finally radialis indicis artery (artery in the finger).

A normal pressure waveform is used as the source of the network to verify the accuracy of the model. As the radius of the arteries decrease, the resistance to flow of blood increases and hence the pressure increases. In accordance with this fact, an increase in pressure of 15 mm Hg is obtained from the model. Figure 39 shows the change in pressure from the aorta to the finger. This is compared to measured data from a research experiment by Mustafa, et. al.[46]. In this experiment, the systolic and diastolic pressure is measured in the aorta and the finger in 12 different patients of different ages. The mean increase in pressure from the aorta to the finger is 23 mm Hg. Hence the model in MATLAB is accurate and can be incorporated in the model to measure T wave elevation in ECG in the presence of a static magnetic field.

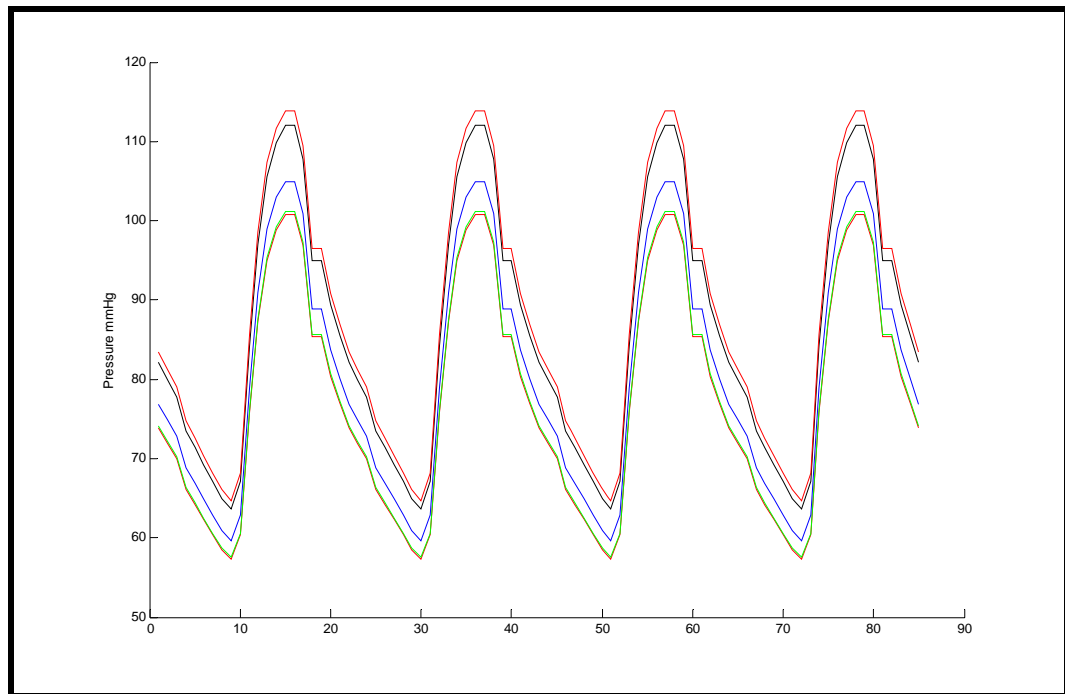


Figure 39 The pressure waveforms at the aorta (minimum amplitude), the finger (maximum amplitude) and some intermediate arteries.

The photo-plethysmogram waveform obtained from the pulse oximeter is a representation of blood flow in the finger. This waveform is used as the source in the above model and the blood flow waveform in the aorta can be obtained. Figure 40 shows the change in blood flow from the finger to the aorta. The blood flow in the finger is used as the source to the electrical model. This is the waveform with the minimum amplitude in Figure 38. The blood flow waveform in the aorta obtained from this model is used to determine the volume of blood in each of the slices in the model of the aorta. From this volume the radius of each slice completely filled with blood is computed. This value is used in the magneto-hydro-dynamic equations to calculate the potential.

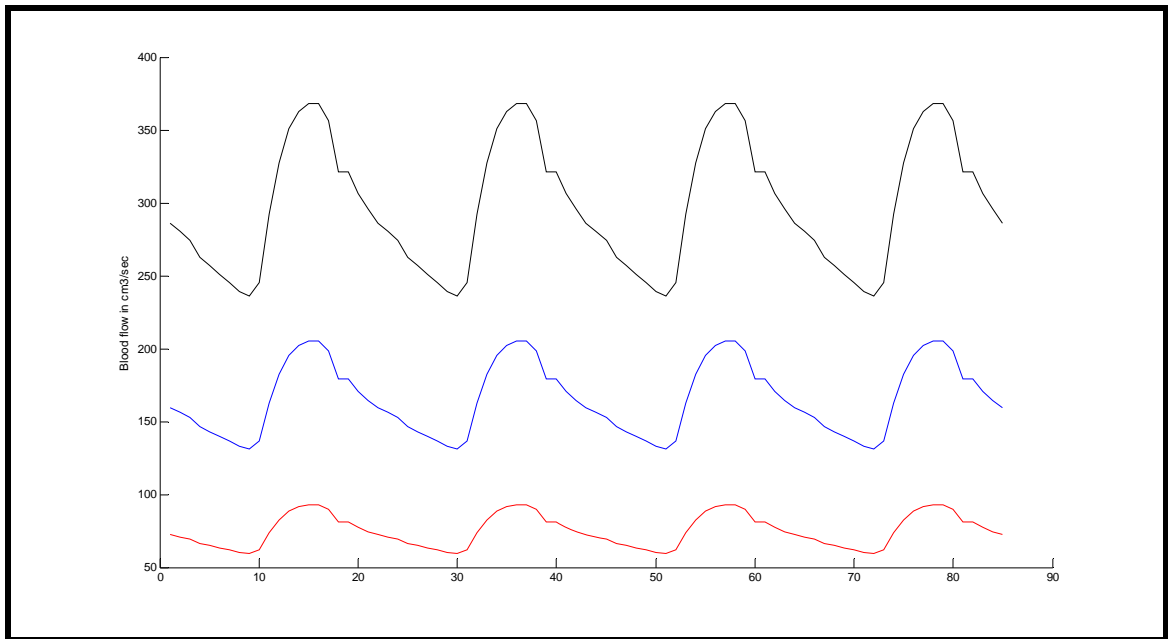


Figure 40 Blood flow in the aorta (maximum amplitude), brachialis and the finger (minimum amplitude).

4.4 GUI Simulation Package

The GUI simulation package developed in MATLAB simulates the ECG signals on the thorax in the presence of a static magnetic field. This ECGSIM package [62-64] discussed in the previous chapter (section 3.3) is used as the reference to develop this model. This package is based on the model to compute T wave elevation presented earlier in this chapter. The input parameters to this package are the magnetic field strength, the aorta diameter, the photo-plethysmogram (PPG) obtained from pulse oximeter, the orientation of the aorta with respect to the heart and the ECG signal of the patient outside the MRI. Based on these input parameters the package computes the potential induced in the aorta due to the flow of blood in it in the presence of a static magnetic field. This potential is then transferred to the thorax and the package outputs the magnitude of the induced potential and the ECG signal with T wave elevation.

The interactive package allows the user to change the magnetic field strength, the aorta diameter, the differential pressure component and the orientation of the aorta with respect to the heart. As these parameters may not be directly known before the patient is taken in the MR room, a set of default values are assigned to them. The magnetic field strength has a default value of 1.5 T, the aorta radius has a default value of 1.6 cm and the differential pressure component has a value of 40 mmHg. Also the orientation of the aorta with respect to the heart may be changed by specifying the angle of rotation along two orthogonal axes. Two data files are required by the simulation package – the ECG of the patient in the MRI and the waveform from the pulse oximeter - the

photoplethysmogram (PPG) waveform. This completes all the information needed by the package to determine the T wave elevation.

The package outputs the magnitude of the T wave elevation and the artifact free ECG signal at the 12 leads of the ECG. Also the package gives the user the option to select different nodes on the aorta and observe the voltage induced at the particular nodes. The final output screen shows the PPG, the blood volume in the aorta, the ECG of the patient in the MR room and the artifact free ECG signal. Also the package displays the patients heart rate determined from the ECG and the pulse wave velocity determined from the PPG and the ECG of the patient.

After all the input parameters have been entered and the “Start Computation” button clicked, a series of computations start. These computations include all the steps discussed in the model in the second section of this chapter. If the user changes the orientation of the aorta with respect to the heart then based on the radius and the new position of the aorta, the aorta structure is reconstructed. The angle between the slices of the reconstructed aorta and the uniform magnetic field is determined. The surface is triangulated to have sufficient number of nodes to describe the entire shape of the aorta. If the default value of the aorta radius is used then the program reads from a file that has the information of the triangles and the nodes on the aorta surface saved previously. This reduces the computation time.

From the aortic blood flow profile derived from the photoplethysmogram (PPG) waveform, the volume of blood in each slice of the aorta is calculated at different time segments throughout the heart cycle. Based on the volume of blood in each slice of the aorta, the voltage induced in that particular slice is determined by using magneto-hydrodynamic equations. Since the MHD equation is a complex integral that includes summation expressions and modified Bessel functions, this equation is implemented in Mathcad for faster performance. The MATLAB program invokes the Mathcad program to perform this computation using ActiveX server. The Mathcad program outputs the voltage induced at all the nodes on the aorta.

The next process is to determine the transfer matrix that transfers the potential induced on the surface of the aorta to the thorax. Matrix multiplication of the potential induced at the nodes on the aorta and the transfer matrix gives the potential on the thorax. This is the potential on the thorax induced due to the flow of blood in the aorta in the presence of a uniform static magnetic field. This induced voltage is modified so that it complies with the WCT terminal and then subtracted from the elevated T wave to give an artifact free ECG signal.

Figure 41 shows the triangulated heart, aorta and thorax surfaces. There is an option to rotate these structures. The magnetic field strength, the radius of the aorta, the differential pressure component, the ECG signal and the PPG signal can be entered in this window. Also the orientation of the aorta can be changed. When the “change” button is clicked, the program opens a new window (Figure 44) where the angle of the aorta with respect to

the heart in two orthogonal directions can be changed. After all the input parameters are entered and the “Start Computations” button clicked, the program performs the various computations. The figure in the right bottom shows the ECG in the MRI and the ECG without the elevation at the lead selected by the drop box above the figure.

Figure 42 shows the original ECG signals (red) and the ECG signals without the elevation at the 12 leads. The relation between these two signals at all the 12 leads is discussed in chapter 6.

Figure 43 gives the option to select any node on the aorta and see the potential induced at that particular node. The user can see that the potential is maximum when the blood flow is perpendicular to the magnetic field and decreases as the angle between the blood flow and the magnetic field decreases.

Figure 44 shows the window to change the orientation of the aorta with respect to the heart. After entering the angles and after clicking the “Compute transfer with new angles” button the program determines the transfer matrix used to transfer the potential from the aorta to the thorax.

Figure 45 shows the aortic blood flow, the ECG in a magnetic field, corrected and filtered ECG and the induced potential. Also this window displays the heart rate computed from the ECG and the pulse wave velocity determined from the ECG and the PPG.

Figure 46 shows the potential induced on the surface of the aorta. The color transition from red to blue indicates maximum positive to minimum negative voltage induced. When the “start animation” is clicked, the change in potential on the surface of the aorta is displayed as an animation, as the blood flows through the aorta.

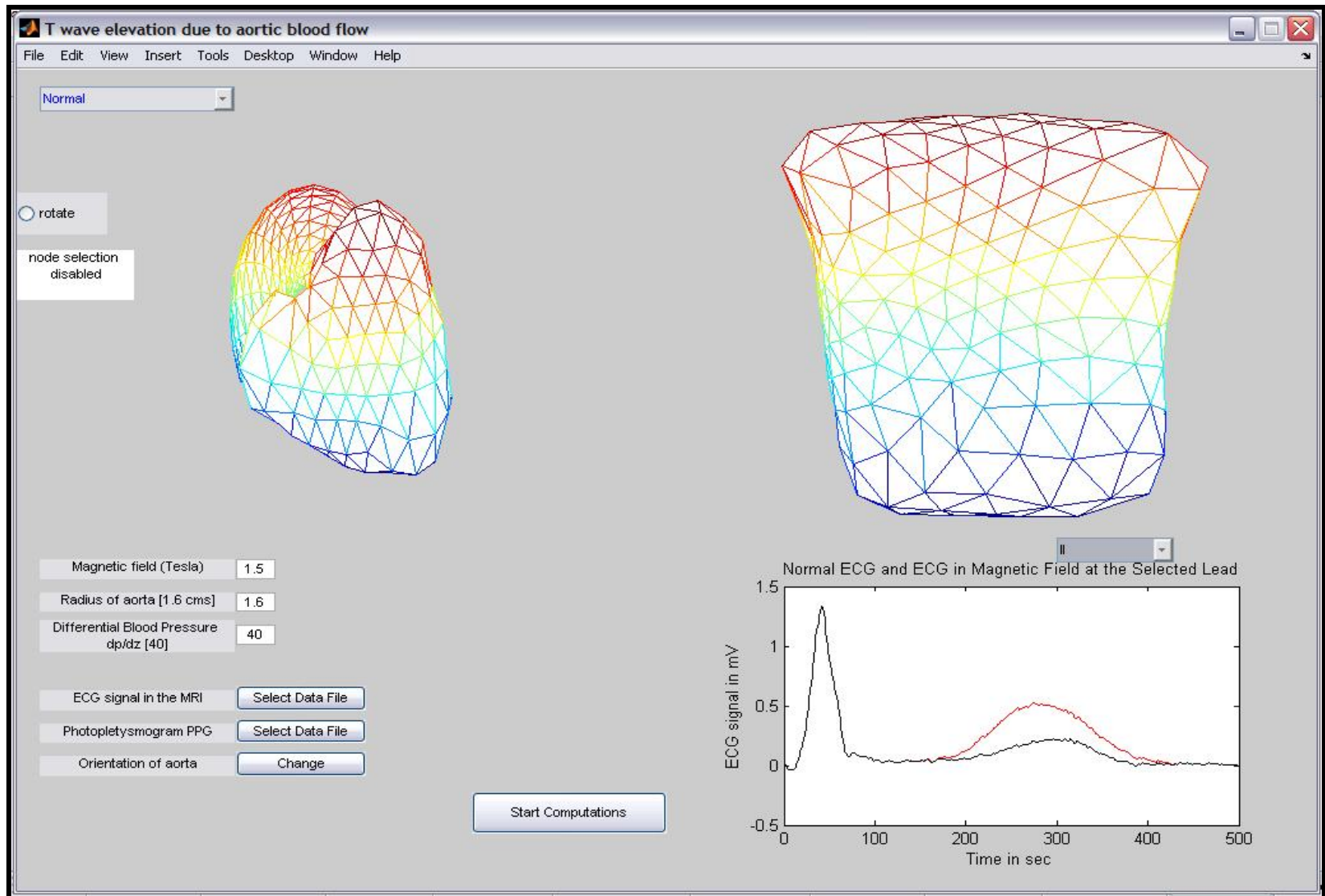


Figure 41 Main screen of the simulation package showing heart, thorax and aorta model.

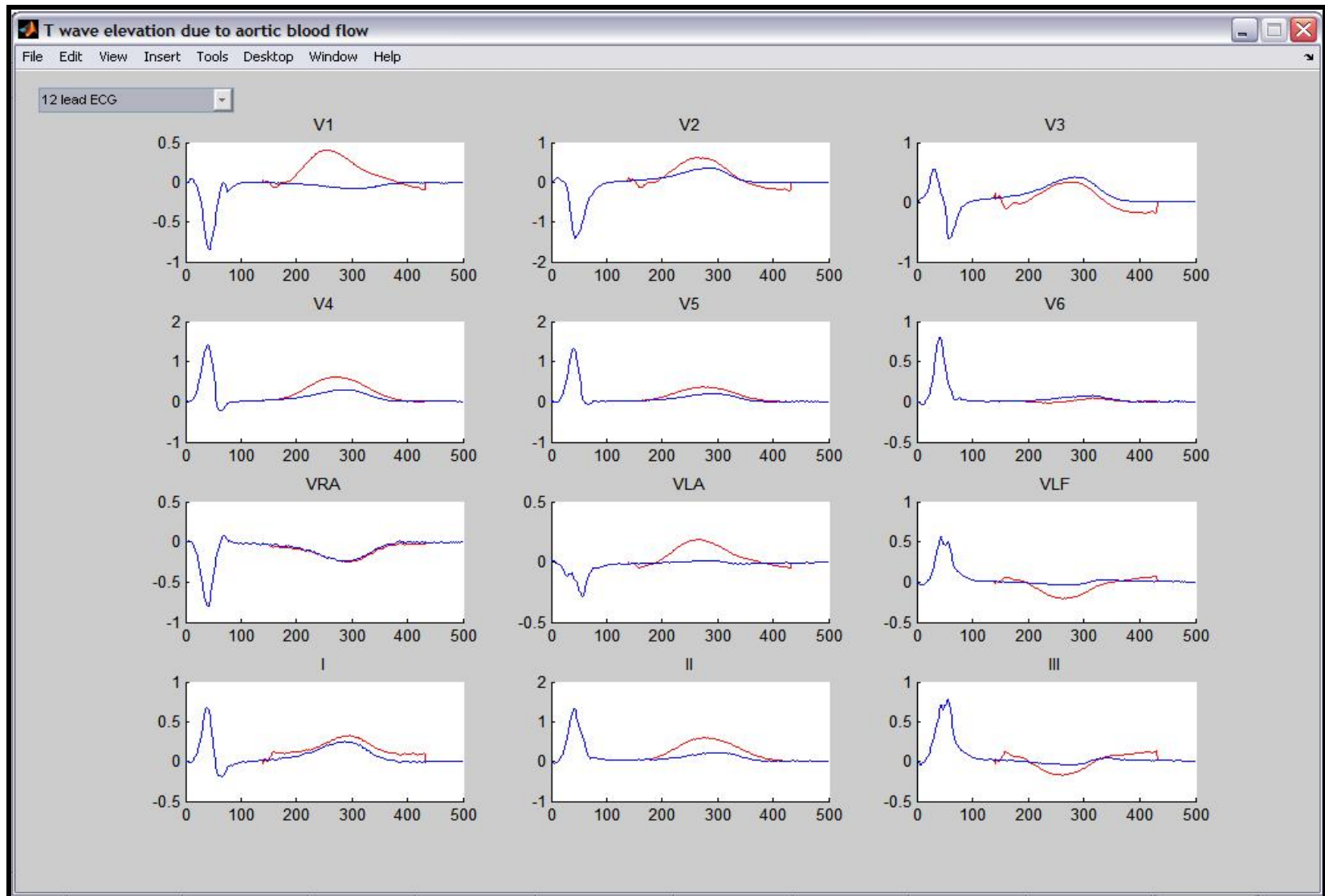


Figure 42 Second scene showing the original ECG and the ECG in the MRI at the 12 leads.

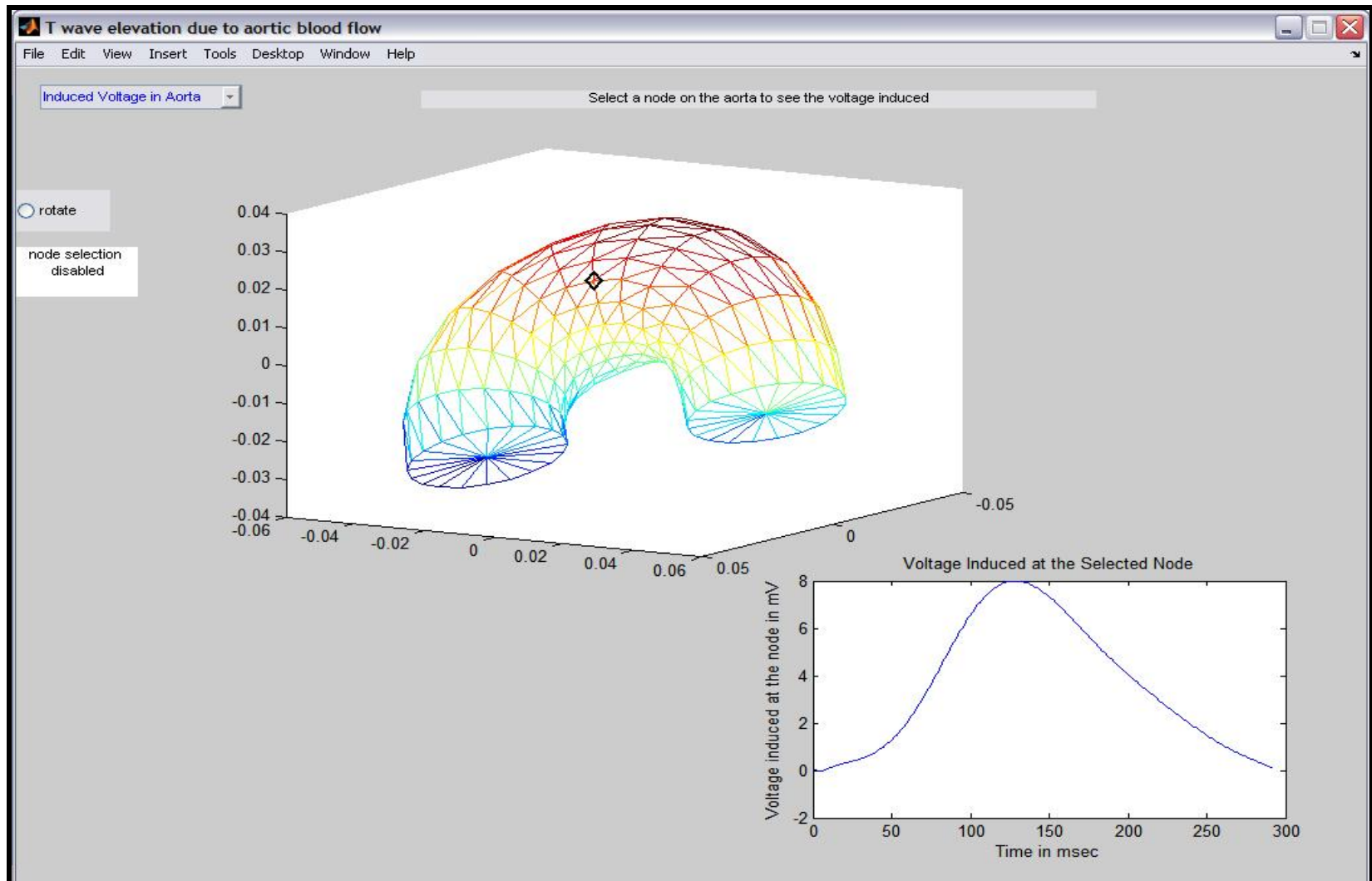


Figure 43 Third Scene showing the model of the aorta and the potential induced at the node selected (heavy black rectangle on the model of aorta).

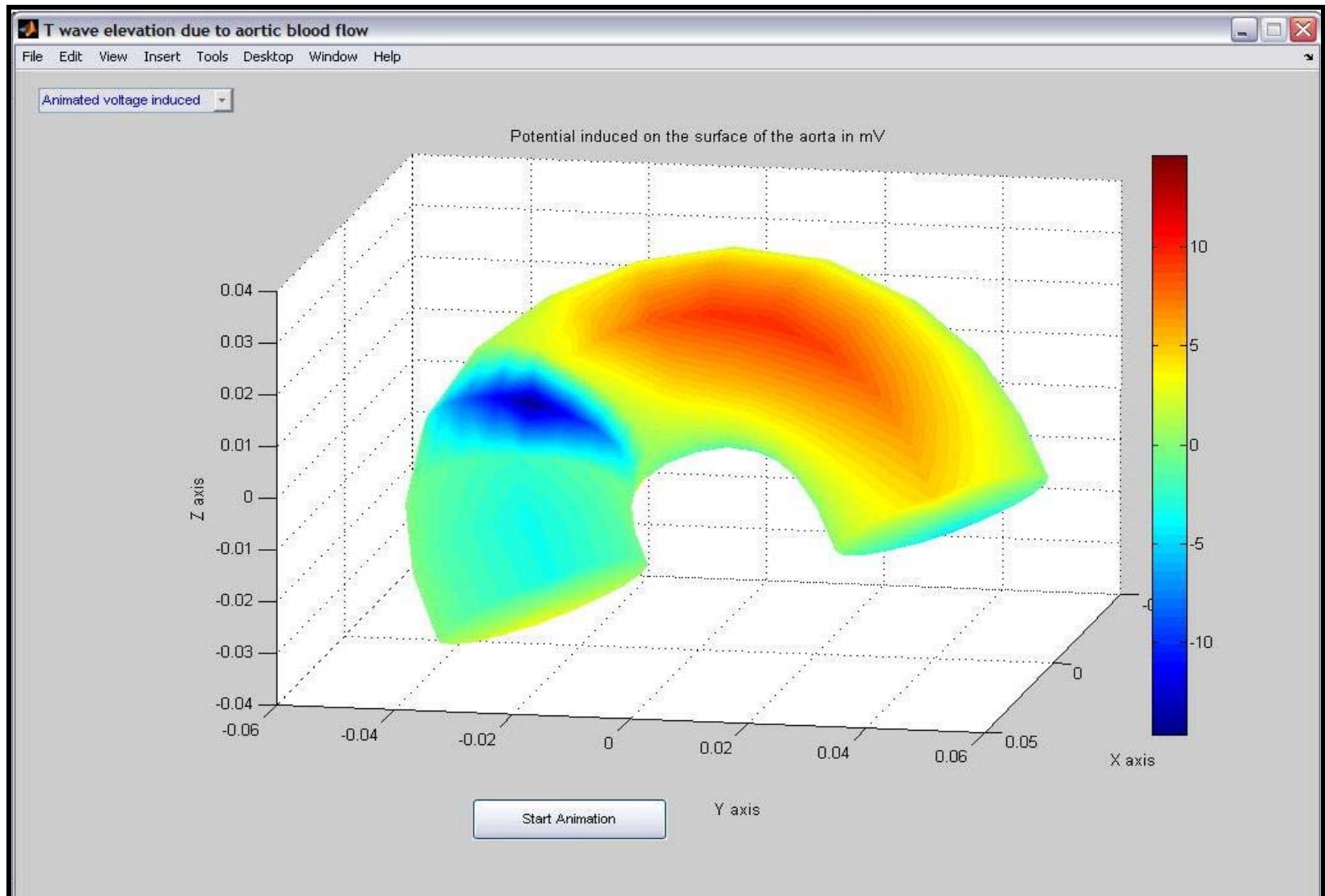


Figure 44 Screen with the option to change the orientation of the aorta with respect to the heart.

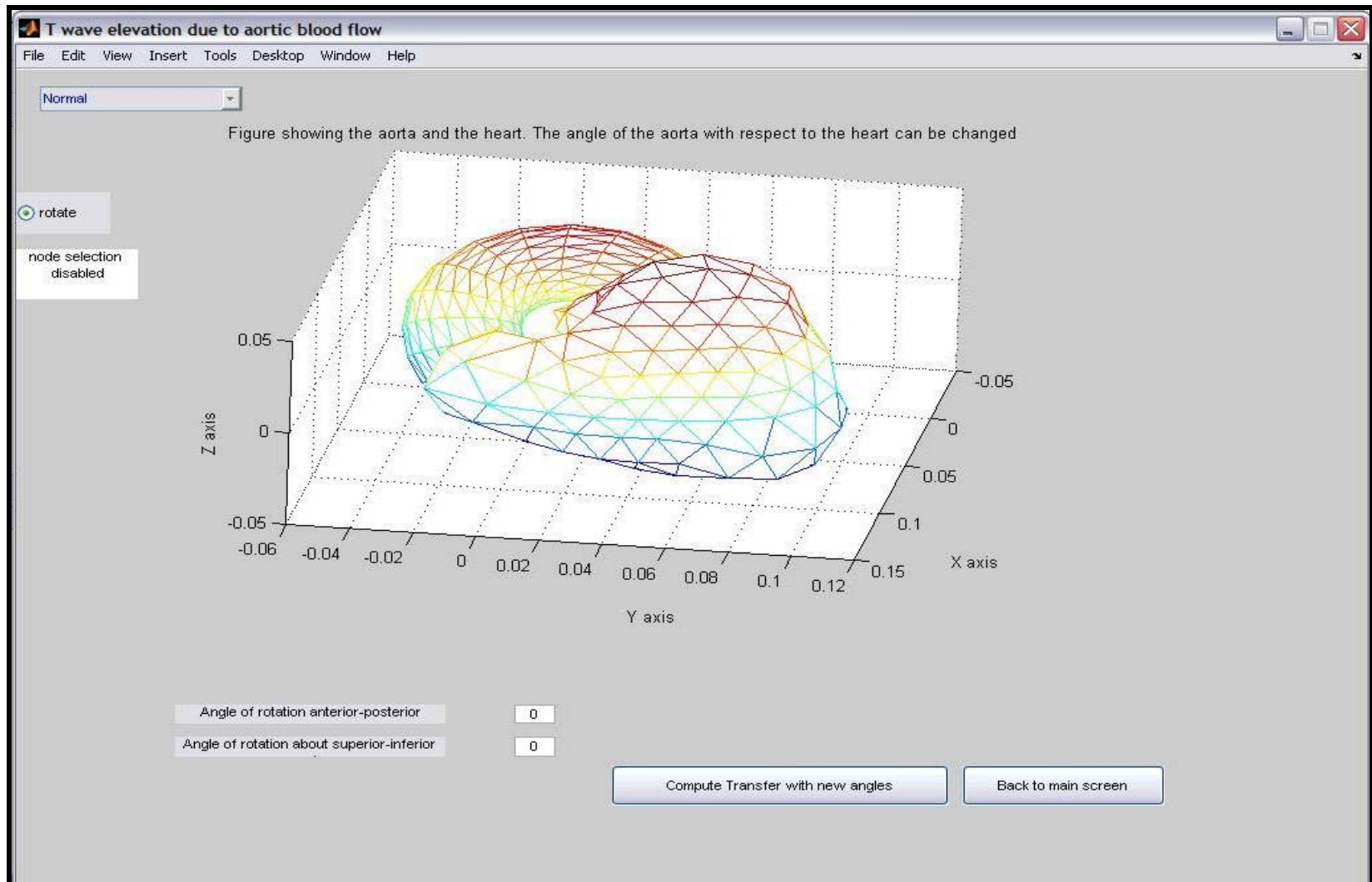


Figure 45 Final screen showing the aortic blood flow, the ECG in a magnetic field, corrected and filtered ECG and the induced potential.

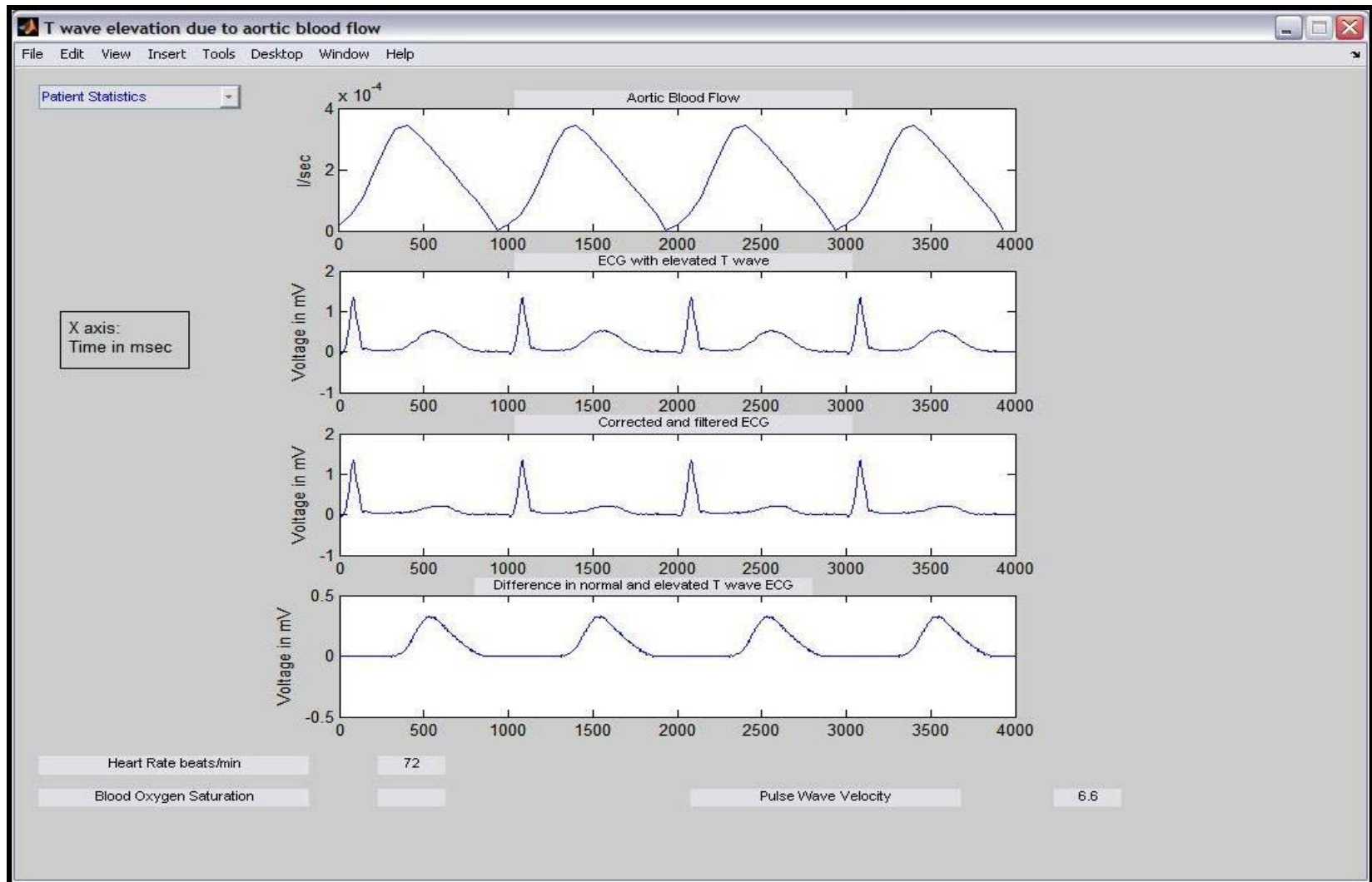


Figure 46 Potential induced on the surface of the aorta. Color transition from red to blue indicates maximum positive to minimum negative.

The next chapter discusses linear least mean square (LMS) adaptive filters used as a method to remove the magnetic induced variation in the T wave of an ECG signal. First the adaptive filters are implemented on the ECG signals from the simulation package. A model is discussed which uses the adaptive filters as a tool to effectively cancel out the T wave elevation. Standard noise removal filters are introduced in the model and finally the adaptive filters are implemented on real data.

CHAPTER 5

LINEAR ADAPTIVE FILTERS TO ELIMINATE T WAVE ARTIFACTS

The output from the computer simulation, discussed in the previous chapter, is a good starting point to determine if a linear adaptive FIR (finite impulse response) filter can be used to remove the T-wave artifact, induced when a patient is subjected to the strong magnetic field of the MRI. The ECG signal with the elevated T-wave is used as the input and the original ECG signal outside the MRI is the desired signal to the adaptive FIR filter. The goal here is to develop an adaptive FIR system that can be trained to filter the elevation of the T wave. A block diagram of a LMS (least mean square) FIR adaptive system is shown below in Figure 47 [74, 75]. The objective is to change (adapt) the coefficients of the FIR filter weights, W , so that the signal $y[n]$ matches as closely as possible to the desired signal $d[n]$.

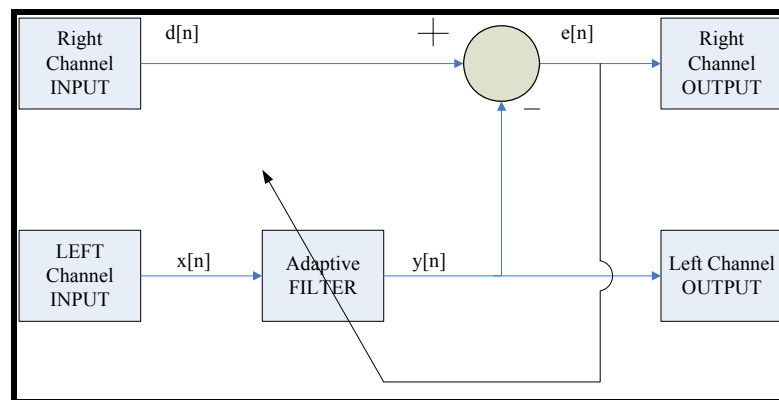


Figure 47 Linear Mean Square adaptive filter.

The adaptive filter weights, W , is trained using the least mean-square algorithm, which is the most widely used adaptive filtering algorithm. First the error signal, $e[n]$, is computed as $e[n] = d[n] - y[n]$, which measures the difference between the output of the adaptive filter and the desired signal $d[n]$. On the basis of this measure, the adaptive filter will change its coefficients in an attempt to reduce the error. The LMS coefficient update equation is [74]:

$$W[n+1] = W[n] + \mu \cdot e[n] \cdot x[n] \quad (110)$$

where $W[n]$ is the vector of FIR filter coefficients at time n , $e[n] = d[n] - y[n]$ is the error between the desired and output signal at the n^{th} time instant, μ is the step size, and $x[n]$ is the vector of current and past input samples.

The step-size μ directly affects how quickly the adaptive filter will converge toward the desired signal [74]. If μ is very small, then the coefficient changes only a small amount at each update, and the filter converges slowly. With a larger step-size, more gradient information is included in each update, and the filter converges more quickly; however the final residue error achieved increases as the step size increases.

5.1 Implementation of the LMS filter on simulation results

In this section, the adaptive filter is implemented on signals from the simulation package. The ECG signal from the simulation package ECGSIM is used as the desired response for the adaptive filter. The ECG signal obtained after adding the T wave elevation due to the

magnetic field computed using the Lorentz's equation is used as the input signal. The size of the weight vector is 15. The adaptive filter is implemented on 4000 data points, eight ECG cycles of 500 samples each. The main purpose of this implementation is to determine whether a linear adaptive filter can remove the T wave artifact. Hence no noise is added to the signals at this point. Implementation of the LMS FIR adaptive filter is as follows. The program runs with a 1000 Hz sampling rate.

1. The filter coefficients are initialized to zero at the start of program execution.
2. The left input channel is the input $x[n]$ to the adaptive filter – the elevated T wave ECG signal of the patient in the MRI bore.
3. The right input channel is the reference (desired) signal $d[n]$ – the ECG of the patient outside the MRI bore.
4. The left channel output is the adaptive filter output $y[n]$.
5. The right channel output is the error signal $e[n]$.

The right input channel - the desired signal $d[n]$ is shown in Figure 48. This is the normal ECG of the patient with no static magnetic field. The left input channel $x[n]$ (with elevated T waves), shown in Figure 49, is the ECG of the patient inside the MRI bore and is obtained from the ECGSIM simulation in the presence of a static magnetic field.

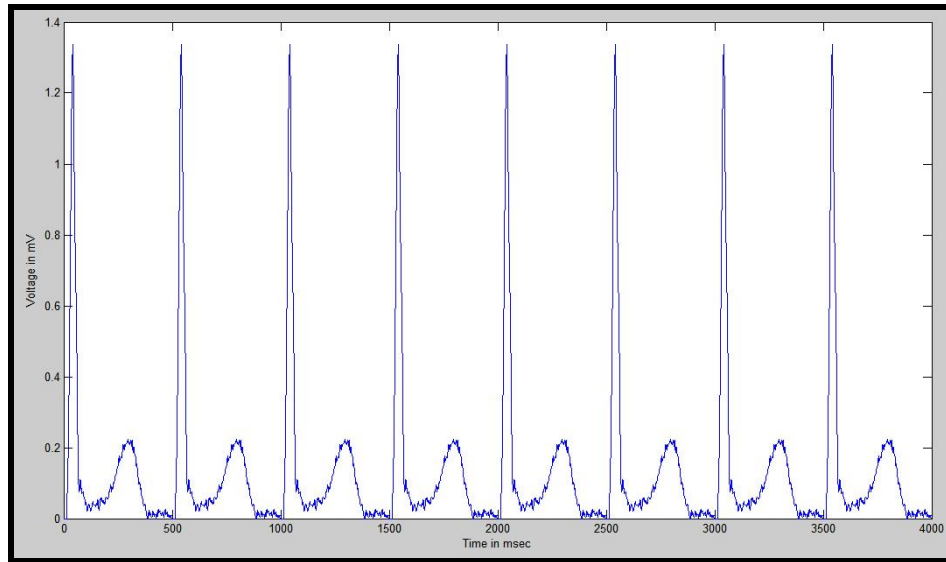


Figure 48 The right channel input – the desired ECG signal.

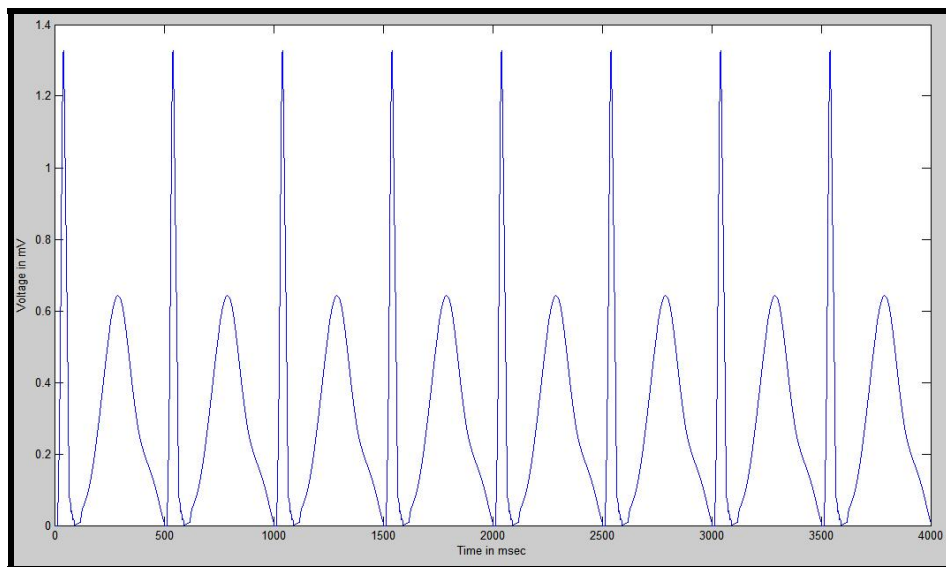


Figure 49 The left channel input – ECG signal with the elevated T wave.

The adaptive LMS FIR filter is implemented using MATLAB. Many simulations on various values of μ are experimented to obtain the best output - the minimum error. The selected step size (μ) is 0.001. The three waveforms – the original ECG signal, the ECG signal in the MRI bore with elevated T wave and the adaptive filter output are shown in

Figures 50 and 51. The adaptive filter output adapts the ECG signal with the elevated T wave to the original ECG signal. The adaptive system shows good adaptation for the T wave of the ECG signal. The adaptive system output has a poor adaptation for the QRS complex of the ECG signal because of the high frequency of the QRS complex. In the adaptive system output, the QRS peak attains a value of 0.6 mV as compared to 1.3 mV in the desired ECG signal.

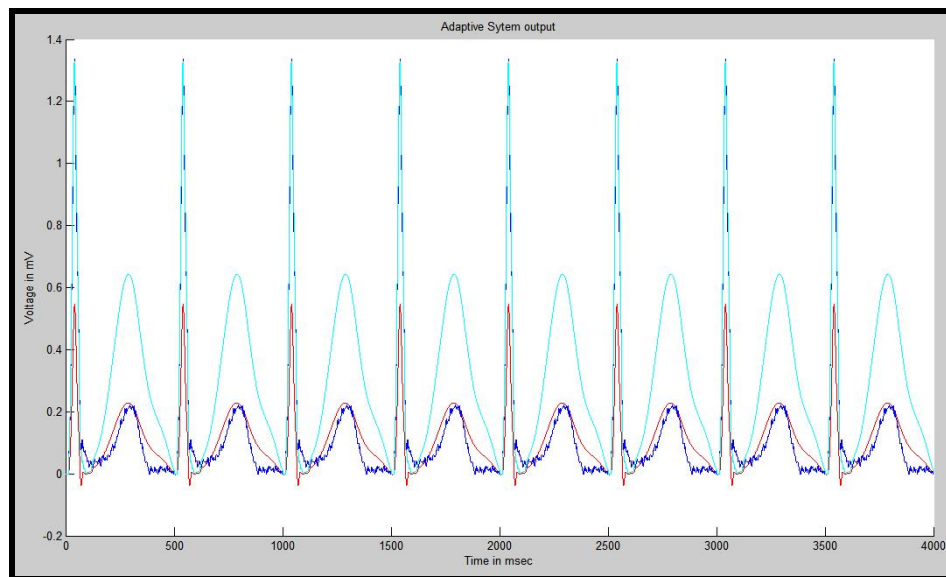


Figure 50 The original ECG, the elevated ECG and the output of the adaptive filter.

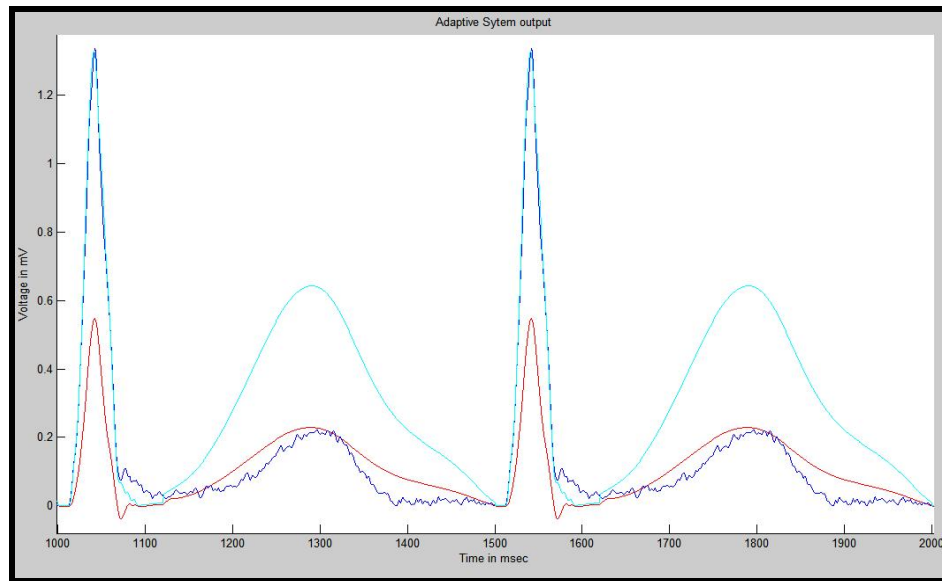


Figure 51 The original ECG, the elevated ECG and the output of the adaptive filter for two ECG cycles.

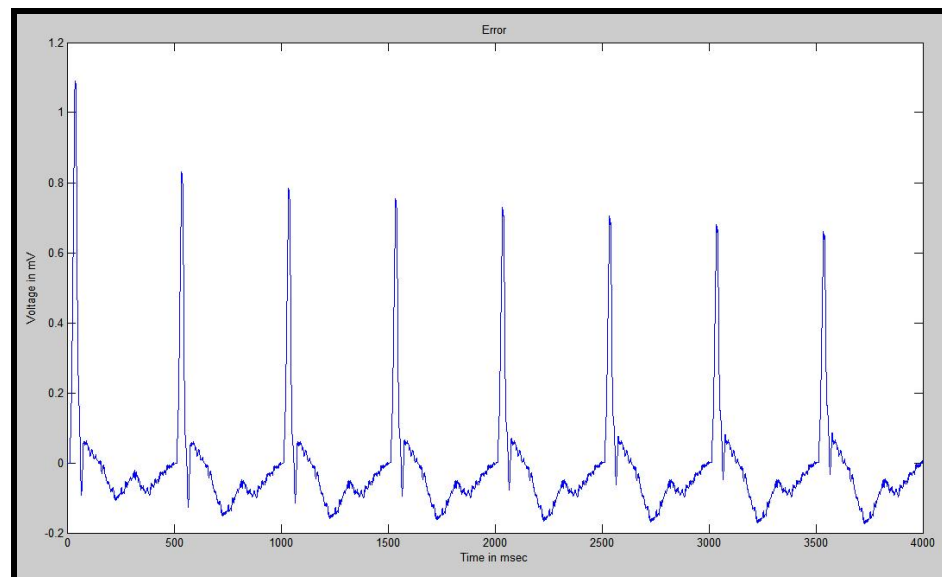


Figure 52 The error signal – the difference between the original ECG and the adaptive filter output.

The maximum error of 0.7 mV is observed between the adaptive system output and the desired signal. This error occurs during the QRS peak of the ECG signal. The adaptation

is good for the T wave of the ECG signal and the error is around 0.04 mV. The error signal is shown in Figure 52.

The results presented here show that the adaptive system works perfectly for the T wave of the ECG signal but fails to adapt to the high frequency QRS peak. In this particular application, the T wave of the ECG signal is distorted due to the strong magnetic field and the adaptive filter adapts well to the T wave of the ECG signal. The output from this section confirms that a linear adaptive system can be used to filter the T wave elevation for noiseless signals. In the next section, the same filter is implemented on noisy signals by corrupting the signals from the simulation package with additive white Gaussian noise.

5.2 Adaptive LMS filter with other noise removal filters

In the hospital environment the ECG signal can be corrupted with various kinds of noises. The LMS adaptive filter discussed in the previous section is implemented on noisy signals to observe the response of the filter. The typical examples of the noise that corrupt the ECG signal are [76]:

1. Power line interference.
2. Electrode contact noise.
3. Motion artifacts.
4. Muscle contraction.
5. Baseline drift.

6. Electrosurgical noise.

The power line interference consists of 60 Hz (or 50 Hz) pickup and harmonics from the power supply. The electrode contact noise occurs as random baseline transition and occurs due to loss of contact between the electrode and the skin. Motion artifacts also occur as transient baseline changes caused due to changes in the electrode-skin impedance. Muscle contraction and electrosurgical noise occurs as random noise in the ECG signal.

To incorporate these noises, the original ECG signal from the simulation package is corrupted with Gaussian noise and baseline wander. The goal here is to make the simulation signals as close as possible to the actual data from the hospital environment. The block diagram of the system implemented in this section is shown in Figure 53.

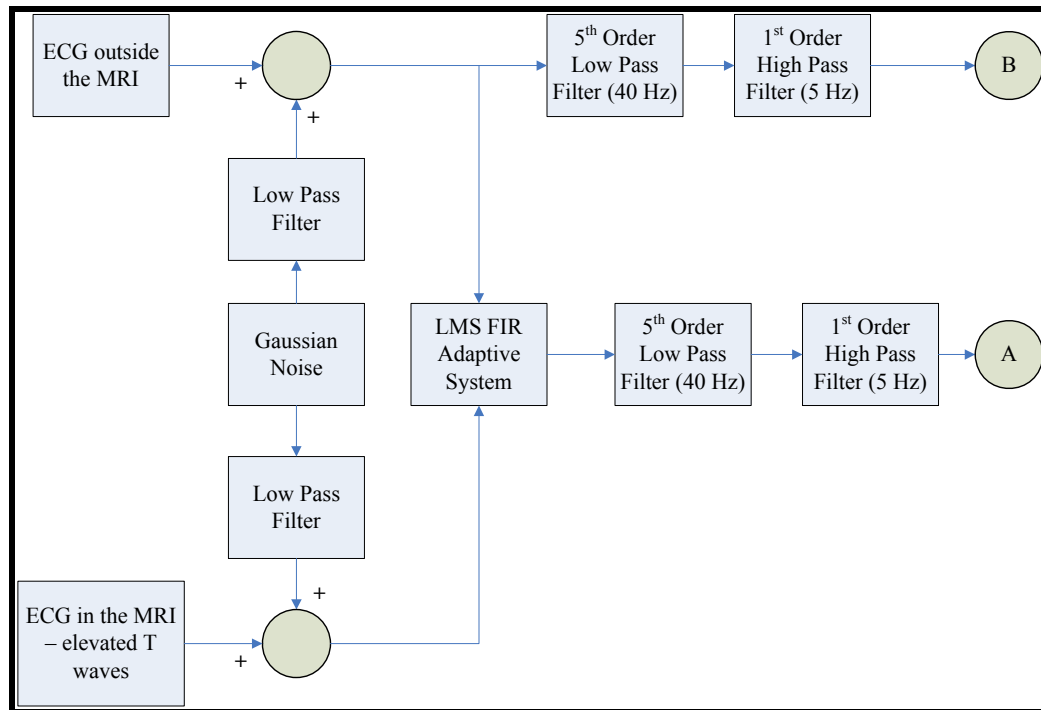


Figure 53 Block diagram of the entire system with noise removal filters.

Noise corrupted ECG signals are the inputs to the LMS FIR adaptive system (Figure 54 and 55). The output from the adaptive system (Figure 56) is then filtered using a fifth order low pass and a first order high pass with cut-off frequencies of 40 Hz and 5 Hz respectively. This is the signal at the point 'A' in the block diagram below. The noise corrupted ECG signal measured outside the MRI room is also filtered using the same two filters. This is point 'B' in the block diagram. The signals at points 'A' and 'B' are compared (Figure 59). Higher the resemblance, the more noise immune is the adaptive system.

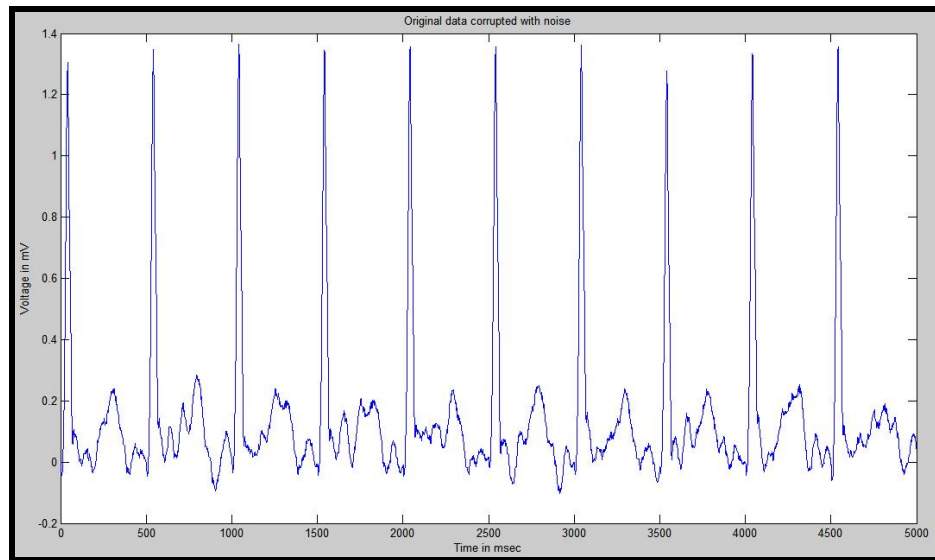


Figure 54 Original ECG outside the MRI room corrupted with noise.

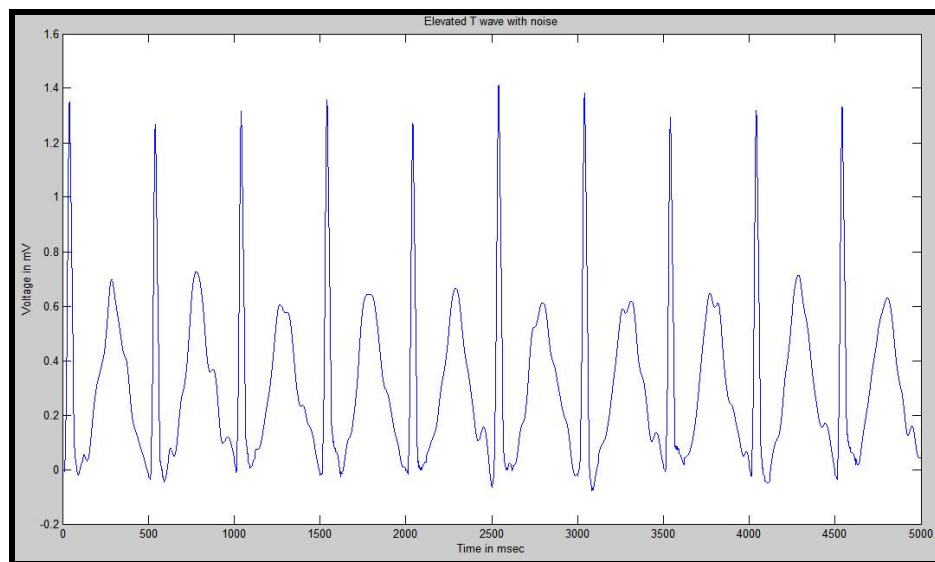


Figure 55 ECG of the patient in the MRI room corrupted with noise.

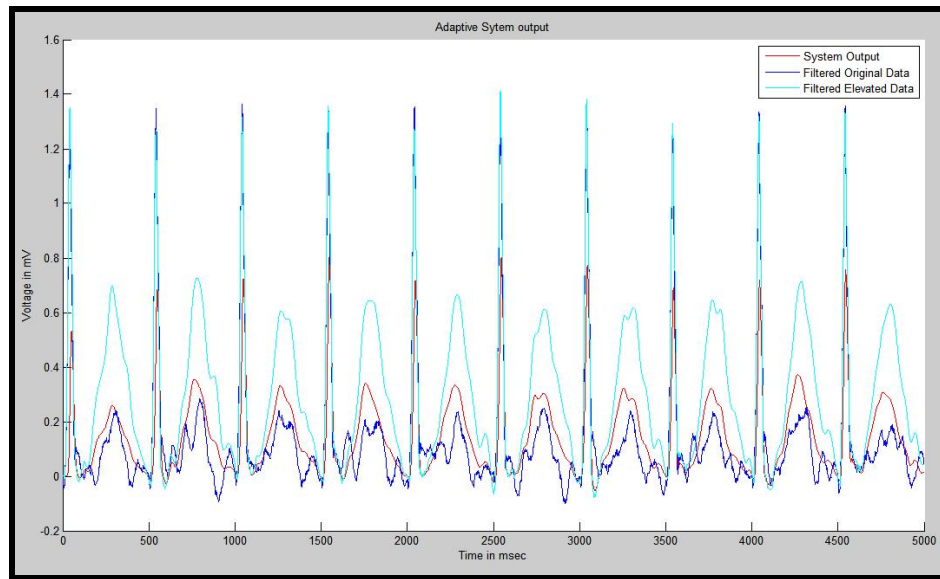


Figure 56 The adaptive system output.

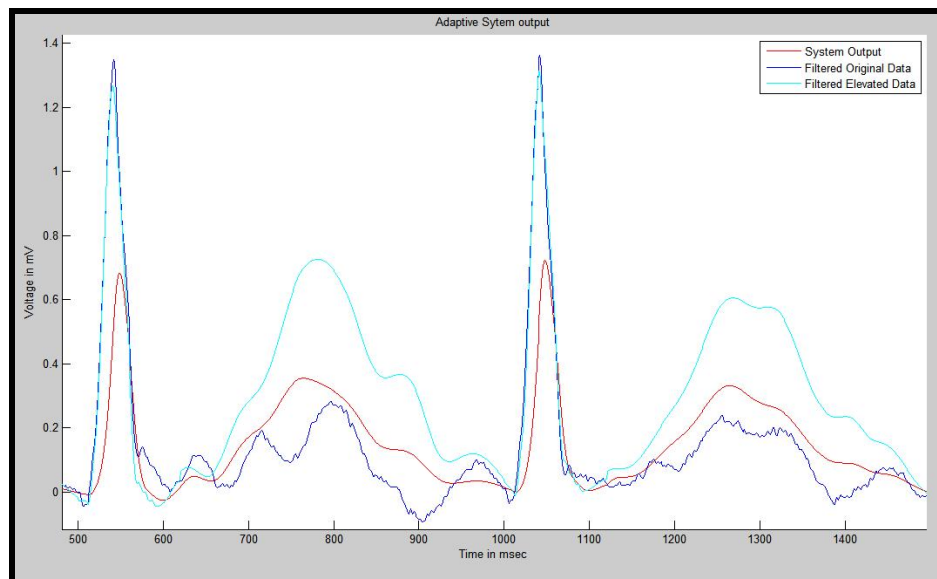


Figure 57 The adaptive system output for two ECG cycles.

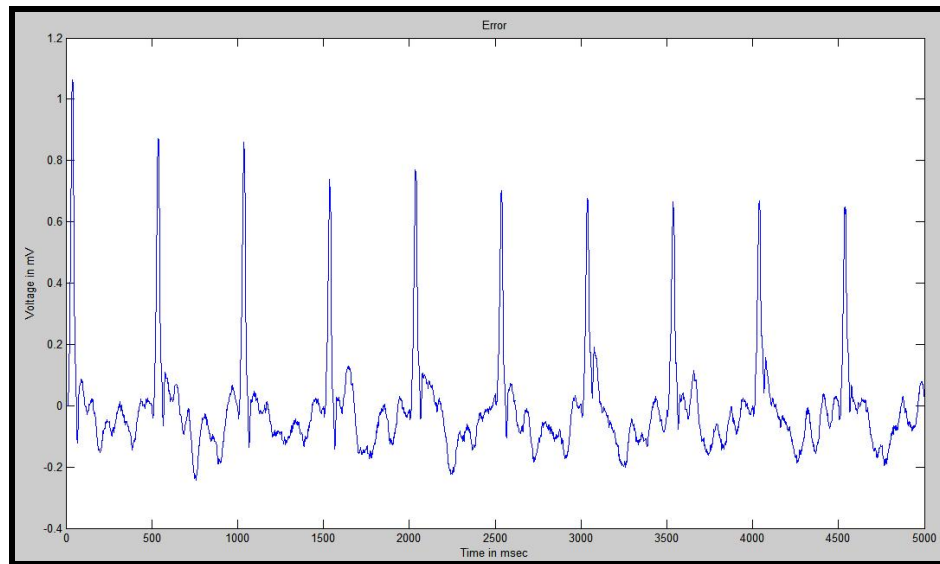


Figure 58 The error of the adaptive system – difference between adaptive system output and original signal.

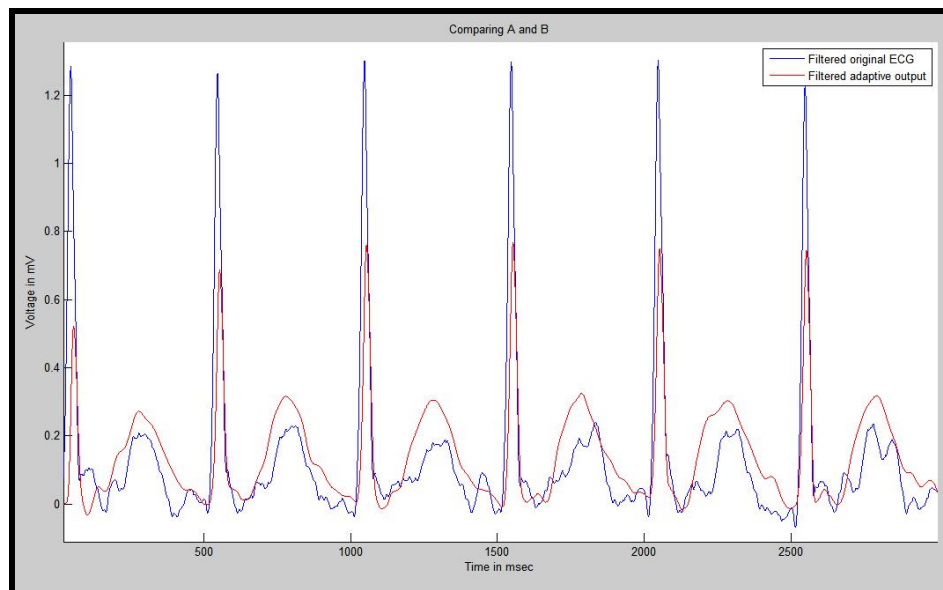


Figure 59 Comparing the signals at points 'A' and 'B'.

The adaptive system adapts the input signal to the desired sequence in the first ECG cycle. The adaptation is good for the T wave of the ECG signal but fails for the QRS peaks. The output is similar to the output of the last section. Hence a linear adaptive filter

works even for noisy signals. Comparing the signals at point A and B (Figure 13), the output from the adaptive system (A) matches the desired signal at point B for the T wave of the ECG signal but fails for the QRS peaks. The signal at point A has QRS peak of 0.8 mV as compared to 1.3 mV for the signal at point B.

The next step is to use the weights obtained from the above adaptive system to filter new ECG data. The ECG signals from the simulation are corrupted with additive white Gaussian noise and then filtered using the FIR filter co-efficient obtained from the LMS algorithm above. The new input signal and the desired signal are shown in Figures 60 and 61. The output of filtering the input signal with the weight vector of the adaptive system is shown in Figures 62 and 63. The error between this signal and the desired signal is shown in Figure 64.

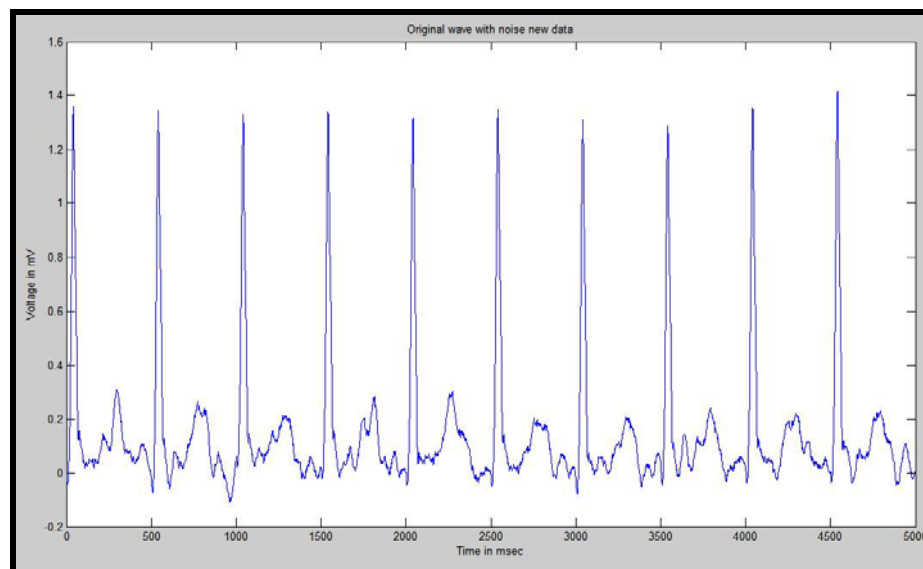


Figure 60 New set of ECG signals – original data outside MRI.

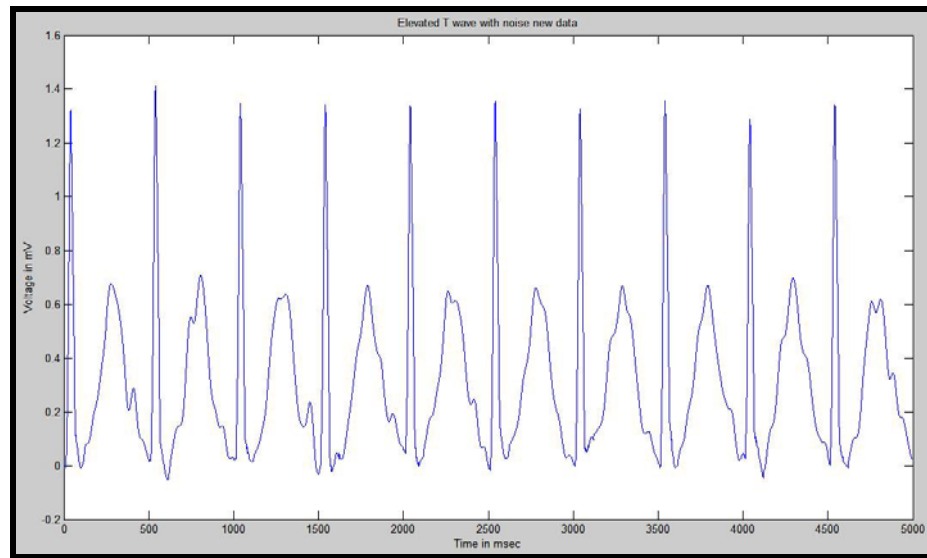


Figure 61 New set of ECG signals – data with elevated T wave in MRI.

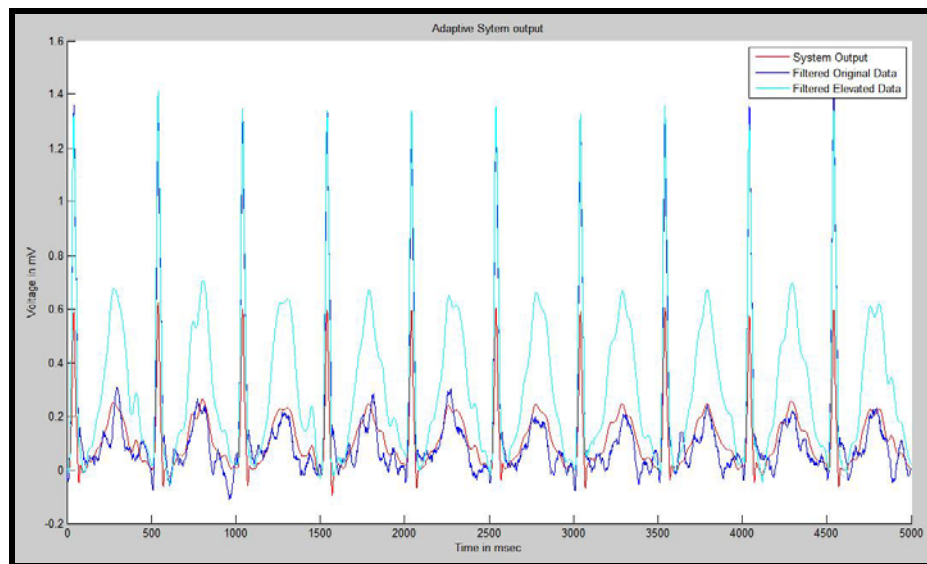


Figure 62 Applying the weights previously computed on new data.

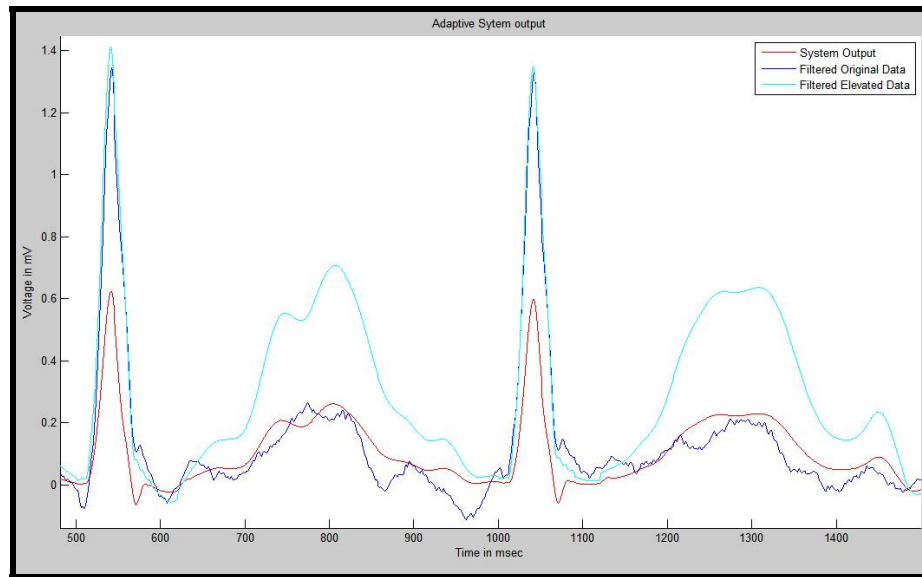


Figure 63 FIR filter output for two ECG signals.

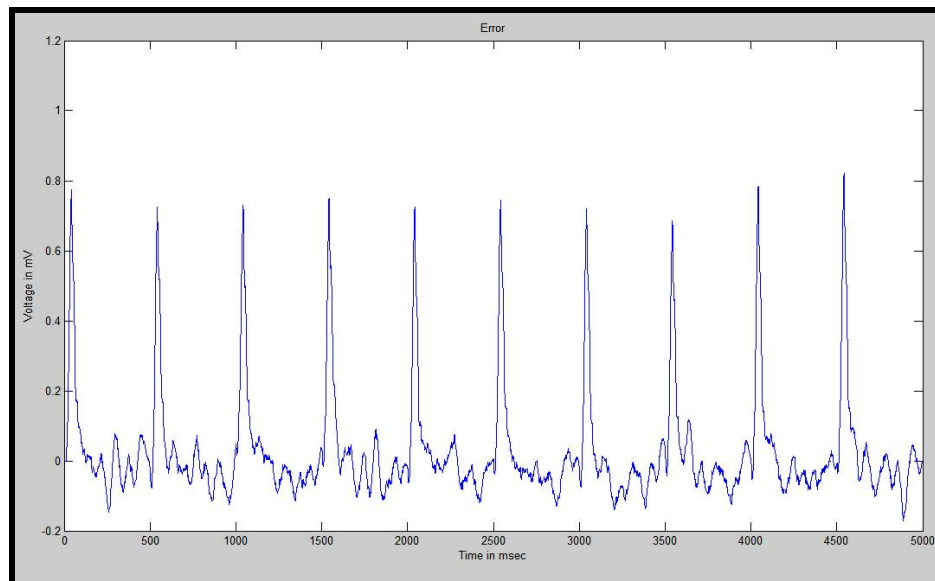


Figure 64 Error signal after applying the filter co-efficient previously computed on new data.

In the above figures, again the same result is observed – the output is extremely good for the T wave of the ECG signal but fails for the QRS complex. In the next section a method is developed in which the adaptive system works on the T wave of the ECG signal and

the T wave elevation due to the static magnetic field is computed and subtracted from the ECG signal in the MRI. Hence in this approach the QRS complex is not disturbed. The entire block diagram, the steps involved and the output of each step is discussed in the next section.

5.3 LMS Filter on the T waves of ECG signal

In this section, the adaptive system is implemented on only the T wave of the ECG signal. From the adaptive system output and the elevated T wave ECG signal, the elevation due to the magnetic field is computed and subtracted from the ECG signal in the MRI. The QRS peaks are not disturbed. The first step is to design linear filters to separate the QRS peaks from the ECG wave. This is achieved by using forth order low pass Butterworth filters. The original ECG wave (Figure 66) and the ECG wave with the T wave artifact (Figure 68) are filtered using this Butterworth filter. In the filtered waves, almost 95% of the QRS peaks are eliminated.

The ECG signals comprising mainly of the T waves are used as inputs to the adaptive system. The elevated T wave (Figure 67) is used as the input and the system adapts to the original T wave (Figure 69). The fact that the ECG signals now contain only the T waves makes the adaptation easier and more accurate. Also the LMS FIR adaptive filter requires lesser number of co-efficients.

The next step is to filter even the small percentage of the QRS complexes to obtain only T wave signals. The non T wave part of the ECG signal is equated to zero. To identify the T waves, the ECG signal in the MRI and the adaptive system output are differentiated and squared. The peaks in the output signal are then identified by detecting the change in slope of the signals. Also since the signals filtered with the Butterworth filter (used to remove the R wave) are free from any noise, the chance of any false detection is completely eliminated. This process detects the starting, ending and the peak of each T wave (Figure 71). Figure 65 shows the block diagram of the proposed system.

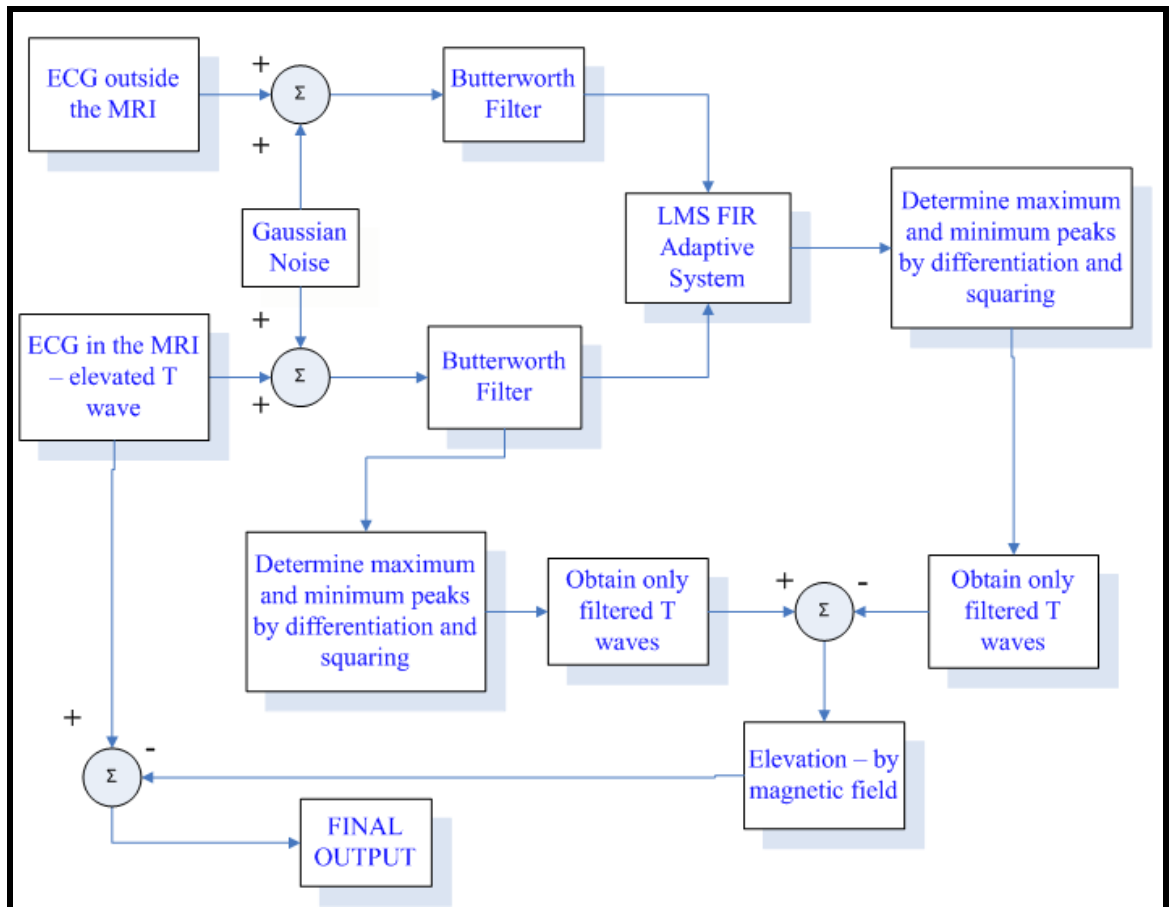


Figure 65 Block diagram of the entire system.

Since the T wave of the ECG signal is identified, the non T wave part of the ECG signal is equated to zero. This is necessary to obtain the signal containing only the elevation of the T wave due to the magnetic field. This elevation thus obtained (Figure 63) is then subtracted from the ECG of the patient with the T wave artifact (Figure 68). The resultant wave (Figure 74) is the ECG of the patient free from T wave elevation artifacts.

The entire process is simulated using MATLAB software. The data is obtained from the ECGSIM simulation package discussed earlier. This data is corrupted using Gaussian noise with zero mean and a variance of 25. After applying the Butterworth filter, the filtered wave consists of only the T wave with a negligible percentage of the QRS peaks. The adaptive system step size is selected as 0.001.

A major advantage of this method is that the entire system uses the filtered Butterworth outputs signifying that we are working on noise free signals. The probability of false detection after differentiation and squaring is also eliminated. Another advantage is that in this system the elevation caused by the magnetic fields is obtained. Finally, the outputs using this system have an extremely small error. The QRS peaks are untouched and the T wave artifact is removed. This method works well on simulation signals; in the next section this method is implemented and improvised for use on real data signals.

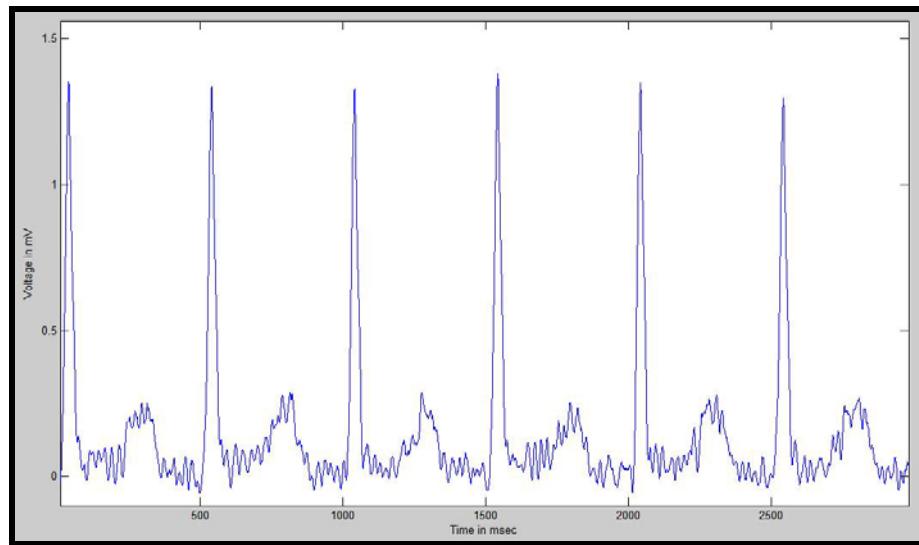


Figure 66 The original ECG signal (outside MRI) corrupted with additive Gaussian noise.

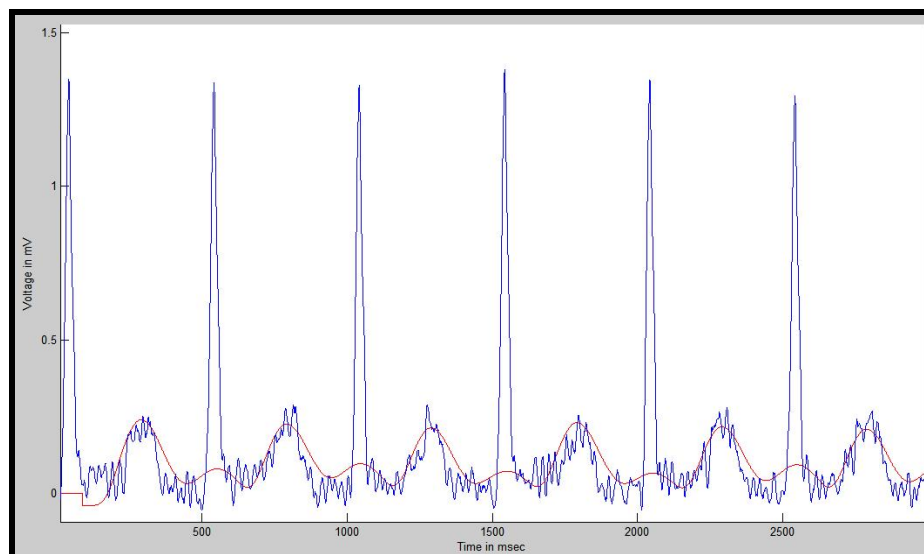


Figure 67 Forth order Butterworth filter output showing the original ECG and the filtered wave (comprising of only the T waves).

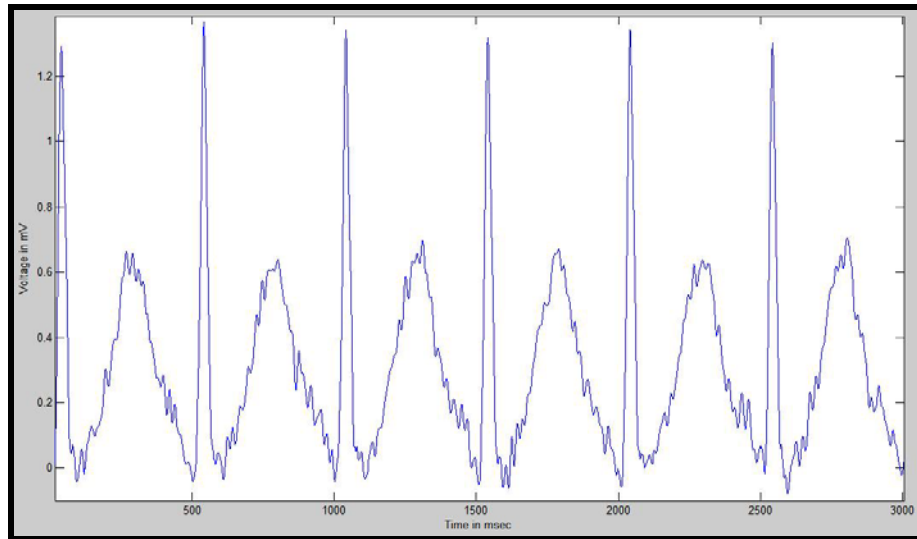


Figure 68 ECG signal with T wave artifact (in the MRI) corrupted with additive Gaussian noise.

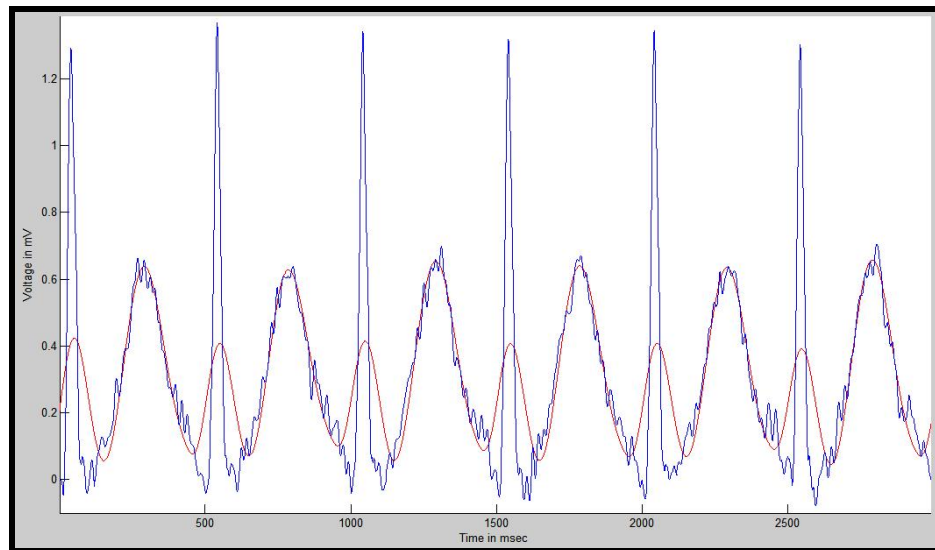


Figure 69 Forth order Butterworth filter output showing the elevated T wave ECG and the filtered signal.

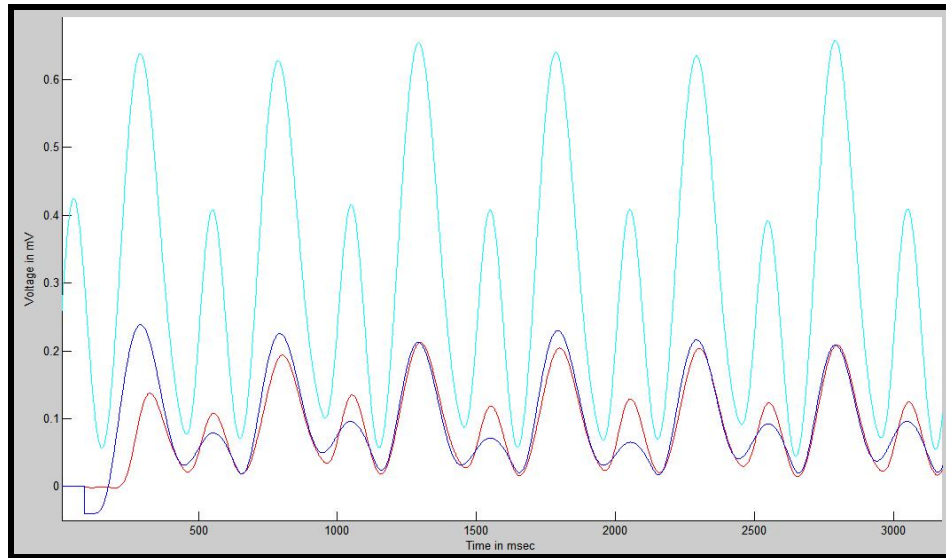


Figure 70 The input, the desired signal and the output of the adaptive system.

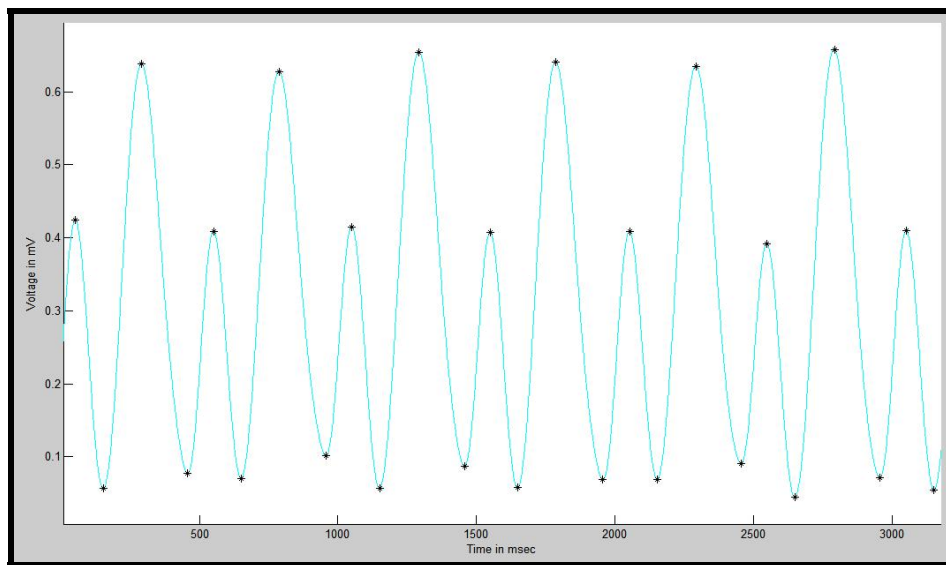


Figure 71 Peak detection algorithms applied to the output of the adaptive system.

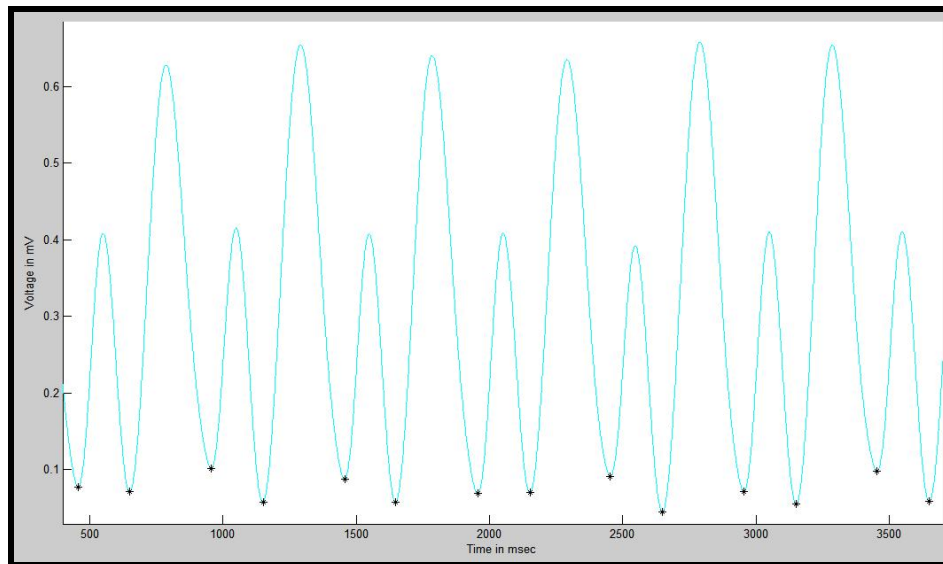


Figure 72 The starting and ending points of the T wave.

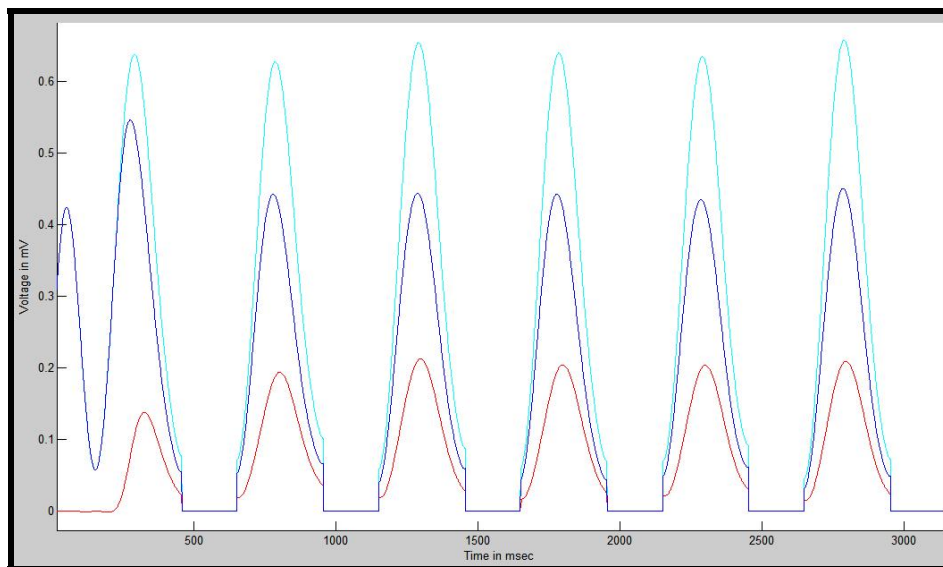


Figure 73 Elevated T wave, the original T wave and their difference – the elevation.

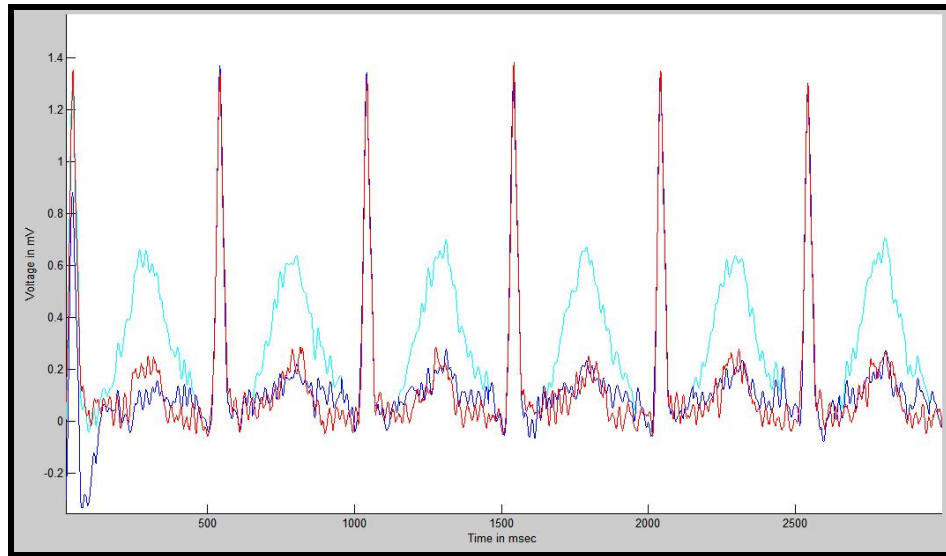


Figure 74 The final output - elevation obtained from the previous stage is subtracted from the elevated T wave ECG signal shown for 6 cycles.

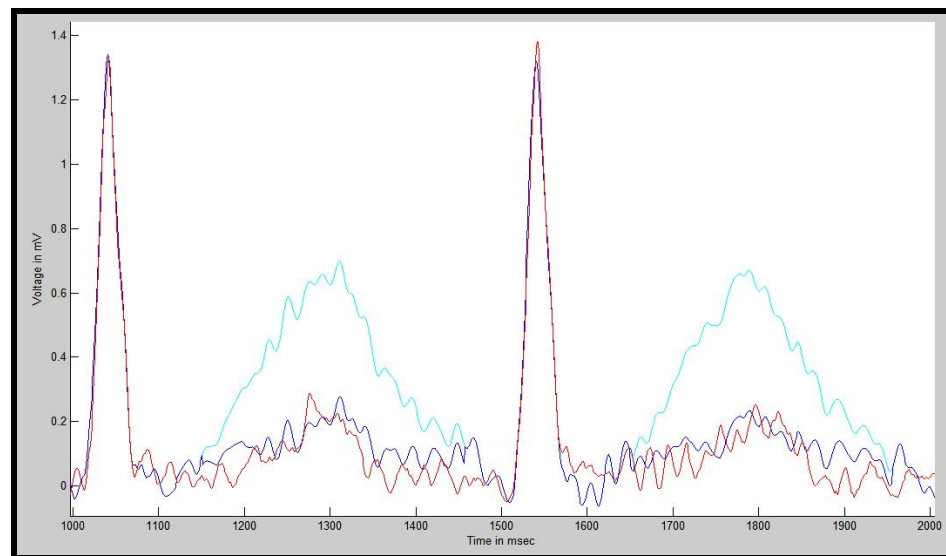


Figure 75 The final output - elevation obtained from the previous stage is subtracted from the elevated T wave ECG signal shown for 2 cycles.

5.4 LMS Adaptive Filter on Real Data

The ECG data of a patient in the MRI room and the ECG before entering the MRI room is recorded for 60 seconds at a sampling frequency of 1000 Hz (60000 samples). The ECG signal recorded in the MRI room has a T wave peak of 9 mV as compared to 2 mV in the ECG outside the MRI. In the previous sections, the results of the adaptive system on data from the simulation package were discussed. The original ECG signal and the elevated T-wave ECG signal from the computer simulation were used as inputs to the adaptive LMS filter. The adaptive system output adapted extremely well for the T wave of the ECG signal but failed to adapt to the QRS peaks.

In this section, the ECG signal outside the MRI is first interpolated or decimated to match the heart rate of the ECG signal in the MRI. The adaptive system is then implemented with this modified ECG signal as the desired signal and the ECG signal in the MRI as the input signal. The QRS peaks of the adaptive system output are then replaced with the QRS peaks of the ECG signal in the MRI. The block diagram in Figure 76 shows all the steps involved.

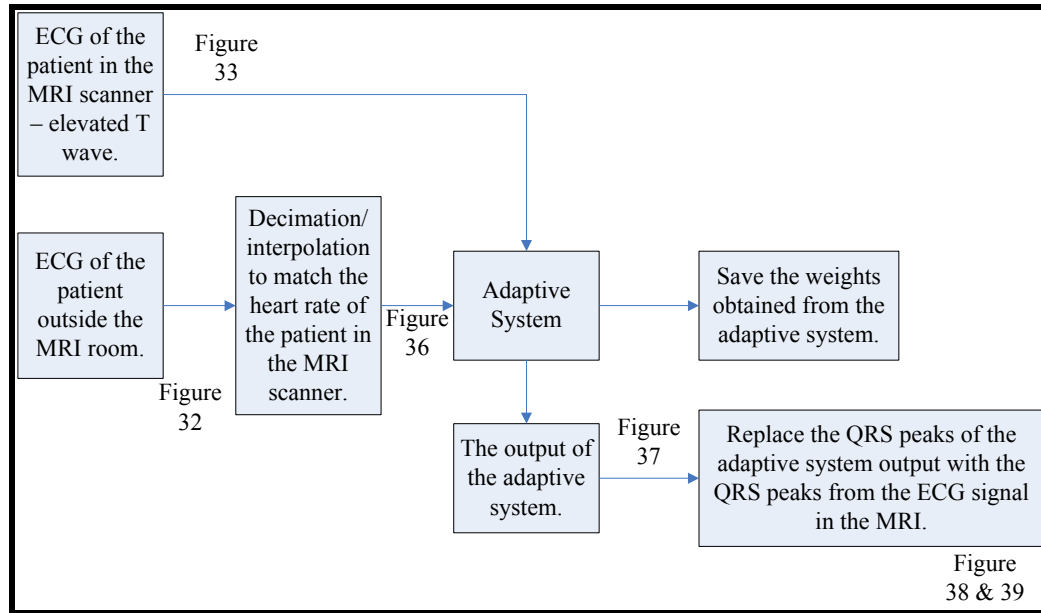


Figure 76 Block diagram of entire system for real data.

The above block diagram uses the QRS peak detector algorithm by Pan and Tompkins [77], for determining the heart rates of the ECG signal in the MRI and outside the MRI. Before discussing the details of the above block diagram, the QRS peak detection algorithm is discussed in the next section.

5.4.1 QRS peak detection algorithm

The algorithm developed by Pan and Tompkins [77] is a real time algorithm to detect the QRS complexes in the ECG signal using information of the slope, amplitude and the width of the QRS complex. The algorithm uses a band pass filter to reduce false detections and adjusts the thresholds automatically as the ECG signal changes. The algorithm uses linear digital filtering (band pass filter, derivative and moving window integration), nonlinear transformation (squaring) and decision rule algorithms.

There are various steps involved in the QRS peak detection algorithm [77]. In order to reduce the noise in ECG signals, the first step uses a digital band pass filter (5 to 15 Hz) composed of a cascaded high-pass and low-pass filter. The band pass filter attenuates muscle noise, 60 Hz interference, baseline wander and T wave interference. The second order low pass filter with a cut-off frequency of 11 Hz and a gain of 36 is implemented by the difference equation:

$$y(nT) = 2y(nT - T) - y(nT - 2T) + x(nT) - 2x(nT - 6T) + x(nT - 12T) \quad (111)$$

The delay of the filter is five samples. This signal is passed through a high pass filter of cut-off frequency 5 Hz, gain of 1 and delay of about 16T. The difference equation of this high pass filter is given by:

$$y(nT) = y(nT - T) - x(nT)/32 + x(nT - 16T) - x(nT - 17T) + x(nT - 32T)/32 \quad (112)$$

The next process after filtering the ECG signal is to differentiate the signal to obtain the QRS complex slope information. A five point derivative with a delay of two samples defined by the difference equation below is used.

$$y(nT) = (2x(nT) + x(nT - T) - x(nT - 3T) - 2x(nT - 4T))/8 \quad (113)$$

After differentiation, the signal is squared point by point. This intensifies the slope of the frequency response curve of the derivative and helps restrict false positives caused by T waves with higher spectral energies. The difference equation for squaring is:

$$y(nT) = [x(nT)]^2 \quad (114)$$

This squaring makes all data points positive and emphasizes the higher ECG frequencies. The moving window integrator is then implemented. This produces a signal that includes information about both the slope and the width of the QRS complex. This is computed by the following difference equation:

$$y(nT) = (1/N)[x(nT - (N-1)T) + x(nT - (N-2)T) + \Lambda + x(nT)] \quad (115)$$

where N is the number of samples in the width of the integration pulse. The selection of N is very important. The width of the window should be approximately the same as the widest possible QRS complex. If the window is too wide, then the integration window will merge the QRS and the T complexes together. If the width is too narrow, a QRS complex may produce several peaks in the integration window. The outputs of the various steps discussed above are shown in Figure 77.

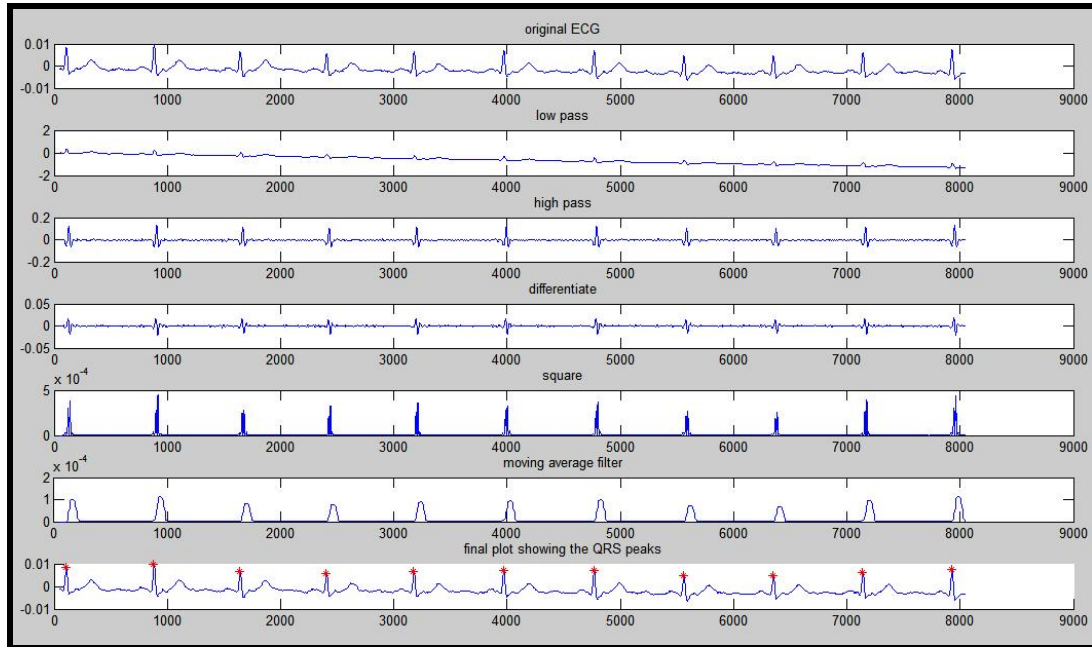


Figure 77 Outputs of the various steps in the QRS detection algorithm.

In Figure 77, the various signals represent: (a) Original signal. (b) Output of band pass filter. (c) Output of differentiator. (d) Output of squaring process. (e) Result of moving window integrator. (f) Original ECG signal delayed by the total processing time. (g) The final output stream.

The algorithm uses two sets of thresholds to detect QRS peaks. One set on the filtered ECG and the other set on the output of the moving window integration. In each set, two thresholds (one half of the other) are used, to improve the reliability of detection and to reduce false negatives. The thresholds are based on the most recent signal and noise peaks and hence continuously adapt to the characteristics of the signal. If in the time interval corresponding to 166 % of the current average RR interval, a QRS complex is not detected then the maximal peak detected in the time interval that lies between these thresholds is considered to be the QRS complex.

For irregular heart beats, both thresholds are reduced by half to increase the sensitivity of detection and to avoid missing beats. Physiologically, QRS complexes cannot occur closer than 200 msec. A refractory period, is a period of time during which an organ or cell is incapable of repeating a particular action, or the amount of time it takes for an excitable membrane to be ready for a second stimulus once it returns to its resting state following an excitation. Hence, after a valid QRS complex is detected there is a 200 msec refractory period, thus eliminating the possibility of multiple triggering and false detection. Two separate measurements of the average RR interval are computed. One RR

interval is the mean of the most recent eight RR intervals and the other is the mean of the most recent eight beats that lie in the range of 92-116 % of current RR interval average. When the heart rate changes suddenly, then the first RR interval average substitutes for the second one. According to the reference [77], the algorithm failed to detect only 0.675 % of the beats.

5.4.2 Signal Processing on real data

The recorded ECG data outside the MRI and in the MRI bore are shown in Figure 78 and 79. The QRS detector [77] discussed is implemented on these two signals. Even though the ECG signal outside the MRI has a strong negative peak after the QRS peak, the QRS detector identified the QRS peaks.

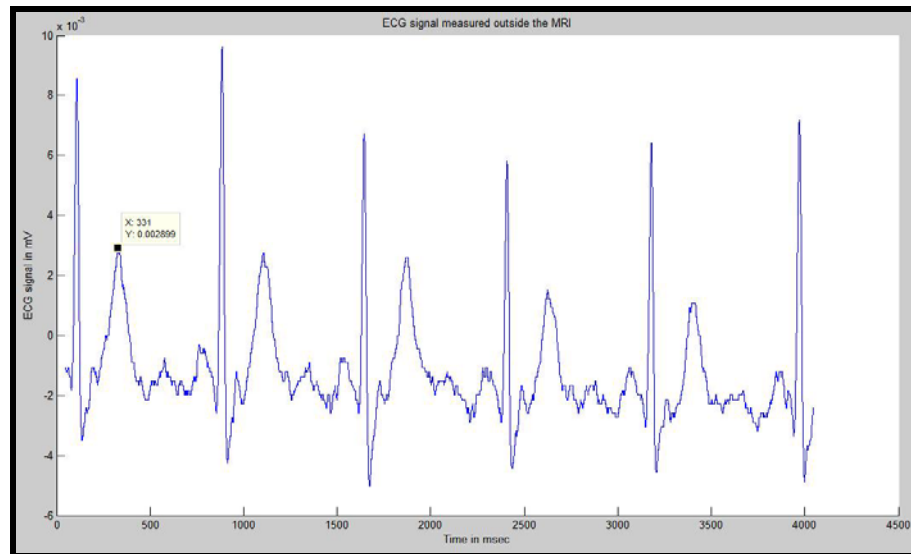


Figure 78 ECG signal outside the MRI.

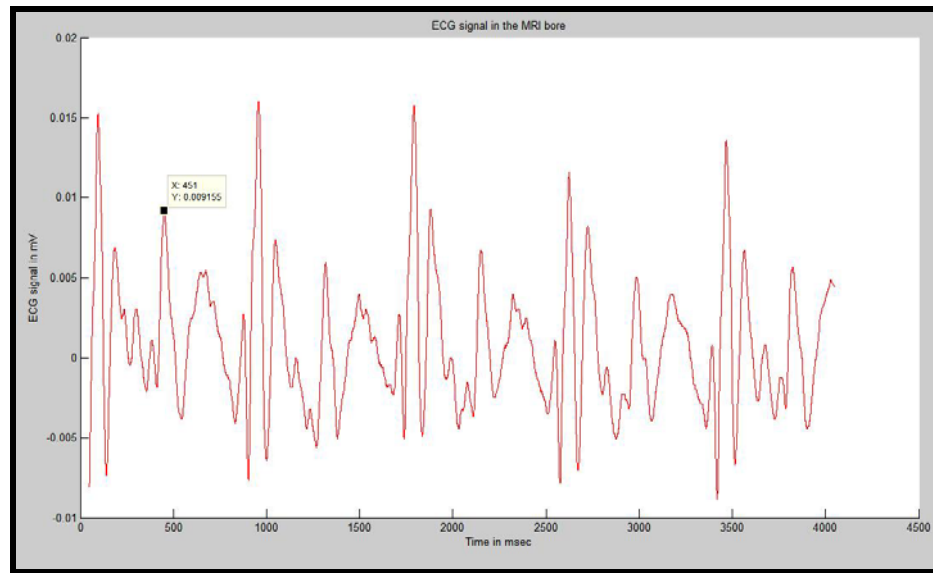


Figure 79 ECG signal in the MRI bore.

The LMS (least mean square) algorithm is implemented with the ECG signal outside the MRI as the desired signal and the ECG signal in the MRI as the input signal. The FIR filter coefficients are obtained from the adaptive system. In the first run, the adaptive system failed to train to the desired data. The step size was varied from 0.001 to 0.95. For each trial the adaptive system output approached the desired response for the first ECG cycle but the weight matrix failed to converge. On closely comparing the two sets of ECG recordings, it is noticed that the patient had a different heart rate outside the MRI and in the MRI room (Figure 80). This varying heart rate caused the adaptive system to fail. If the adaptive system is directly implemented on the signals the adaptive system fails to adapt (as shown in Figure 81).

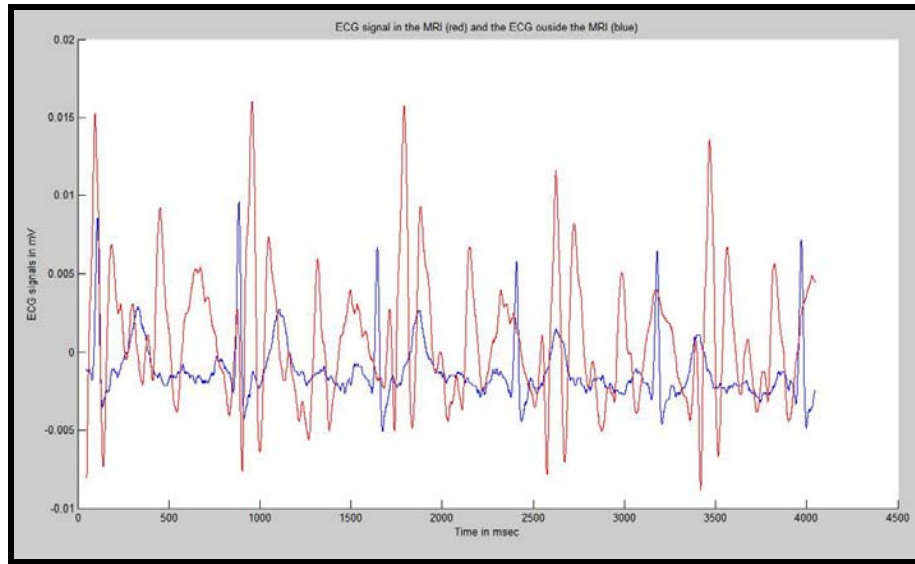


Figure 80 ECG signal in the MRI (higher amplitude) and ECG outside the MRI.

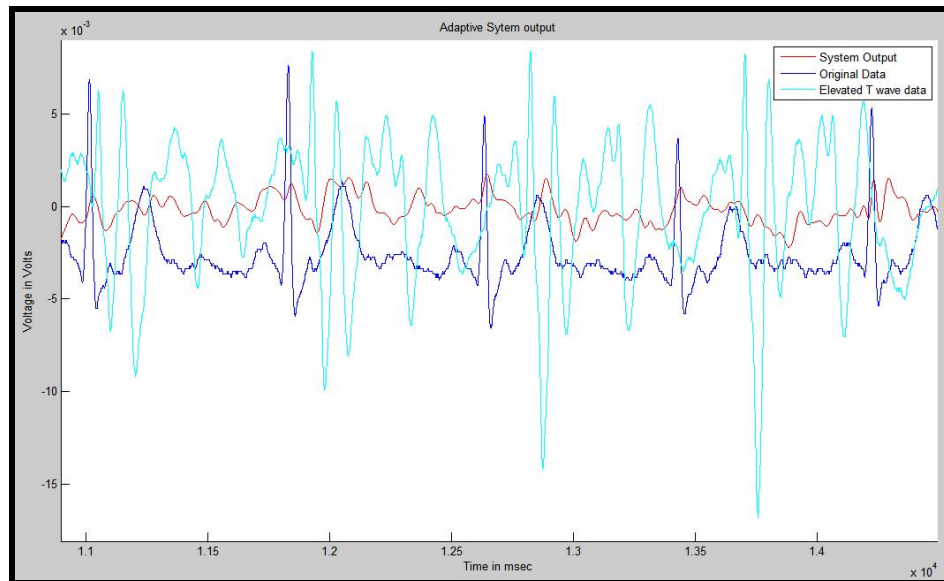


Figure 81 The adaptive system fails when the heart rates of the two signals are not synchronized.

Hence it is essential to match the heart rate of the ECG signal outside the MRI to the heart rate of the ECG signal in the MRI. This is implemented by computing the

difference in the number of samples between the first RR intervals of both the signals. If the number of samples in the first RR interval of the ECG signal outside the MRI is greater then the number of samples in the first RR interval of the ECG signal in the MRI then the first signal is decimated to match the number of samples of the second signal. In the other case, the first signal is interpolated by introducing new samples of magnitude the average of the neighboring samples (linear interpolation). Figure 82 shows the ECG signal outside the MRI modified to match the heart rate of the ECG signal in the MRI and the ECG signal in the MRI.

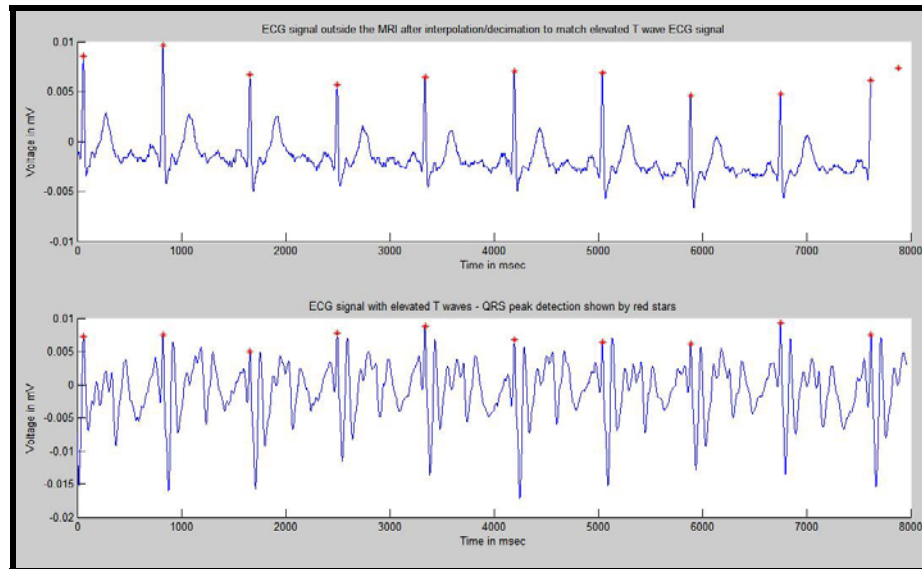


Figure 82 ECG signal outside the MRI (upper signal) is matched to the heart rate of the ECG signal in the MRI (lower signal).

The adaptive system is now implemented on the elevated T wave ECG signal with the modified ECG signal as the desired response. The size of the weight matrix is 15. A non-zero weight matrix is obtained and the adaptive system trains closely to the desired response for the T wave part of the ECG signal. But the QRS peaks fail to adapt. The

adaptive system output shows a positive QRS peak but the system does not adapt completely to the original magnitude of the peak. The adaptive system outputs for the T wave of the ECG signal are extremely good and the magnetic induced potential is filtered. Figure 83 shows the adaptive system output. The T wave adapts well but the QRS peak of the ECG fails to adapt.

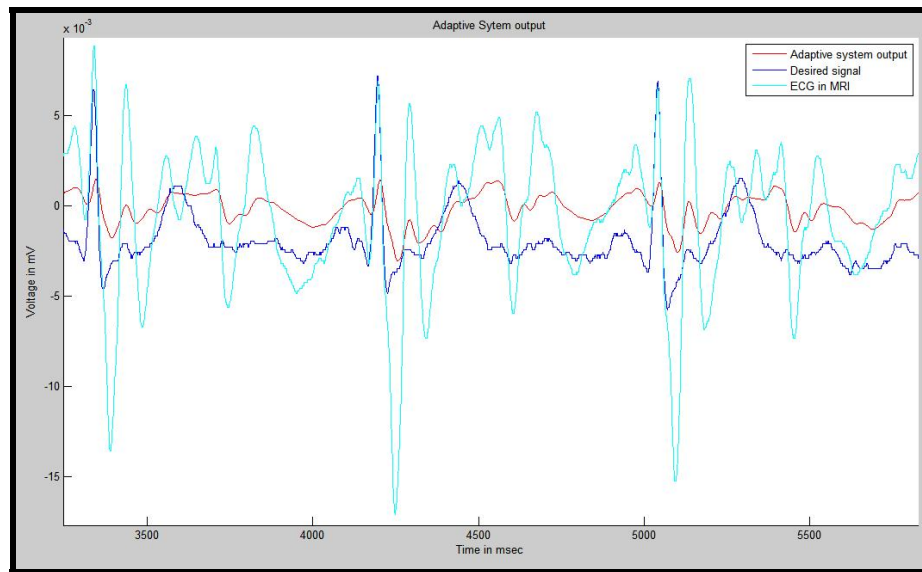


Figure 83 The ECG signal outside the MRI (desired signal), the ECG signal in the MRI and the adaptive system output.

Since the QRS peaks are detected using the QRS detector, it is easy to replace the QRS peaks of the adaptive system output with the QRS peaks from the elevated T wave ECG signal. The adaptive system output with the QRS peaks replaced is shown in Figures 84 and 85. The signals are plotted individually for clarity and then the signals are superimposed for comparison and to observe the adaptation.

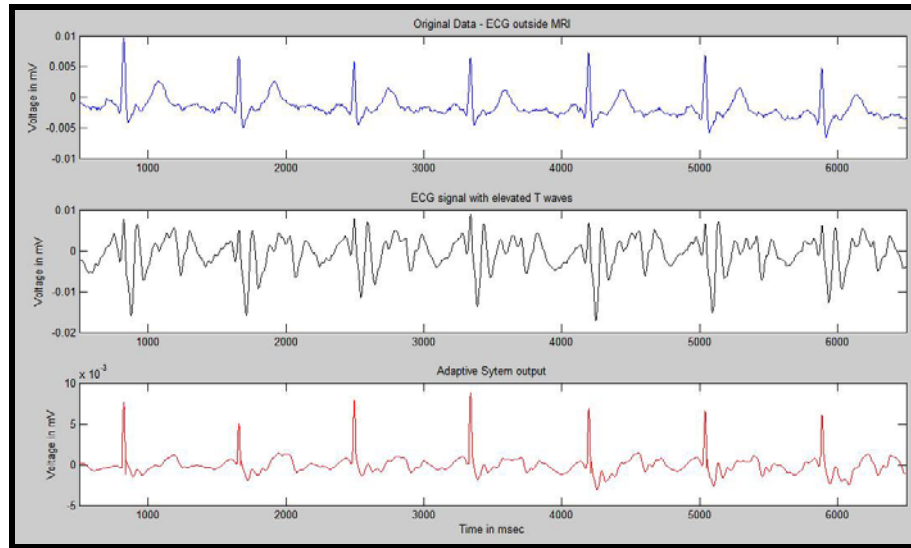


Figure 84 ECG signal outside the MRI (upper signal), ECG signal in the MRI (middle) and the adaptive system output after replacing the QRS peaks.

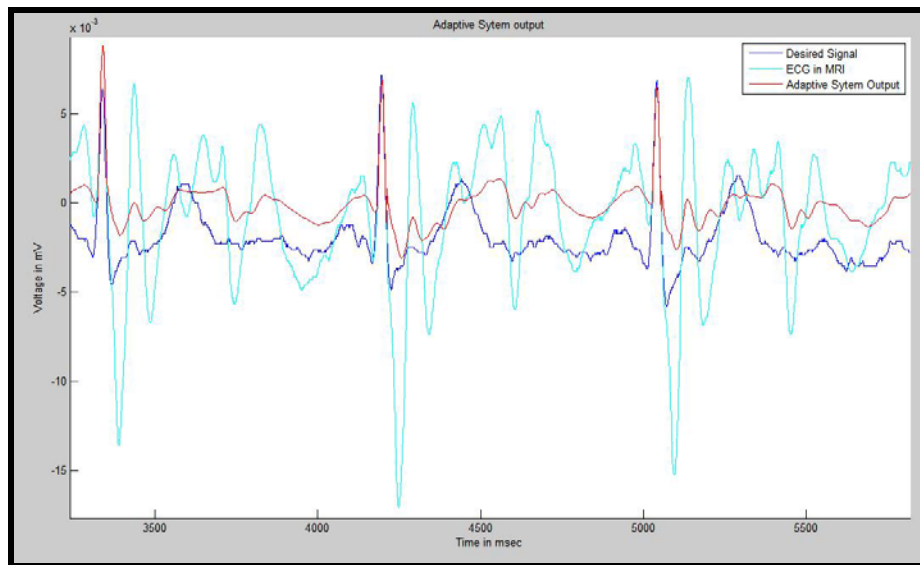


Figure 85 ECG signal outside the MRI, ECG signal in the MRI (strong negative peaks) and the adaptive system output after replacing the QRS peaks.

This weight matrix obtained from the above adaptive system is used for FIR filtering of the next few ECG cycles (new set of data – figure 87). The output of FIR system filters the magnetic induced elevation in the T wave of the ECG. As above, the QRS peaks in

the adaptive system output are replaced by the original QRS peaks. Figure 86 shows the block diagram of the entire process. Figure 87 shows the new data with the (red) stars indicating the QRS peak detection.

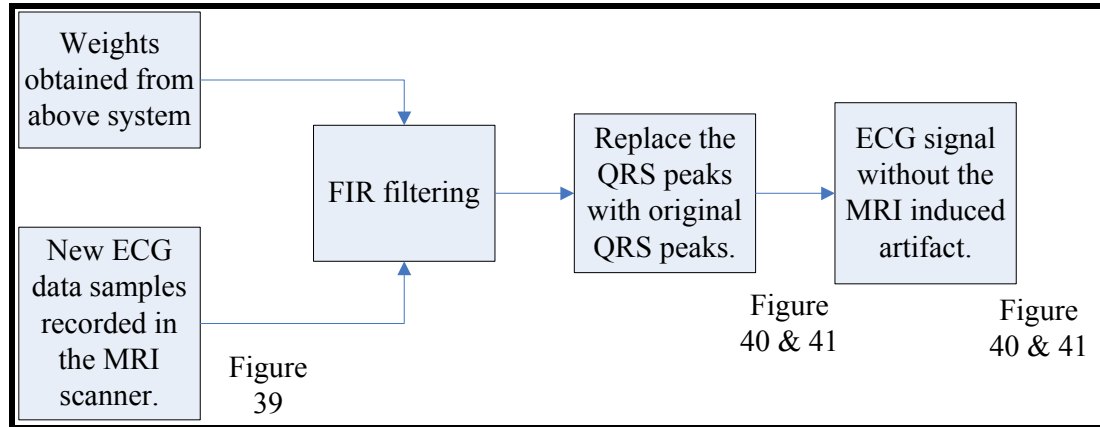


Figure 86 After obtaining the weights from the adaptive system, filtering the new data with these co-efficients.

The result of FIR filtering and replacing the QRS peaks of the adaptive system output with the original QRS peaks is shown in Figures 88 and 89. The signals are plotted individually for clarity and then the signals are superimposed for comparison and to observe the adaptation.

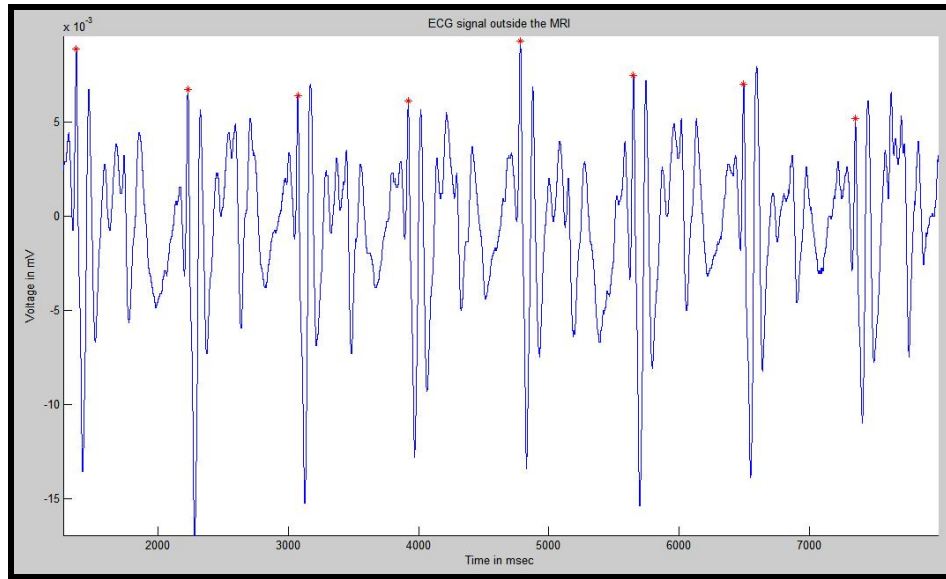


Figure 87 New data of the ECG signal inside the MRI (red peaks indicate QRS peaks)

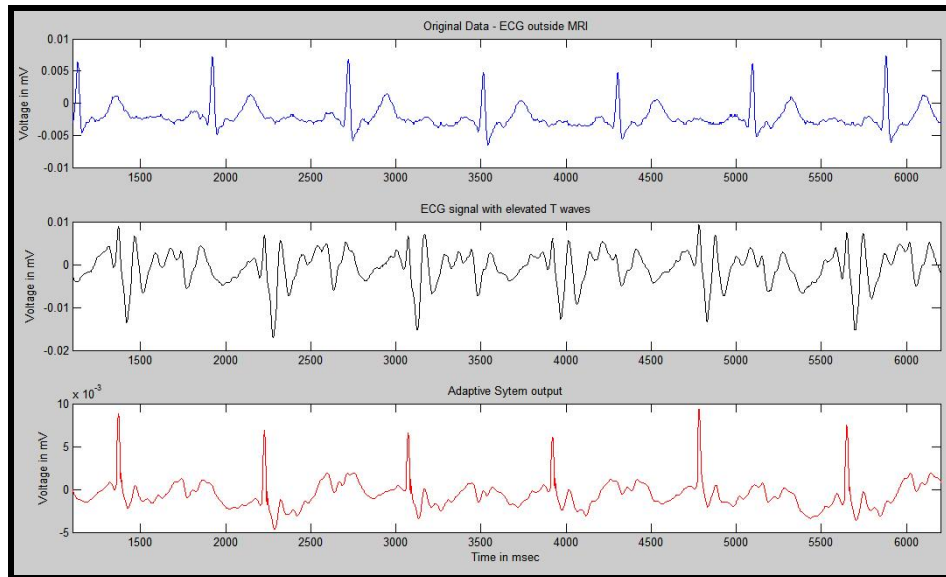


Figure 88 ECG signal outside the MRI (upper signal), ECG signal in the MRI (middle) and the adaptive system output after replacing the QRS peaks.

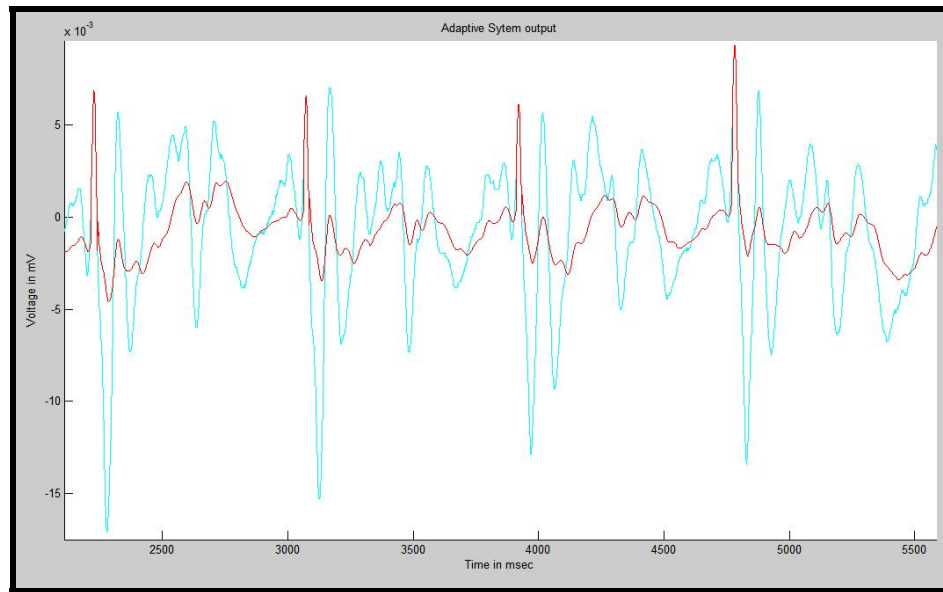


Figure 89 ECG signal in the MRI (strong negative peaks) and the adaptive system output after replacing the QRS peaks.

The results obtained by using this method on real data are extremely good. Further conclusions and discussions regarding the performance of the above system including the percentage of ST segment elevation in the ECG signals (original, elevated and filtered signals) is discussed in the next chapter.

To summarize, in this chapter first the LMS adaptive filter is implemented on noise free simulation signals and then on simulation signals with additive white Gaussian noise. In both the cases, the adaptive filter showed good results for the T wave of the ECG signal but failed to adapt to the QRS complexes. This problem was solved in the third section by implementing the adaptive filter on T waves only and computing the T wave elevation. This elevation is then subtracted from the ECG signal in the MRI to obtain artifact free ECG signals. This method showed good results as the QRS peaks were not disturbed and

the T wave adaptation had an extremely small error. This method is then tested on real data from the hospital. The method is improvised and the results are presented in the forth section of this chapter. These results obtained are extremely good and the method is more robust as compared to the method discussed in section three.

The next chapter discusses the results and conclusions of the entire research. The results from the simulation model developed and the adaptive filters are presented in greater detail. Final concluding remarks, the importance of the research and further work are also discussed as the concluding section of this dissertation.

CHAPTER 6

DISCUSSIONS AND FUTURE WORK

In this chapter, the final results and conclusions of this entire dissertation are presented. First, the results of the simulation package are compared with real data obtained from a research paper [79]. The output of the simulation package for various different input parameters is obtained. From these outputs the relation between the T wave elevation and varying magnetic field is discussed. Also the percentage increase in the T wave amplitude with a change in the maximum blood flow in the aorta is deduced from the simulation package outputs. Then the performance of the adaptive filters (fifth chapter) to filter the T wave artifact is discussed. To study the performance the slope of the line joining the S and the T point of the ECG is computed and compared for the adaptive system output, the ECG signal inside and outside the MRI. The last section of this chapter discusses the conclusions of the entire dissertation and future work.

6.1 Comparison of GUI Simulation Package with real data

The results from the simulation model are compared to a research work by Richard N Dimick, et. al.[79]. In this research paper, the 12 lead ECG is plotted for nine normal volunteers and thirteen patients in and out of a 1.5 T MRI bore. The largest artifacts are observed in the early T wave and late S-T segment of the ECG. Of the 12 leads, the maximum amplitude of the artifact is observed on leads I, II, V1 and V2 and smallest on leads III and AVF. Also low voltage, low frequency (7-10 Hz) waves are observed

throughout the cardiac cycle. The results from the simulation model are compared with these signals.

All the input parameters used in the simulation package are first discussed. The data for the blood velocity profile in the aorta is obtained from the work by Joachim Lotz, et. al.[11]. This blood velocity profile is shown in Figure 90. For the simulation, the pulse wave velocity and the differential pressure component have a constant value of 6.6 m/s and 40 mm Hg respectively. Various values of the magnetic field B ($\mu_e H_0$) are considered from 0 T to 4 T. The aorta radius has been assigned a value of 16 mm. The density of blood is between 1.05 and 1.06 g/cm³. The blood viscosity is 0.04 N.sec/m² and conductivity is 1/1.5. The Hartmann number is calculated from the values of the magnetic field, radius of aorta, the conductivity and the viscosity of blood. The model of the aorta in the simulation model is slightly rotated to align it with the position of the aorta in the patient.

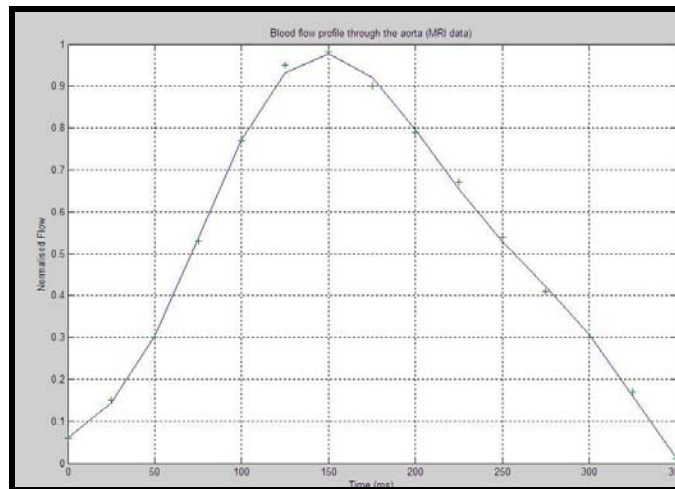
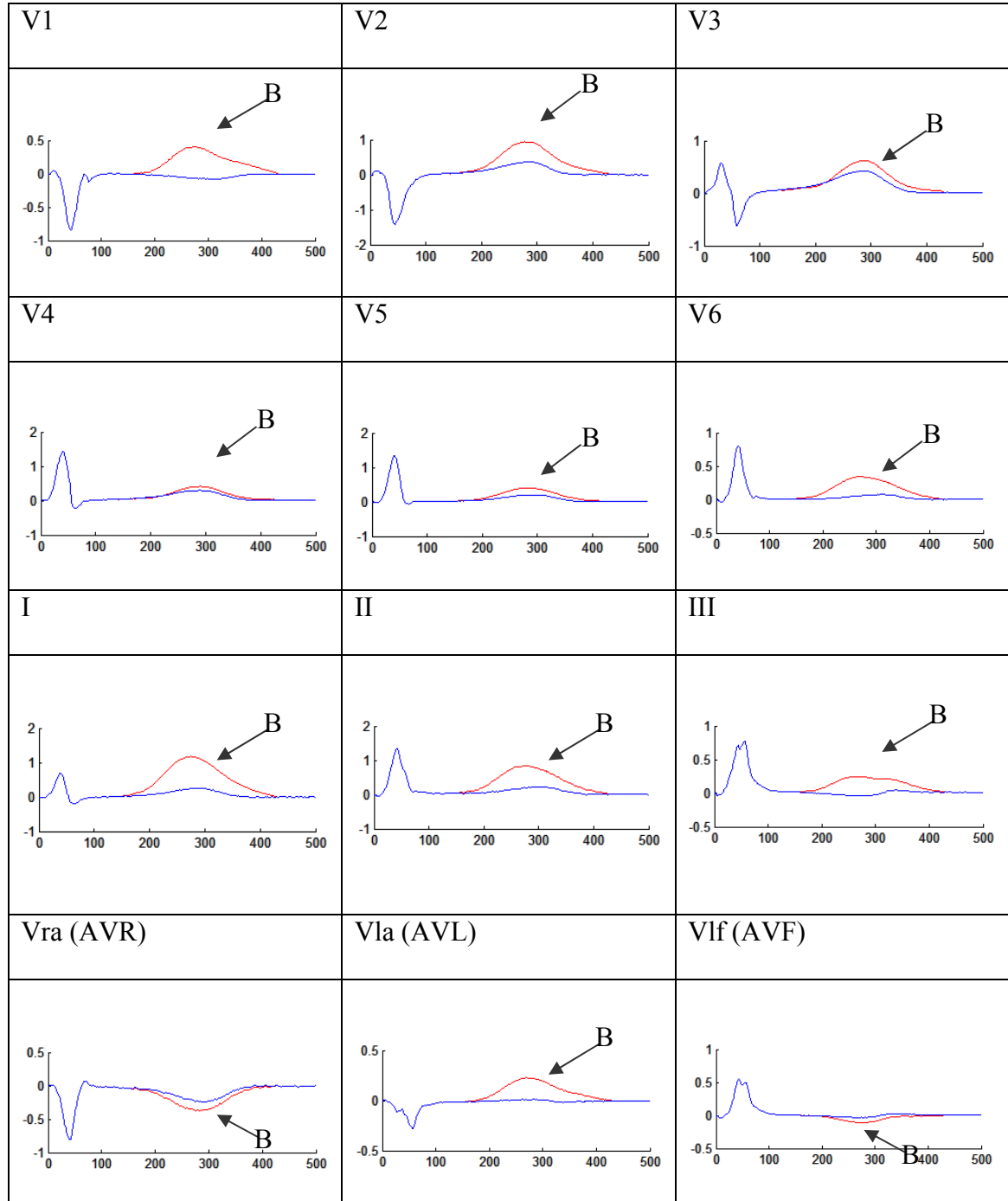


Figure 90 Blood flow profile in the aorta obtained from MRI.

After substituting these input parameters, the package computes the triangulation of the aorta, the transfer matrix and uses the MFD equations to compute the potential induced in each of the slices of the aorta. The maximum voltage is induced in the slice perpendicular to the magnetic field and decreases as the angle decreases. The results of the simulation model for the potential at the 12 leads in the presence and absence of the magnetic field of 1.5 T are shown in Table 4. The ECG signals in a magnetic field of 1.5 T are marked with 'B'. The ECG tracings from this simulation show a 310% increase in the T wave amplitude for a magnetic field of 1.5 T. at lead II. The simulation model results show a positive voltage induced in the T wave of the ECG at all the leads except AVR and AVF.

Table 4 ECG tracings at the 12 leads under normal conditions (A) compared with the tracings when subjected to 1.5 T static magnetic field (B).



There is an excellent match between the simulation and measured ECG signals at all the 12 leads. The comparison of the measured and computed ECG signals at the 12 leads is shown in Tables 5 and 6. In Table 5, the measured ECG signals for two cycles are compared with the signals from the simulation model for leads I, II, III, AVR, AVL and AVF. In each row the first signal is the ECG outside the MRI (O) and the second signal is the ECG inside the MRI (I). Table 6 shows the same comparison between the measured and simulated signals for leads V1 to V6. Table 7 compares the amplitude of induced potential at all the 12 leads for the measured and the simulation model ECG signals. Also Table 7 lists the magnitude of normal T waves, elevated T waves and the error in the induced potential between the measured and the simulation model result. The magnitude of error is extremely small (less than 0.3 mV) at all the 12 leads. Except for I, VRA, VLA and VLF, the remaining leads have an error of less than 0.1 mV. It is believed that the error is higher in these leads due to the difference between the orientation of the aorta in the simulation model and that of the patient, as discussed in the next paragraph. This shows that the simulation results are very similar to the measured ECG signals.

Table 5 Comparison of the ECG tracings measured and the tracings obtained from the simulation at leads I, II, III, AVR, AVL and AVF.

O – ECG signal outside the MRI; I – ECG signal in the MRI.

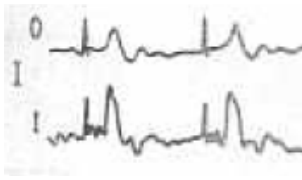
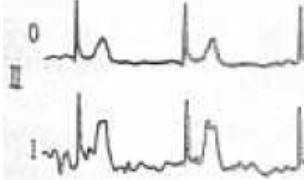
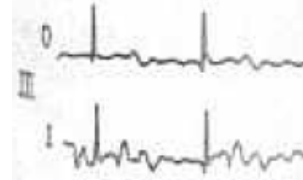
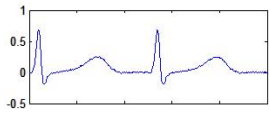
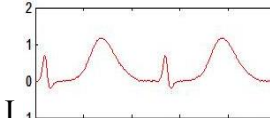
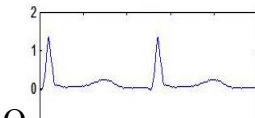
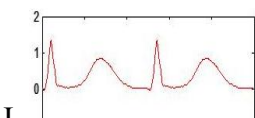
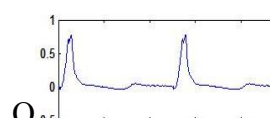
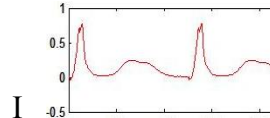
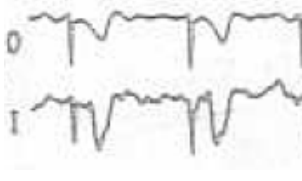
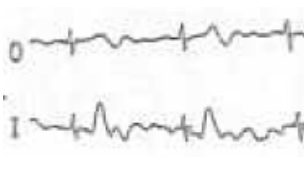
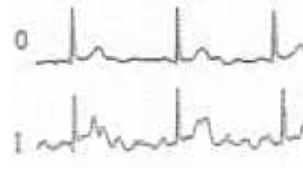
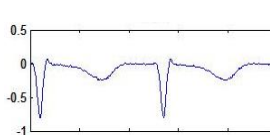
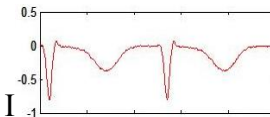
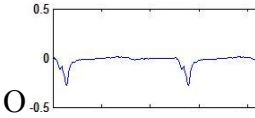
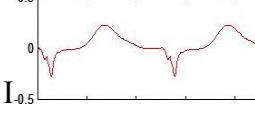
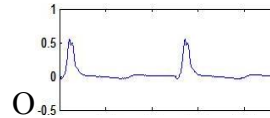
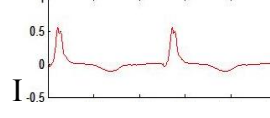
Leads	I	II	III
Measured ECG signal.			
ECG signal from simulation model.	 	 	 
Leads	AVR	AVL	AVF
Measured ECG signal.			
ECG signal from simulation model.	 	 	 

Table 6 Comparison of the ECG tracings measured and the tracings obtained from the simulation at leads V1, V2, V3, V4, V5 and V6.

O – ECG signal outside the MRI; I – ECG signal in the MRI.

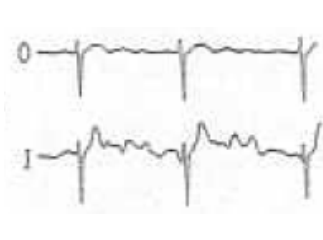
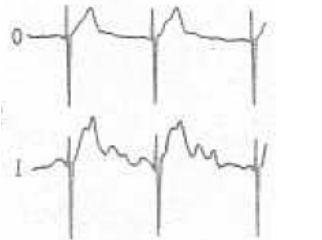
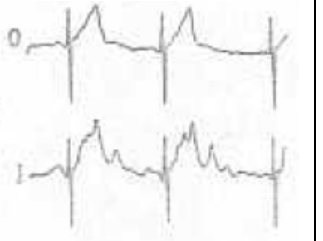
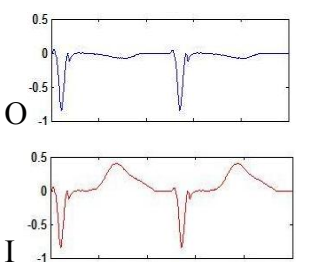
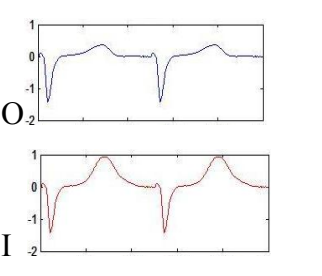
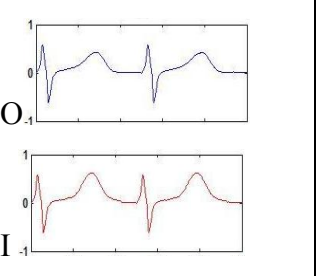



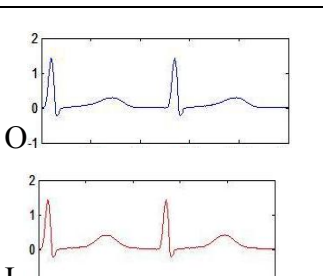
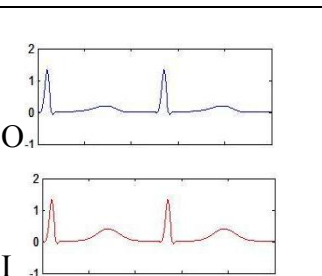
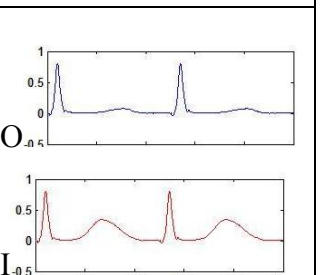
Leads	V1	V2	V3
Measur ed ECG signal.			
ECG signal from simulati on model.			
Leads	V4	V5	V6
Measur ed ECG signal.			
ECG signal from simulati on model.			

Table 7 Magnitude of the normal T wave amplitude, the T wave amplitude in a magnetic field of 1.5 T and the magnitude of induced potential at 12 leads.

Lead	T wave amplitude in a normal ECG (mV)	T wave amplitude in a ECG signal in the MRI (mV)	The induced potential = column 3 – column 2 (mV)	Induced Potential in measured data = T wave in MRI – T wave outside	Error in induced potential = simulation model – measured value (mV)
V1	-0.07405	0.4024	0.47645	$0.5 - 0.1 = 0.4$	0.07645
V2	0.3588	0.9413	0.5825	$1 - 0.5 = 0.5$	0.0825
V3	0.4213	0.6179	0.1966	$0.8 - 0.6 = 0.2$	-0.0034
V4	0.3002	0.4043	0.1041	$1 - 0.9 = 0.1$	0.0041
V5	0.1958	0.393	0.1972	$0.8 - 0.7 = 0.1$	0.0972
V6	0.06271	0.3405	0.27779	$0.8 - 0.5 = 0.3$	-0.0222
VRA	-0.2402	-0.3641	-0.1239	$-1 - (-0.5) = -0.5$	0.3761
VLA	0.01199	0.2207	0.20871	$0.5 - 0.1 = 0.4$	-0.1913
VLF	-0.03134	-0.109	-0.07766	$0.3 - 0.2 = 0.1$	-0.1777
I	0.2388	1.178	0.9392	$1 - 0.3 = 0.7$	0.2392
II	0.2021	0.8505	0.6484	$1 - 0.4 = 0.6$	0.0484
III	-0.011	0.2109	0.2219	$0.3 - 0.1 = 0.2$	0.0219

In our simulation, the largest amplitude of the induced potential is observed in I, II, V1 and V2 and the smallest amplitude is observed in AVF (Table 7). From this, it can be inferred that the vector of the maximum potential is in the direction left inferior (maximum at leads I and II) and anterior from the center of the chest (maximum at V1 and V2). At lead I the amplitude of the induced potential is more than the QRS peak. The position of the aorta is not parallel to the thorax but originates from the aortic valve and arches posterior as seen in Figure 91.

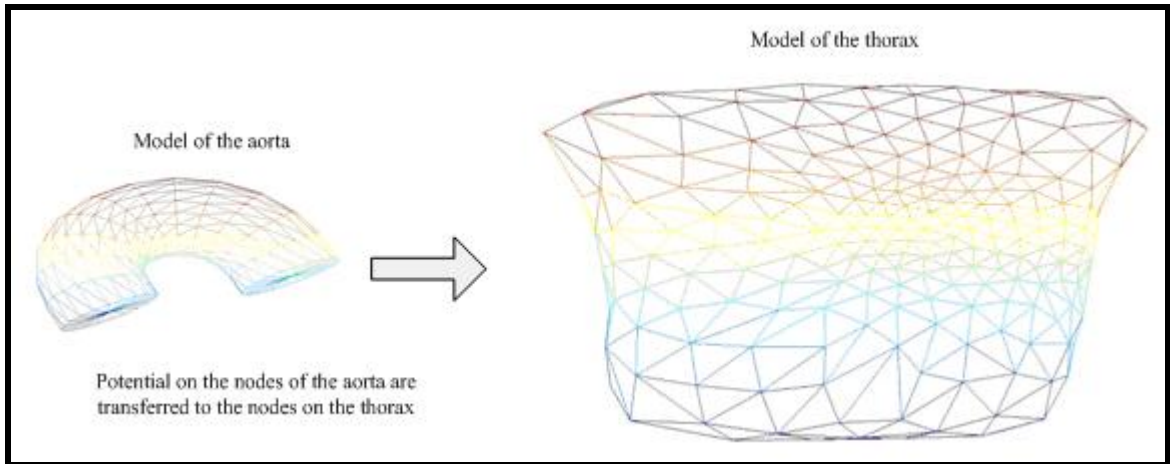


Figure 91 The model of the aorta and the thorax.

Hence, the obtained results are in accordance with the right hand rule that the maximum potential is induced when the flow of blood is perpendicular to the magnetic field. Figure 92 shows the region of the aorta where the maximum (left superior part of the aortic arch) and minimum potential (right inferior) is induced. Darker regions show higher positive or negative voltage induced and lighter regions show a decrease in induced potential as the angle between the flow of blood and the magnetic field decreases.

The next section describes the relationship between the T wave elevation and the magnetic field strength. Also the change in the elevation with a change in the cardiac output is discussed.

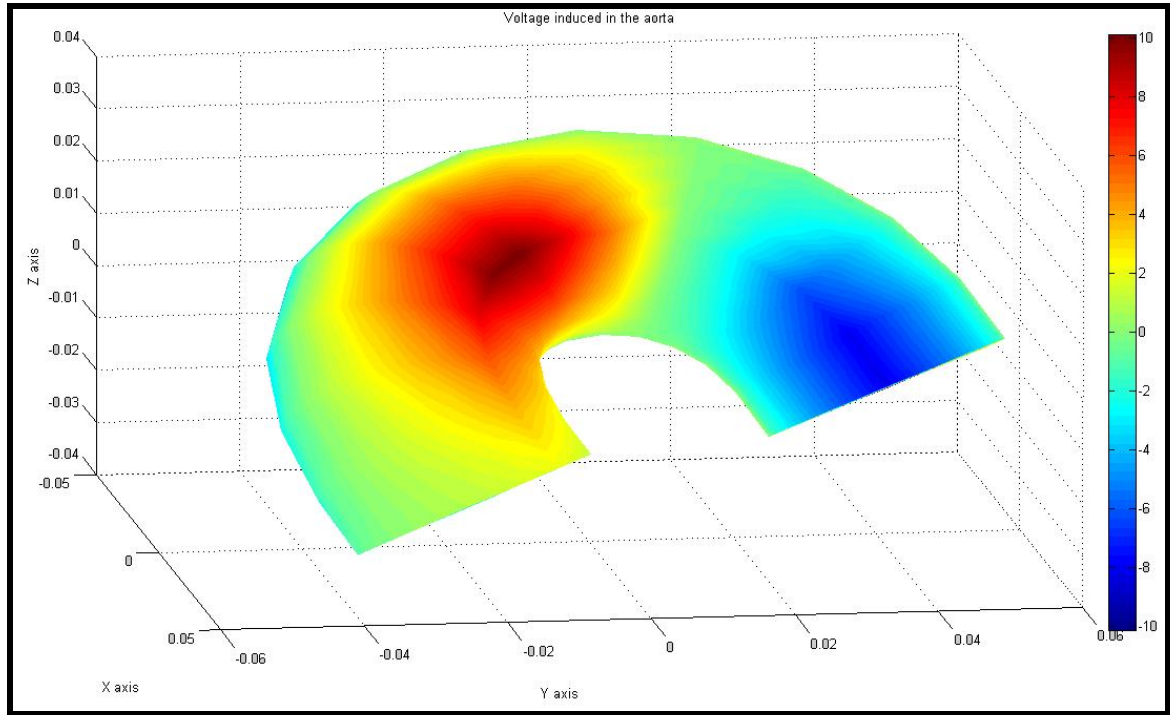


Figure 92 Distribution of potential induced on the surface of the aorta.

6.2 Relation between T wave elevation and the magnetic field

The relation between the changes in T wave amplitude with the change in magnetic field is analyzed by changing the magnetic field magnitude and running the GUI simulation package. The results at lead II for magnetic fields varying from 0 to 4 T are shown in Figure 94. The magnitude of T wave elevation and the percentage increase with changing magnetic field are tabulated in Table 8.

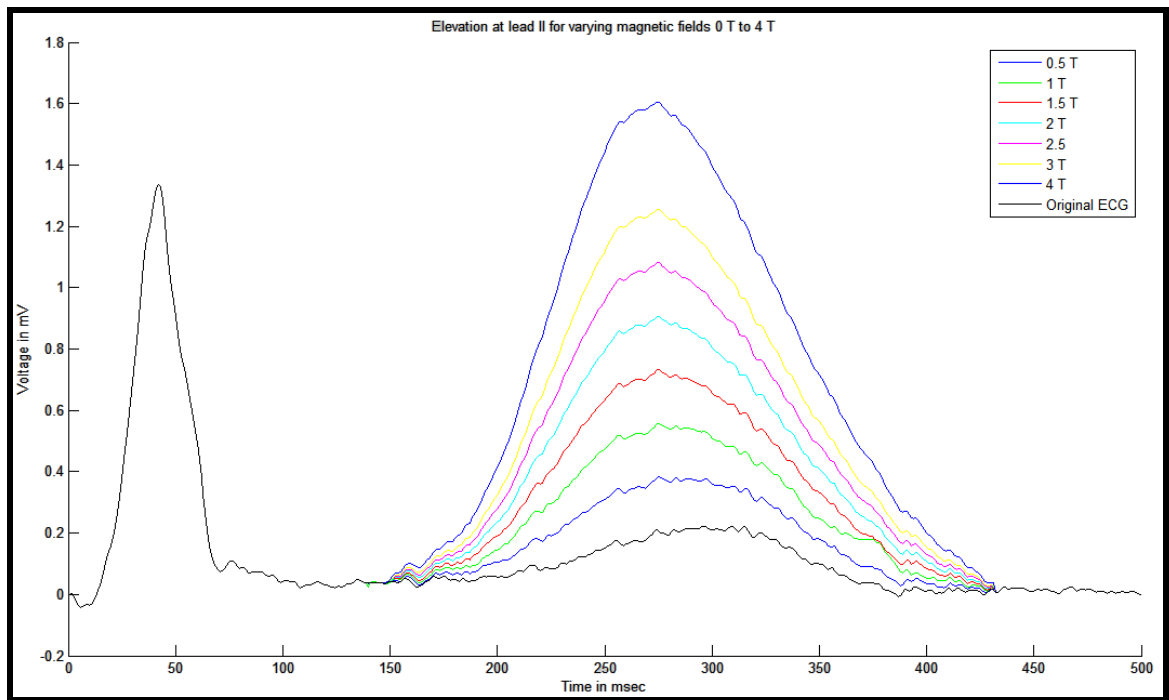
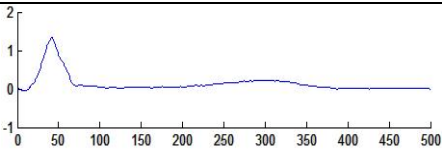
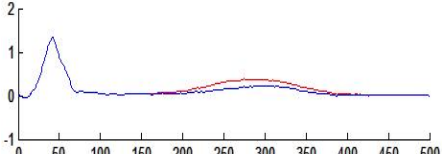
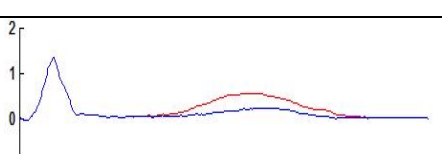
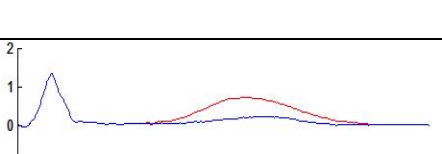
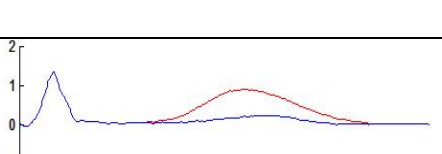
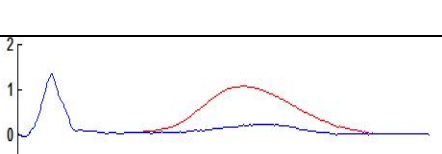


Figure 93 ECG at lead II showing the T wave amplitude for varying magnetic fields 0 T to 4 T.

Table 8 T wave elevation at lead II for varying magnetic fields (0 to 4 T). Table also shows percentage increase in T wave amplitude.

Magnetic Field	Elevation in the T wave – lead II	T wave amplitude mV	Increase in T wave amplitude %
0 T		0.2074	0
0.5 T		0.3841	85.198
1 T		0.5569	168.51
1.5 T		0.8505	310.07
2 T		0.9076	337.60
2.5 T		1.082	421.697

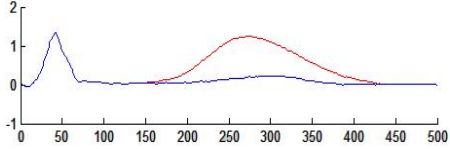
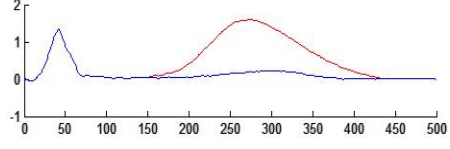
3 T		1.256	505.59
4 T		1.605	673.86

Figure 95 shows the percentage increase in T wave amplitude with varying magnetic fields. The plot clearly reveals a linear relationship. The ECG tracings from this simulation show a 310% (Table 5) increase in the T wave amplitude for a magnetic field of 1.5 T. at lead II. In an experiment on Macaca monkeys [3], a 300 % increase in T wave amplitude is obtained for a magnetic field of 1.52 T. Hence, the simulation results at all the 12 leads and the percentage increase for varying magnetic fields yield very similar results. The next section discusses the relation between the T wave elevation and the cardiac output.

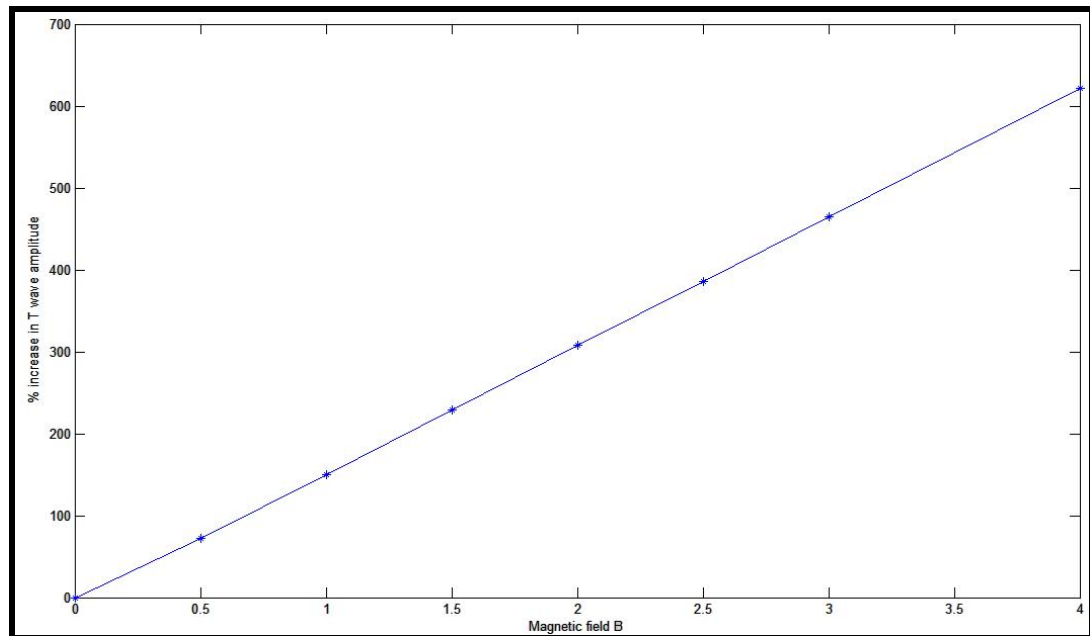


Figure 94 Plot of percentage increase in T wave amplitude with varying magnetic field (0 to 4 T).

6.3 Relation between T wave elevation and cardiac output

In the simulation package, the induced T wave is computed for various cardiac outputs. This is done by changing the aorta blood flow data file and running the simulation package. The peak blood flow velocity in the aorta is changed from 200 ml/sec to 600 ml/sec and the induced voltage is determined for each case. The peak blood flow in the aorta of a normal human is 400 ml/sec. Figure 96 shows the T wave induced potential for different cardiac outputs. Figure 97 shows the percentage increase in T wave amplitude with varying blood velocities in the aorta. The relation is clearly linear.

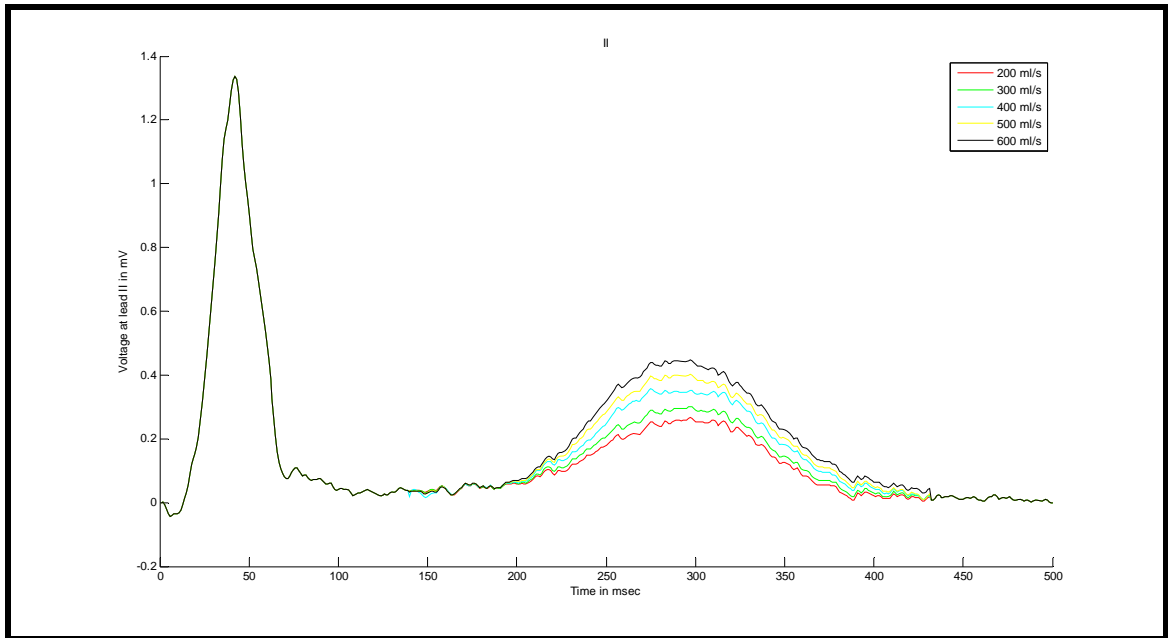


Figure 95 Elevation of the T wave for various different cardiac outputs.

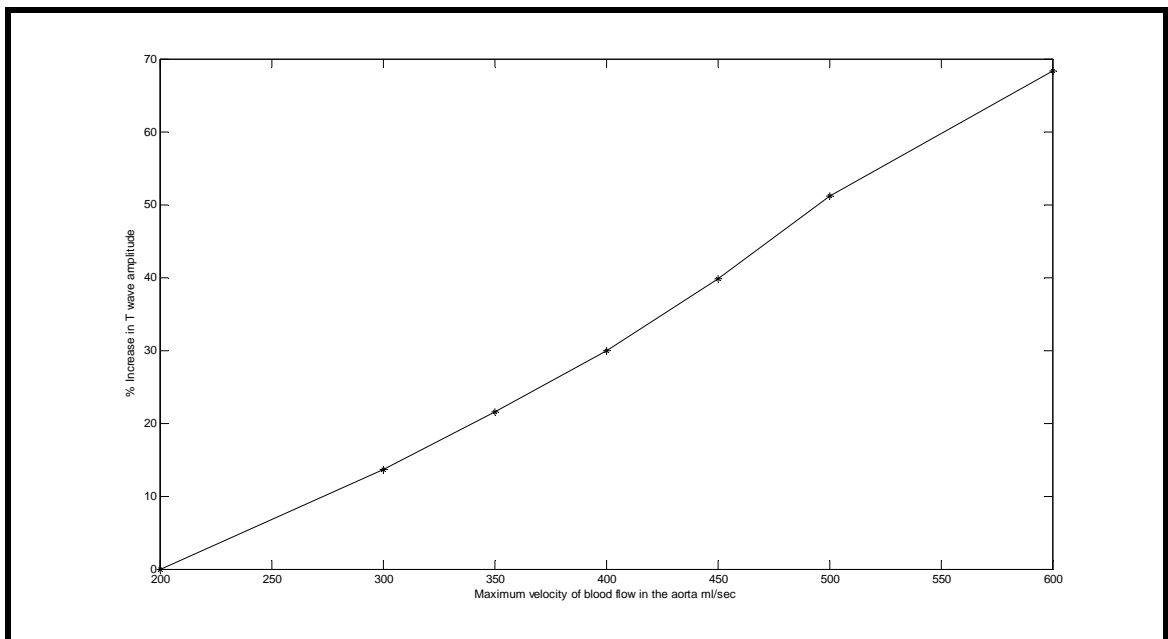


Figure 96 Percentage increase in the T wave with varying cardiac output.

An important result from this figure is that there is an increase of 17.08% or 0.0454 mV in the induced T wave amplitude for every 100 ml increase in the peak blood flow in the aorta. This result can be incorporated in the linear adaptive systems so that for any change in blood flow in the aorta the T wave amplitude can be correspondingly updated. In the next section the results of filtering the T wave artifact using adaptive LMS filter is discussed.

6.4 Results from the adaptive system

In the last section of the previous chapter, the adaptive system is implemented on real data after heart rate matching using interpolation or decimation. After training the weights of the adaptive system, the FIR filter with these weights is used to filter the T wave artifact. The output plots were discussed in the previous chapter. The magnitude and phase response of the FIR filter is plotted in Figure 98. The magnitude response shows that the filter suppresses the frequency corresponding to the T wave elevation by -18 dB.

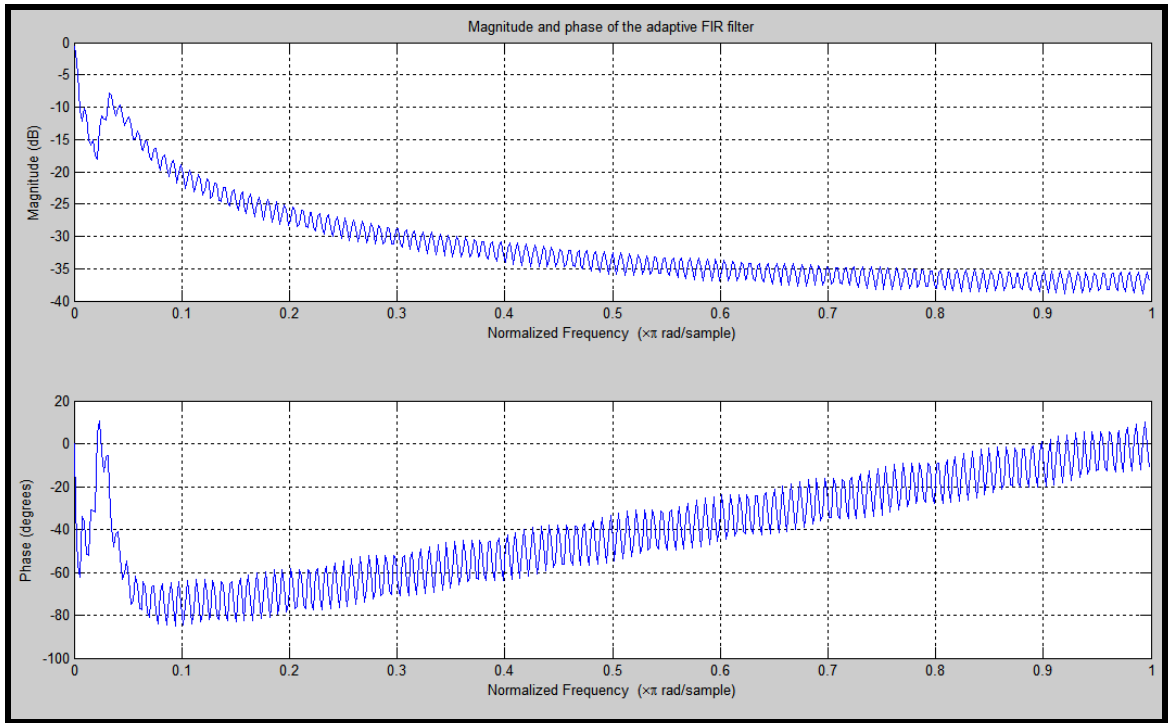


Figure 97 Magnitude and phase of the adaptive FIR filter.



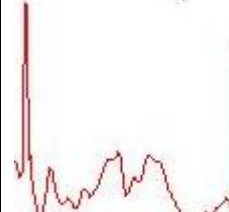
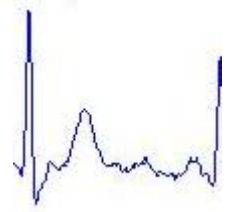




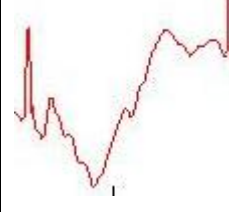
To further look into the performance of the adaptive system, the ST segment slope is computed for a single heart beat for the ECG signal outside the MRI, in the MRI and the adaptive system output. The closer the slope of the ST segment of the adaptive system to the ECG signal outside the MRI, better is the performance of the system. The slope of the ST segment of the signals is tabulated in Table 9. The slope of the ST segment of the adaptive system may vary slightly from the ECG signal outside the MRI as the ECG signals in and outside the MRI are measured at different time instants. Table 9 shows that the adaptive filter is successful in removing the T wave artifact as the ST segment slope reduces from an average value of 6.5 to 1.7.

Table 9 The slope of the line joining the ST segment measured at different points of the measured ECG signals

Data Sample number in the ECG signal	Slope of ST segment of ECG outside the MRI	Slope of ST segment of ECG from adaptive system output	Slope of ST segment of ECG inside the MRI
3200	2.92	1.01	6.79
16000	3.42	1.85	6.8
36000	3.32	1.83	5.24
13000	2.89	2.09	7.97
32000	3.303	1.8	5.88

The ECG signal in the MRI, outside the MRI and adaptive system output are plotted for individual ECG cycles in Table 10. This further shows the performance of the adaptive system. The ECG signal measured in the MRI in the third row of the table is distorted due to a change of the patient physiology. The adaptive system output (third row) maintains the shape to show the change in patient physiology but with reduced T wave amplitude. Hence the adaptive system reduces the T wave amplitude but maintains the characteristics of the ECG signal.

Table 10 The performance of the adaptive system – the ECG signal outside the MRI, the ECG signal in the MRI and the adaptive system output.

ECG signal outside the MRI	ECG signal in the MRI	Adaptive System Output
		
		
		

6.5 Future Work

The simulation package developed has been successfully tested for human physiological signals obtained from different research papers. The simulation package worked successfully on these signals. But the package has not been tested in real time. The next step would be to test the package when the patient is in the MRI. The input parameters – the radius of the aorta and the orientation of the aorta with respect to the heart can be fed into the package. From this the transfer matrix can be determined. The patient PPG waveform and the ECG signal in the MRI can be measured real time and fed into the

package. The package computes the pulse wave velocity real time and uses this value in magneto-hydro-dynamic equations to compute the potential induced in the aorta. This value is then transferred to the thorax to determine the T wave elevation. The final output of the package can be tested to determine the performance of the entire package real time.

The adaptive LMS filter is implemented on ECG data and the results show that the T wave artifacts can be reduced to match the non-MRI ECG signals. The next step would be to implement this entire software code on a DSP processor and introduce this as a module in the MRI compatible ECG monitors. An interesting challenge is that the final device should be MRI compatible, compact and should not introduce any new artifacts. The success of this device will assist the doctors to analyze and diagnose the physiology of the patients in the MRI.

6.6 Conclusion

In this dissertation two approaches are presented to solve the problem of T wave elevation of the ECG signal when the patient is subjected to a static magnetic field of the MRI. The solution to this problem is researched from a mathematical approach based on modeling of the aorta and thorax and from a signal processing perspective.

A GUI simulation package is developed to compute the T wave elevation of the ECG signal using magneto-hydro-dynamic equations. The simulation package uses a model of the heart, aorta and thorax and computes the potential induced in the aorta and then

transfers this potential to the thorax considering the conductivity of the tissues and organs between the aorta and the thorax. This package needs the PPG waveform obtained from a pulse oximeter in addition to the ECG signal in the MRI. It has the provision to change the radius and the orientation of the aorta with respect to the heart. The package developed is successfully tested by using simulated signals and human physiology signals obtained from various research papers.

The second approach is based on digital signal processing where the T wave artifact is filtered by using an adaptive LMS filter. This approach requires the ECG of the patient outside the MRI as a desired response and the ECG in the MRI as the input to the LMS filter. The heart rate of the two ECG signals is first synchronized and then used as inputs to the LMS filters. The output from this approach successfully filters out a majority of the T wave artifact, to obtain ECG signals free of the T wave elevation.

With the extensive use of MRI and the vital information in the ECG signal, it is important to have artifact free ECG of the patient in the MRI room. This entire research works towards obtaining artifact free ECG signals in the MRI. The research work in this area is unique and the results obtained can be tested on hardware to obtain artifact free ECG signals. This research is a major step in solving this problem and the results obtained will assist doctors to diagnose the patients in the MRI.

LIST OF REFERENCES

1. Thomas S. Tenforde, "Magnetically induced electric fields and currents in the circulatory system," *Progress in Biophysics and molecular Biology*, vol. 87, pp. 279-288, 2005.
2. Frans Van de Werf, "Management of acute myocardial infarction in patients presenting with ST-segment elevation," *European Heart Journal*, vol. 24, no. 1, pp. 28-66, 2003.
3. T. S. Tenforde, C. T. Gaffey, B. R. Moyer, and T. F. Budinger, "Cardiovascular Alterations in Macaca monkeys exposed to stationary magnetic fields," *Bioelectromagnetics*, vol. 4, pp. 1-9, 1983.
4. Lionel H Opie, *Heart Physiology: from cell to circulation – fourth edition*. Philadelphia: Lippincott Williams and Wilkins Publications, 2004
5. J.R.Levick, *An introduction to cardiovascular physiology*. London: Butterworth-Heinemann Publications, 1991.
6. Mary Boudreau Conover, *Understanding Electrocardiography - Seventh Edition*. Missouri: Mosby Publications, 1996.
7. Frank G. Yanowitz, Professor of Medicine, University of Utah School of Medicine, "The Alan E. Lindsay ECG Learning Center in Cyberspace," 2006, <http://library.med.utah.edu/kw/ecg/index.html>.
8. Richard P. Wayne (wayne@physchem.ox.ac.uk), "Elementary ECG", <http://physchem.ox.ac.uk/~wayne/ECG%20etc/Elementary%20ECG%20%28aka%20Electrocardiogram%20or%20EKG%29.htm>.

9. Zhi.-Pei Liang, and Paul C. Lauterbur, *Principles of magnetic resonance imaging: A signal processing perspective*. IEEE Press series in biomedical engineering, 2000.
10. Joseph P. Hornak, Rochester Institute of Technology, “The basics of MRI” <http://www.cis.rit.edu/htbooks/mri/inside.htm>.
11. Joachim Lotz, Christian Meier, Andreas Leppert, and Michael Galanski, “Cardiovascular flow measurement with phase contrast MR Imaging,” *RadioGraphics*, vol. 22, pp. 651-671, 2002.
12. Samuel Seely and Alexander D Poularikas, *Electromagnetics – Classical and Modern Theory and Applications*. New York and Basel: Marcel Dekker, Inc. Publications, 1979.
13. Anne M. R. Agur and Ming J. Lee, *Grant’s Atlas of Anatomy - Tenth Edition*. Philadelphia: Lippincott William and Wilkins Publications, 1999.
14. Beischer D. E., and Knepton J. C. Jr., “Influence of strong magnetic fields on the electrocardiogram of squirrel monkeys,” *Aerospace Medicine*, vol. 35, pp. 939-944, 1964.
15. John K-J. Li, *The Arterial circulation- physical principles and clinical applications*. New Jersey: Humana Press, 2000.
16. K. H. Wesseling, J. R. C. Jansen, J. J. Settels and J. J. Schreuder, “Computation of aortic flow from pressure in humans using a nonlinear, three-element model,” *Journal of Applied Physiology*, vol. 74(5), pp. 2566-2573, 1993.

17. Brian Gribbin, Andrew Steptoe and Peter Sleight, "Pulse Wave Velocity as a Measure of Blood Pressure Change," *Psychophysiology*, vol. 13(1), pp. 86-90, January 1976.
18. Kenneth R. Cramer and Shih-I Pai, *Magnetofluid Dynamics for Engineers and Applied Physicists*. Washington, D.C.: Scripta Publishing Company, McGraw-Hill Book Company 1973.
19. Richard R. Gold, "Magnetohydrodynamic pipe flow - Part 1," *Journal of Fluid Mechanics*, vol. 13, issue 04, pp. 505-512, August 1962.
20. J. Hartmann and F. Lazarus, "Hg-Dynamics I," *Math.-fys. Medd.*, vol. 15, no. 7, 1937.
21. J. A. Shercliff, "Steady motion of conducting fluids in pipes under transverse magnetic fields," *Proceedings of the Cambridge Philosophical Society*, vol. 49, pp. 136-144, 1953.
22. J. A. Shercliff, "The flow of conducting fluids in circular pipes under transverse magnetic fields," *Journal of Fluid Mechanics*, vol. 1, pp. 644-666, 1956.
23. P. A. Davidson, *An Introduction to Magnetohydrodynamics*. Cambridge Texts in Applied Mathematics – Cambridge University Press, 2001.
24. American Society of Mechanical Engineers Fluids Engineering Division, *Biomedical Fluid Mechanics Symposium*. Presented at Fluids Engineering Conference, Denver, Colorado, 1966.
25. M. Jermy, *Fluid Mechanics - A Course Reader*. Mechanical Engineering Department, University of Canterbury, 2005.
26. Amal Jubran, "Pulse Oximetry," *Critical Care*, vol. 3, pp. R11-R17, 1999.

27. James E. Sinex, "Pulse Oximetry: Principles and Limitations," *American Journal of Emergency Medicine*, vol. 17, number 1, January 1999.
28. Invivo Research 4500 Pulse Oximeters: http://used-medical-equipment.medical-supplies-equipment-company.com/product/PPF/ID/13421/new_prod_full.asp.
29. M. Shamir, L. A. Eidelman, Y. Floman, L. Kaplan and R. Pizov, "Pulse oximetry plethysmographic waveform during changes in blood volume," *British Journal of Anaesthesia*, vol. 82(2), pp. 178-181, 1999.
30. Kathleen Wilkie, "Human Blood Flow measurement and modeling," Report 98181130.
31. David N. Ku, "Blood flow in arteries," *Annual Review of Fluid Mechanics*, vol. 29, pp. 399-434, 1997.
32. F. M. Liebman, J. Pearl and S. Bagno, "The electrical conductance properties of blood in motion," College of Dentistry and the Murry and Leonie Guggenheim Foundation Institute for Dental Research, Department of physiology, New York University.
33. E. Sigman, A. Kolin, and L. Katz, "Effect of motion on the electrical conductivity of the blood," *American Journal of Physiology*, vol. 118, pp. 708-719, 1937.
34. Yu. E. Moskalenko, and A. I. Naumenko, "Movement of the blood and changes in its electrical conductivity," *Bulletin of experimental Biology and Medicine*, vol. 47, pp. 211-215, 1959.

35. F. M. Liebman and F. Cosenza, "Study of blood flow in the dental pulp by an electrical impedance technique," *Physics in medicine and Biology*, vol. 7, number 2, pp. 167-176, 1962.
36. Y. C. Fung, *Biomechanics – Motion, flow, stress and growth*. New York: Springer Verlag Publications, 1990.
37. A. Landias, J. P. Morin, A. Roche, C. Cornec, and N. Sansoy, "Measurement of cardiac output by the thermodilution method during left thoracotomy in the lateral position in the dog," *Acta Anaesthesiologica Scandinavica*, vol. 34, pp. 158-161, 1990.
38. David H. Evans, and W. Norman McDicken, *Doppler Ultrasound –physics, instrumentation and signal processing*. Chichester, New York: John Wiley Publications, May 2000.
39. N. A. Wisely and L. B. Cook, "Arterial flow waveforms from pulse oximetry compared with measured Doppler flow waveforms," *Anaesthesia*, vol. 56, issue 6, pp. 556, June 2001.
40. L. B. Cook, "Extracting arterial flow waveforms from pulse oximeter waveforms," *Anaesthesia*, vol. 56, issue 6, pp. 551, June 2001.
41. George Rudinger, "Review of current mathematical methods for the analysis of blood flow," *Cornell Aeronautical Laboratory, Buffalo, New York*.
42. Howard L Golub, "Method and apparatus for non-invasive, cuffless, continuous blood pressure determination," U. S. Patent 5,865,755, February 1999.
43. L. A. Geddes, M. H. Voelz, C. F. Babbs, J. D. Bourland, and W. A. Tacker, "Pulse Transit Time as an Indicator of Arterial Blood Pressure," *Psychophysiology*, vol. 18, issue 1, pp. 71, January 1981.

44. Andrew Steptoe, Harold Smulyan, and Brian Gribbin, "Pulse Wave Velocity and Blood Pressure Change: Calibration and Applications," *Psychophysiology*, vol. 13, issue 5, pp. 488, 1976.
45. Alfredo L. Pauca, Michael F. O'Rourke, and Neal D. Kon, "Prospective Evaluation of a Method for estimating Ascending Aortic Pressure from the Radial Artery Pressure waveform," *American Heart Association – Hypertension*, vol. 38, pp. 932-937, 2001.
46. Mustafa Karamanoglu and Michael P. Fenely, "On-line Synthesis of the Human Ascending Aortic Pressure Pulse from the finger pulse," *American Heart Association – Hypertension*, vol. 30, pp. 1416-1424, 1997.
47. Willem Jan W. Bos, Jeroen van Goudoever, Gert A. van Montfrans, Anton H. van den Meiracker, and Karel H. Wesseling, "Reconstruction of Brachial artery pressure from non invasive finger pressure measurements," *American Heart Association – Circulation*, vol. 94, pp. 1870-1875, 1996.
48. Ante Santic and Miroslav Saban, "Two methods for determination of diastolic and systolic pressures in fingers," in *Proceedings of the 17th Annual International Conference of the IEEE Engineering in Medicine and Biology Society*, September 1995, 20-25, vol. 1, pp. 149-150.
49. P. Shaltis, A. Reisner, and H. Asada, "Calibration of the photoplethysmogram to arterial blood pressure: capabilities and limitations for continuous pressure monitoring," in *Proceedings of the 27th Annual International Conference of the IEEE Engineering in Medicine and Biology Society*, 2005, pp. 3970-3973.

50. Teng X. F. and Zhang Y. T., "Continuous and noninvasive estimation of arterial blood pressure using a photoplethysmographic approach," in *Proceedings of the 25th Annual International Conference of the IEEE Engineering in Medicine and Biology Society*, 2003, 17-21, vol. 4, pp. 17-21.
51. John Allen and Alan Murray, "Modeling the relationship between peripheral blood pressure and blood volume pulses using linear and neural network system identification techniques," *Physiological Measurement*, vol. 20, pp. 287-301, 1999.
52. D. McAuley, B. Silke, and S. Farrell, "Reliability of blood pressure determination with the Finapres with altered physiological states or pharmacodynamic conditions," *Clinical Autonomic Research*, vol. 7, number 4, August 1997.
53. V. A. Vardanyan, "Effect of magnetic field on blood flow," *Biofizika*, vol. 18, number 3, pp. 491-496, 1973.
54. E. M. Korchevskii and L. S. Marochnik, "Magnetohydrodynamic version of movement of blood," *Biofizika*, vol. 10, number 2, pp. 371-373, 1965.
55. Y. Kinouchi, H. Yamaguchi and T. S. Tenforde, "Theoretical Analysis of Magnetic Field Interactions with Aortic Blood Flow," *Bioelectromagnetics*, vol. 17, pp. 21-32, 1996.
56. T. Togawa, O. Okai and M. Oshima, "Observation of blood flow EMF in externally applied strong magnetic field by surface electrodes," *Medical and Biological Engineering*, vol. 5, pp. 169-170, 1967.
57. C. T. Gaffey, T. S. Tenforde, and E. E. Dean, "Alterations in the electrocardiograms of baboons exposed to DC magnetic fields," *Bioelectromagnetics*, vol. 1, pp. 209, 1980.

58. M. Sermesant, H. Delingette and N. Ayache, "An Electromechanical Model of the Heart for Image Analysis and Simulation," *IEEE Transactions on Medical Imaging*, vol. 25, issue 5, pp. 612-625, May 2006.
59. M. Sermesant, Y. Coudiere, H. Delingette, N. Ayache, J. Sainte-Marie, D. Chapelle, F. Clement, and M. Sorine, "Progress towards model based estimation of the cardiac electromechanical activity from ECG signals and 4D images," *European Series in Applied and Industrial Mathematics (ESAIM) Proceedings*, vol. 12, pp. 153-162, November 2002.
60. M. Sermesant, O. Faris, F. Evans, E. MsVeigh, Y. Coudiere, H. Delingette, and N. Ayache, "Preliminary validation using in vivo measures of a macroscopic electrical model of the heart," in *International Symposium on surgery simulation and soft tissue modeling (IS4TM'03)*, 2003.
61. Gunnar Seemann, Christian D. Werner, Frank B. Sachse and Olaf Dossel, "Simulation of the cardiac electrical activity: interactive user interface to control the simulation process," *Institute of Biomedical Engineering, University of Karlsruhe, Germany*.
62. Adriaan Van Oosterom and Geertjan Huiskamp, "The depolarization sequence of the human heart surface computed from measured body surface potentials," *IEEE Transactions on biomedical engineering*, vol. 35, number 12, pp. 1047-1058, December 1988.
63. Adriaan Van Oosterom, "Genesis of the T wave as based on an equivalent surface source model," *Journal of Electrocardiology*, vol. 34S, pp. 217-226, 2001.

64. Adriaan Van Oosterom, "Interactive Simulation of QRS waveforms," in *Proceedings of the 11th Annual International Conference of the IEEE Engineering in Medicine and Biology Society*, 1989, pp.183-184.
65. C. T. Gaffey and T. S. Tenforde, "Alterations in the rat electrocardiogram induced by stationary magnetic fields," *Bioelectromagnetics*, vol. 2, pp. 357-370, 1981.
66. C. T. Gaffey and T. S. Tenforde, "Changes in the electrocardiograms of rats and dogs exposed to DC magnetic fields," University of California, Berkeley, California, Lawrence Berkeley Laboratory Report No. 9085, 1979.
67. MEET Man Project:
http://www-ibt.etec.uni-karlsruhe.de/forschung/meetman/meetmanmenue_en.htm.
68. Frank G. Shellock, Henriette Lipczak, and Emanuel Kanal, "Monitoring patients during MR procedures: A review," *Applied Radiology*, pp. 11-17, February 1995.
69. Richard E. Wendt III, Roxann Rokey, G. Wesley Vick III and Donald L. Johnston, "Electrocardiographic gating and monitoring in NMR imaging," *Magnetic Resonance Imaging*, vol. 6, pp. 89-95, 1988.
70. Hideki Fujiko and Kazuo Tanishita, "Computational fluid mechanics of the blood flow in an aortic vessel with realistic geometry," in *Clinical Application of Computational Mechanics to the Cardiovascular System*, T. Yamaguchi, Ed. Tokyo: Springer-Verlag Publications, 2000, pp. 99-117.
71. Roger C. Barr, Maynard Ramsey III, and Madison S. Spach, "Relating Epicardial to Body Surface Potential Distributions by Means of Transfer Coefficients Based on Geometry Measurements," *IEEE Transactions on Biomedical Engineering*, vol.24, number 1, January 1977.

72. G. Fischer, B. Tilg, R. Modre, F. Hanser, B. Messnarz, and P. Wach, "On modeling the Wilson terminal in the boundary and finite element method," *IEEE Transactions on Biomedical Engineering*, vol. 49, issue 3, pp. 217-224, March 2002.
73. Nicolaas Westerhof, Frederik Bosman, Cornelis J. De Vries, and Abraham Noordergraaf, "Analog studies of the human systemic arterial tree," *Journal of Biomechanics*, vol. 2, pp. 121-143, 1969.
74. Bernard Widrow and Samuel D. Stearns, *Adaptive signal processing*. Delhi: Pearson Education, Inc., 1985.
75. Paulo S. R. Diniz, *Adaptive filtering – Algorithms and Practical Implementation*. Massachusetts: Kluwer Academic Publishers.
76. Kamran Jamshaid, Omar Akram, Farooq Sabir, Dr. Syed Ismail Shah, and Dr. Jamil Ahmed, "Application of adaptive and non adaptive filters in ECG signal processing," Report by GIK Institute of Engineering Sciences and Technology, http://www.khwarzimic.org/takveen/ecg_adaptive_f.pdf.
77. Jiapu Pan and Willis J. Tompkins, "A Real-Time QRS detection algorithm," *IEEE Transactions on Biomedical Engineering*, vol. 32, number 3, March 1985.
78. Adriaan van Oosterom and T. F. Oostendrop, "On computing pericardial potentials and current densities in inverse electrocardiography," *Journal of Electrocardiology*, vol. 25, pp. 102-106, 1992.
79. Richard N. Dimick, Laurence W. Hedlund, Robert J. Herfkens, Evan K. Fram, and Joe Utz, "Optimizing Electrocardiograph Electrode Placement for Cardiac-Gated Magnetic Resonance Imaging," *Investigative Radiology*, vol. 22, pp. 17-22, January 1987.

80. C. T. Gaffey and T. S. Tenforde, "Alterations in the rat electrocardiogram induced by stationary magnetic fields," *Bioelectromagnetics*, vol. 2, issue 4, pp. 357-370, 1981.